HADRONIC CHARM PRODUCTION
BY PROTONS AND PIONS ON IRON

by

Jack L. Ritchie

Submitted in Partial Fulfillment
of the
Requirements for the Degree

DOCTOR OF PHILOSOPHY

Supervised by Arie Bodek
Department of Physics and Astronomy
College of Arts and Sciences

University of Rochester
Rochester, New York

1983

CURRICULUM VITAE

Jack L. Ritchie, born August 14, 1955, graduated from Stinnett High School, Stinnett, Texas, in 1973. He attended Frank Phillips College in Borger, Texas, and graduated with the degree Bachelor in Physics with Honors from the University of Texas at Austin in 1977. Since then, he has been a graduate student at the University of Rochester in Rochester, New York, where he received the Master in Arts in Physics in 1979 and the Doctor of Philosophy in Physics in 1983.

ACKNOWLEDGEMENTS

I would like to express my thanks to all the members of the experiment described in this thesis. They were: Barry Barish, Arie Bodek, Richard Breedon, Rick Coleman, Greg Donaldson, Gene Fisk, Yasu Fukushima, Bill Marsh, Frank Merritt, Bob Messner, Steve Olsen, Petros Rapidis, Mike Shaevitz, Eric Siskind, Ian Stockdale, and Stan Wojcicki. Each made a significant contribution toward the success of this experiment.

Special thanks are due to my advisor, Arie Bodek. He has led by example with his high scientific standards, his unbelievable drive, his remarkable intellegence and his deep physics insight. I have been fortunate to have been Arie's student.

Some members of this experiment deserve special thanks. I would like to thank Rick Coleman, who worked hard on every phase of the experiment, for his patience and good nature in dealing with an occasionally irate and often overbearing graduate student. I would also like to express to Frank Merritt my appreciation for his herculean efforts on our analysis software.

I would like to thank the members of Group G at SLAC for their unusual hospitality during my visit there during an early phase of the analysis of this experiment.

I would like to express my gratitude to two members of the Fermilab staff, Anthony Malensek and Delmar Miller, for their help in making our experiment work. Their dedication stands out among their peers.

I would like to express my appreciation to my friends, too numerous to mention, among the graduate student community at Fermilab for their support during our shared tribulations.

I wish to acknowledge the helpful comments and criticisms of my friend Priscilla Auchincloss, who gave this thesis the most careful reading it will ever receive.

Above all, I wish to acknowledge the years of encouragement and unqualified support from my parents and family, to whom this thesis is dedicated.

ABSTRACT

An experiment to measure the production of prompt single muons by 350 GeV protons and 278 GeV pions on iron has been performed at Fermilab. The measurement was made using a heavily instrumented variable density target-calorimeter (beam dump) followed by a very large acceptance muon detector. These results have been used to study hadronic production of charmed particles.

In 350 GeV proton interactions, prompt single μ^+ and μ^- production are approximately equal. The charm production cross section is in the range of 20 to 40 μb/nucleon (most of the uncertainty being due to the uncertainty in the average semi-leptonic branching ratio B; in particular, $B(1 - B)\ \sigma_{charm} = 1.57 \pm .30$ μb/nucleon for $-1 < x_F < 1$). The data are well represented by $D\bar{D}$ production with $E\, d\sigma/dx_F \sim (1 - x_F)^{5.0 \pm .9}$. Charmed baryon production is allowed at the 10 μb/nucleon level. An upper limit on the charmed baryon cross section which is independent of the semi-leptonic branching ratio of charmed baryons has been calculated. Intrinsic charm appears to be ruled out by these data. Comparison to neutrino beam dump experiments, using the same model and branching ratio assumptions, favors an $A^{1.0}$ dependence for the charm cross section. Comparison to the NA16 experiment at CERN also indicates $A^{1.0}$ dependence.

In 278 GeV π^- interactions, prompt single μ^- production is larger than prompt single μ^+ production by almost a factor of two. The source of the μ^- excess has not been firmly established. One possible explanation, which enjoys some support from NA16 data, is the recombination of valence quarks from the beam pion with charmed quarks about 25% of the time. The x_F distribution of charmed particles produced via recombination appears to be considerably flatter than charmed particles produced without recombination. If this picture is correct, then the ratio of the semi-leptonic branching ratios of charged to neutral D's is greater than 1.8 (90% confidence level). The total charm cross section is in the range 15 to 30 μb/nucleon ($x_F > 0$), where most of the uncertainty comes from the uncertainty in the average semi-leptonic branching ratio ($B(1 - B)\ \sigma_{charm} = 1.29^{+.40}_{-.29}$ μb/nucleon for $x_F > 0$). Comparison with other pion experiments favors, as for protons, an $A^{1.0}$ dependence of the charm cross section.

TABLE OF CONTENTS

page

Chapter 1: INTRODUCTION 1
1.1 Charmed Particles 2
1.2 Experimental Methods in Hadronic Charm Production 6
1.2.1 Bump Hunting 6
1.2.2 Yields of Prompt Single Leptons 10
1.2.3 Searching for Short Tracks 17
1.3 Beam Dump Experiments 18
1.4 Fermilab Experiment 595 25

Chapter 2: APPARATUS 26
2.1 The Beam 27
2.2 The Detector 32
2.2.1 The Beamline PWC Spectrometer 32
2.2.2 The Target-Calorimeter 35
2.2.3 The Muon Identifier 42
2.2.4 The Toroid Spectrometer 45
2.3 Beam Logic and Triggering 49
2.3.1 The Interacting Beam Trigger 49
2.3.2 The Muon Triggers 53
2.4 Data Taking Procedures 58

Chapter 3: EVENT RECONSTRUCTION 61
3.1 PWC Tracking 62
3.2 Calorimetry 65
3.3 Muon Identification from Counters 69
3.4 Muon Tracking 72

Chapter 4: ANALYSIS OF THE PROTON HIGH-P DATA 80
4.1 Data Analysis 81
4.1.1 Event Selection 84
4.1.1.1 IBV Cuts 85
4.1.1.2 Muon Cuts 91
4.1.2 Event Classification 96
4.1.3 Rate Calculation 98
4.1.4 Density Extrapolations 104
4.2 Backgrounds 112
4.2.1 Accidentals 112
4.2.2 Misclassification of Events 116
4.2.3 Highly Asymmetric Dimuons 121
4.2.4 Upstream Interactions 125
4.2.5 Downstream Decays 127

4.2.6 Systematic Errors in the Density Extrapolation 130
4.2.6.1 Finite Plate Thickness 133
4.2.6.2 Finite Lifetimes of Pions and Kaons 133
4.2.6.3 Hyperon Semi-leptonic Decays 135
4.2.7 "Physics" Backgrounds 136
4.3 Prompt Single Muon Rates 138

Chapter 5: ANALYSIS OF THE PION HIGH-P DATA 147
5.1 Data Analysis 148
5.1.1 Event Selection and Classification 150
5.1.2 Rate Calculation 152
5.1.3 Density Extrapolations 163
5.2 Backgrounds 167
5.2.1 Accidentals 167
5.2.2 Interacting Muons 176
5.2.3 Semi-leptonic Pion and Kaon Decays in Flight 177
5.2.4 Highly Asymmetric Dimuons 178
5.2.5 Upstream Interactions 182
5.2.6 Downstream Decays 182
5.2.7 Systematic Errors in the Density Extrapolation 183
5.2.8 "Physics" Backgrounds 184
5.3 Prompt Single Muon Rates 186

Chapter 6: RESULTS ON CHARM PRODUCTION 195
6.1 Theoretical Considerations 195
6.2 Method of Analysis 201
6.3 Charm Production by Protons 208
6.3.1 Results from the Proton High-p Data 208
6.3.2 Other Proton Experiments 222
6.4 Charm Production by Pions 229
6.4.1 Results from the Pion High-p Data 229
6.4.2 Other Pion Experiments 244
6.5 Summary 247

REFERENCES 249

Appendix 1: DIMUON MONTE CARLO 255

Appendix 2: CALCULATION OF DOWNSTREAM DECAY RATES ... 273

Appendix 3: NONUNIFORM CALORIMETER DENSITY 276

Appendix 4: CALCULATION OF INTERACTING MUON RATES ... 279

Appendix 5: MUON INTERACTION CROSS SECTIONS 299

LIST OF TABLES

page

Table 1-1: Properties of charmed particles 5

Table 1-2: Sources of non-prompt leptons 14

Table 4-1: Number of proton triggers 83

Table 4-2: Proton flux after IBV cuts 90

Table 4-3: Probability of an extra single muon for the proton data 103

Table 4-4: Single muons rates for high and low intensity running 115

Table 4-5: Proton prompt single muon rates 144

Table 4-6: Proton non-prompt single muon rates 145

Table 4-7: Proton dimuon rates 146

Table 5-1: Number of pion triggers 149

Table 5-2: Pion flux after IBV cuts 151

Table 5-3: Probability of an extra single muon for the pion running 162

Table 5-4: Fraction of events rejected by accidentals cuts 174

Table 5-5: Negative single muon rates for high and low intensity running 175

Table 5-6: Pion prompt single muon rates 192

Table 5-7: Pion non-prompt single muon rates 193

Table 5-8: Pion dimuon rates 194

Table 6-1: Comparison of this experiment with the neutrino beam dump experiments 225

LIST OF FIGURES

page

Figure 2-1: Momentum distribution of the proton beam 30

Figure 2-2: Momentum distribution of the pion beam 31

Figure 2-3: Plan view of the apparatus 33

Figure 2-4: Layout of the PWC spectrometer 34

Figure 2-5: The target-calorimeter 36

Figure 2-6: Illustration of the density variation of the target-calorimeter 39

Figure 2-7: Calorimeter logic 41

Figure 2-8: Muon identifier counter and logic 44

Figure 2-9: Toroid counter and logic 48

Figure 2-10: The beam logic 52

Figure 2-11: Efficiency contours versus p and p_T 56

Figure 2-12: Muon trigger logic 57

Figure 3-1: Typical shower profile 68

Figure 3-2: Illustration of muon range fit 70

Figure 3-3: Comparison of range fit to spark chamber range 71

Figure 3-4: Calibration muon data 77

Figure 3-5: Dimuon mass for the proton data 78

Figure 3-6: Dimuon mass for the pion data 79

Figure 4-1: PWC χ^2 distribution 89

Figure 4-2: Proton D_{min} distribution 92

Figure 4-3: Muon rate versus beam momentum for p > 8 GeV/c 102

Figure 4-4: Density extrapolation for protons 106

Figure 4-5: Density extrapolations in bins 107

Figure 4-6: Raw prompt single muon rates versus p .. 111

Figure 4-7: Dimuon subtraction vesus p 123

Figure 4-8: Dimuon subtraction versus p_T 124

Figure 4-9: Additional backgrounds 132

Figure 4-10: Final rates versus p for μ^+ triggers ... 140

Figure 4-11: Final rates versus p for μ^- triggers ... 141

Figure 4-12: Final rates versus p_T for μ^+ triggers .. 142

Figure 4-13: Final rates versus p_T for μ^- triggers .. 143

Figure 5-1: Single muon triggers rates versus p 154

Figure 5-2: Shower length for μ^- triggers 158

Figure 5-3: Shower length for μ^+ triggers and IBV's 159

Figure 5-4: Illustration of the shower length fit .. 161

Figure 5-5: Density extrapolations for pion data ... 165

Figure 5-6: Raw prompt single muon rates versus p .. 166

Figure 5-7: Pion D_{min} distribution 170

Figure 5-8: Dimuon subtraction versus p 180

Figure 5-9: Dimuon subtraction versus p_T 181

Figure 5-10: Final rates versus p for μ^+ triggers ... 188

Figure 5-11: Final rates versus p for μ^- triggers ... 189

Figure 5-12: Final rates versus p_T for μ^+ triggers .. 190

Figure 5-13: Final rates versus p_T for μ^- triggers .. 191

Figure 6-1: Lowest order QCD diagrams for hadronic charm production 200

Figure 6-2: χ^2 versus α for proton μ^+ and μ^- separately 211

Figure 6-3: χ^2 versus α for simultaneous fit 212

Figure 6-4: Proton rates versus p with Monte Carlo . 213

Figure 6-5: χ^2 versus β for proton data 214

Figure 6-6: Proton rates versus p_T with Monte Carlo 215

Figure 6-7: Charmed baryon cross section limit versus semi-leptonic branching ratio ... 219

Figure 6-8: Ratio of $\bar{\nu}/\nu$ for the neutrino beam dump experiments 224

Figure 6-9: Ratio of μ^-/μ^+ versus momentum for protons and pions 230

Figure 6-10: χ^2 versus α for pion data 234

Figure 6-11: χ^2 versus β for pion data 235

Figure 6-12: Rates versus p_T with Monte Carlo 236

Figure 6-13: $(\mu^- - \mu^+)$ versus p 238

Figure 6-14: Rates versus p with Monte Carlo for two component fit 242

Figure A1-1: Proton dimuon mass 259

Figure A1-2: Sum of proton dimuon momenta 260

Figure A1-3: Proton dimuon pair p_T 261

Figure A1-4: Proton dimuon non-triggering momentum fraction 262

Figure A1-5: Momentum of triggering muon for proton dimuons 263

Figure A1-6: p_T of triggering muon for proton dimuons 264

Figure A1-7: Pion dimuon mass 265

Figure A1-8: Sum of pion dimuon momenta 266

Figure A1-9: Pion dimuon pair p_T 267

Figure A1-10: Pion dimuon non-triggering momentum fraction 268

Figure A1-11: Momentum of triggering muon for pion dimuons 269

Figure A1-12: p_T of triggering muon for pion dimuons 270

Figure A1-13: Ratio of unobserved to observed dimuons for proton data 271

Figure A1-14: Ratio of unobserved to observed dimuons for pion data 272

Figure A4-1: Muon interaction cross sections versus y 282

Figure A4-2: Shower length of "off-momentum" events 286

Figure A4-3: Sources of purely electromagnetic showers versus p 292

Figure A4-4: Interacting muon rates versus p for COMPACTED 294

Figure A4-5: Interacting muon rates versus p for EXPANDED 295

Figure A4-6: Ratio of inelastic hadron production to purely electromagnetic interactions ... 297

CHAPTER 1

INTRODUCTION

The experimental study of hadronic charm production has proved to be an attractive, yet difficult, undertaking. Inspite of the large number of experiments performed to date, no satisfying experimental consensus on charm cross sections or production distributions has emerged. This thesis describes an experiment which has investigated the hadronic production of charmed particles by observing muons from their semi-leptonic decays. While this method is somewhat indirect, it has proved to be one of the more successful employed so far.

This chapter will provide an introduction to the experimental side of charm physics. Section 1.1 very briefly reviews the history of charm and the properties of charmed particles. Section 1.2 describes the experimental approaches typically applied to the study of

hadronic charm production. Section 1.3 focuses on the technique employed here and compares experiments which observe the neutrinos from charm decays to this experiment. Section 1.4 briefly outlines the plan of this thesis.

1.1 Charmed Particles

The existence of charmed particles was proposed[1] in 1964, primarily in order to provide a symmetry between the leptons known at the time (e, ν_e, μ, ν_μ) and the hypothetical constituents of hadrons, known as quarks (u, d, s). The addition of a fourth quark, the charmed quark c, led not only to a more symmetrical scheme, but also to a model of the weak interaction, proposed[2] in 1970, which accounted for the weak interaction selection rules, including the absence of strangeness changing neutral currents (e.g., $K_L \rightarrow \mu^+\mu^-$). The first observation of charm came in 1974 with the discovery of the ψ simultaneously in a positron-electron (e^+e^-) annihilation experiment[3] and in an experiment measuring the production of e^+e^- pairs in proton-beryllium interactions.[4] (About the same time neutral currents, a prediction of the model[2], were observed in neutrino interactions[5], adding additional support to the charm hypothesis.) The ψ,

however, is not a charmed particle; its charm quantum number is zero. The ψ is a bound state of a charmed quark and a charmed antiquark. The first direct observation of particles with non-zero charm quantum number came in 1976 in an e^+e^- experiment[6] with the discovery of the D mesons.

It is noteworthy that prior to these <u>direct</u> observations of charmed particles several experiments[7] performed in hadron beams had observed charmed particles <u>indirectly.</u> They had observed unexpectedly high levels of prompt lepton production, often reported in terms of the prompt lepton to pion ratio. This ratio was found to be about 10^{-4} and could not be explained by the sources of prompt leptons which were known at that time, primarily vector meson decays. It is clear in retrospect that a significant fraction of these leptons were from the semi-leptonic decays of charmed particles (another important source was the low-mass dilepton continuum).

The properties of charmed particles, such as masses, lifetimes and branching ratios, have thus far been measured with notable success only in e^+e^- experiments[8] and neutrino experiments.[9] In both of these types of charm production experiment, the ratio of charm to non-charm production is relatively large (about .1) above the charm threshold. This favorable "signal-to-noise" ratio allows for the relatively background free study of

the properties of charmed particles. Recently data on charmed particle lifetimes also have become available from a photo-production experiment.[10] Table 1-1 lists the charmed particles observed to date and certain of their properties.

The study of charm in hadron interactions, however, is a more difficult undertaking. The charm to non-charm production ratio is small (about 10^{-3}), so that the "signal" is buried deep under a confusing background. If the goal were merely to measure the properties of charmed particles, then the effort might not be justified. (On the other hand, one might argue that the effort is justified by the large number of events, and resultant statistical power, which can be obtained, at least in principle, via the strong interaction.) But the hadronic production of charm is an important subject in itself. Any theory of the strong interaction, quantum chromodynamics for example, must accurately predict hadronic charm cross sections and production distributions. Therefore, the experimental difficulties must be surmounted. Accurate experiments must be performed.

Table 1.1: Properties of charmed particles. Shown are measured masses, lifetimes and semi-leptonic branching ratios of charmed particles. The values shown are from the Stable Particle Table of the Review of Particle Properties, Physics Letters, 111B, April, 1982. The $D^{*+}(2010)$ and $D^{*0}(2010)$, excited states of the D^+ and D^0, respectively, and the $\Sigma_c^{++}(2450)$, a charmed baryon, have also been observed. These particles decay strongly or electromagnetically into the lower lying charm states shown in the table. It should be commented that at this time the F meson mass remains a subject of controversy.

Particle	Mass (MeV)	Lifetime (10^{-13} s)	Semi-leptonic BR (%)
$D^{\pm}$	1869.4 ± 0.6	$9.1^{+2.2}_{-1.5}$	19^{+4}_{-3}
D^0	1864.7 ± 0.6	$4.8^{+2.4}_{-1.5}$	< 6
$F^{\pm}$	2021 ± 15	$2.2^{+2.8}_{-1.1}$	unknown
Λ_c^+	2282.2 ± 3.1	$1.1^{+0.9}_{-0.4}$	4.5 ± 1.7

1.2 Experimental Methods in Hadronic Charm Production

There are three basic techniques which have been employed thus far, or which are planned for the foreseeable future, in the experimental study of hadronic charm production. They are "bump hunting" (or spectroscopy), measuring prompt single lepton yields, and searching for short tracks (evidence of the decay of short-lived particles). Each will be discussed separately here, although in practice some experiments have combined aspects of more than one to arrive a hybrid technique.

In the following discussion, the emphasis will be placed on the experimental methods used in the study of hadronic charm production, and not on the results obtained so far. Since the topic of this thesis is an experiment on the hadronic production of charm, it is more appropriate to discuss the results of other experiments after these new results have been presented. Therefore, discussion of the results of other experiments will be deferred until the last chapter.

1.2.1 Bump Hunting

"Bump hunting" refers to looking for statistically

significant peaks in the reconstructed invariant mass distributions of specific (i.e., exclusive) final states. For example, it is known from e^+e^- experiments that the D^0 decays to $K^-\pi^+$ about 2% of the time. So in a hadronic charm search, one might histogram the invariant mass of all possible $K^-\pi^+$ pairings from each event. If a D^0 signal were present, it would appear as a "bump" at the appropriate mass, 1865 MeV. The detector for such an experiment would typically consist of a thin target followed by tracking devices, such as drift chambers, an air-gap magnet, and then more drift chambers. This arrangement would allow momentum measurement of the charged secondaries. Cerenkov counters would likely be present for charged particle identification, and some sort of electromagnetic shower calorimeter might also be present for the measurement of photons and the separation of electrons from pions.

The difficulty with this technique, indeed the reason the simple experiment described above would fail, is that in high energy hadronic interactions the multiplicities are large. In 200 GeV pion interactions on beryllium, the average charged multiplicity is eleven. These large multiplicities cause the number of possible combinations in a given event to be so large that the "correct" pairings do not stand out above the "combinatorial background" caused by all the spurious pairings.

Three "tricks" to get around this combinatorial problem have been tried:

(1) A lepton trigger. This idea relies on two facts: (1) charmed particles are produced in pairs and (2) they decay to final states containing an electron or muon with a roughly 8% branching ratio. The idea is to trigger on events with either a muon or electron from the semi-leptonic decay of one of the charmed particles, and to reconstruct the other one. One difficulty is that most leptons are not from charm decays. Most electrons are from pairs (e.g., Dalitz pairs), and while this is less a problem with muons, a copious source of muons, pion decay, does exist. Consequently, the enhancement in signal-to-noise derived from the lepton trigger, although it may be a factor of the order of 10 to 50, is not always adequate to allow for the observation of statistically significant charm signals. A second problem makes what results are obtained hard to interpret. In triggering on the lepton from the decay of one of the two charmed particles, the distribution of the other charmed particle becomes biased, and biased in an unknown way since the correlations between the two particles are not known. Therefore, the calculation of a cross section becomes model dependent because it depends on what is assumed for the production distribution of the unobserved charmed particle, as well as the form of the

assumed correlation. The most common assumption is that the two charmed particles are produced in an uncorrelated way. This assumption is theoretically dubious and is contradicted by at least one experiment.[11] The lepton trigger, it would seem, while potentially useful in detecting a previously unobserved particle, is not a powerful tool for the study of the dynamics of charm production.

It should be remarked that bump hunting is the only one of the three usual methods which can be employed to search for charmed particles in storage ring experiments, such as those conducted at the ISR, a proton-proton collider at CERN. As a result, a lepton trigger is common in the charm searches conducted there.

(2) Cut on the D^*-D mass difference. This allows a reduction in background in the search for D^*'s. The D^{*+} decays to $D^0\pi^+$ about 60% of the time. The D^0 may then decay to $K^-\pi^+$. The idea is to calculate the $K^-\pi^+\pi^+$ mass and the $K^-\pi^+$ mass for each combination in an event, and then histogram only those combinations for which the mass difference is consistent with the D^{*+}-D^0 mass difference, which is 145 MeV. (It should be noted that in princlple the same method can be employed with the Σ_c-Λ_c mass difference.) One experiment[12] has gone so far as to trigger on the pion from the D^* to $D^0\pi$ decay, but in order to do so, had to the restrict acceptance for D^*

production to a very small region around zero rapidity, thereby compromising the relevance of the measurement.

(3) Require a short track. The idea here is to select events in which the decay of a very short-lived particle is observed. In principle, this requirement can be made during the analysis, or can be put into the trigger, as is planned for a future experiment[13] at CERN. In either case, state-of-the-art silicon strip detectors are used as a "live" interaction targets, and provide a measurement of ionization (i.e., charged multiplicity) versus depth in the target. The virtue of this approach is that the selection criterion does not strongly bias the data, as in the case of the lepton trigger. Therefore, while it is technically ambitious at the present time, it may prove to be the ultimate solution to the problem of measuring exclusive final states in hadronic charm production.

1.2.2 Yields of Prompt Single Leptons

The measurement of the yields of leptons from the semi-leptonic decays of charmed particles is another way the hadronic production of charm has been studied. In particular, experiments have measured yields of prompt neutrinos and prompt <u>single</u> muons. There are numerous

sources of muon <u>pairs</u>, but <u>single</u> muons can originate only from weak decays (of course, in such a weak decay, a neutrino is also produced). Measuring these prompt single lepton yields depends on the fact that the lifetimes of charmed particles (see Table 1-1) are short with respect to the lifetimes of the conventional sources of single leptons, namely pions, kaons and hyperons. In fact, the word "prompt" as applied to leptons simply means "from very short-lived phenomena." (Note that muon pairs, which are produced only via the electromagnetic interaction, are therefore also prompt.) The disparity in the lifetimes of the sources of single leptons allows a separation of the prompt from non-prompt contributions to the total yield to be made by means of a technique known as the density extrapolation.

Experiments which measure prompt single lepton yields are frequently refered to as "beam dump" experiments. This is because it is standard in these experiments to place a large block of a dense material (typically iron, copper or tungsten) in a high-energy hadron beam, this block constituting the beam dump. When the hadrons interact in the dump, all varieties of secondary particles are produced. While most of the secondary particles are pions or other "conventional" particles, some exotic species, including charmed particles, are occasionally produced. The charmed particles immediately

decay, sometimes to final states in which leptons are present. The pions, kaons and hyperons, the other potential weak decay sources of single leptons (i.e., those which will result in a $\mu\nu$ or $e\nu$ pair, or in the terminology used here, a single lepton) will, with rare exception, re-interact hadronically. This is because the decay length of these particles is enormously greater than their interaction length in a solid material. Therefore, the number of non-prompt single leptons produced is heavily suppressed. Consequently, the prompt to non-prompt ratio can be large enough (usually .1 to 1.0) that the prompt contribution can be measured.

The way in which the prompt contribution is measured, as remarked earlier, is by the density extrapolation technique. This simply means that the single lepton yields are measured for different target densities, that is, different effective densities of the dump. (The change in <u>effective</u> density is accomplished by constructing the dump out of plates of dense material, and then by changing the distance between the plates.) The decay length, $c\tau\gamma\beta$, for any given particle produced in the dump (whether it is produced in the primary interaction, or in any subsequent interaction) does not depend on this effective density ρ_{eff}. But the "effective" interaction length λ_{eff} for this particle does depend on ρ_{eff}. In particular, $\lambda_{eff} = \lambda\rho/\rho_{eff}$, where

ρ is the actual density of the material (e.g., $\rho = 7.87$ g/cm^3 for iron) and λ is the interaction length of the particular particle under consideration in the material (i.e., when $\rho_{eff} = \rho$). The probability P_{decay} that the particle will decay, as opposed to interact, is given by

$$P_{decay} = (\lambda_{eff}/c\tau\gamma\beta)(1 + \lambda_{eff}/c\tau\gamma\beta)^{-1}.$$

The value of λ_{eff} is typically in the range of from 20 to 40 cm. Table 1-2 gives $c\tau\gamma\beta$ for the various sources of single leptons for relevant values of γ. For charmed particles, $\lambda_{eff}/c\tau\gamma\beta >> 1$, so that $P_{decay} \simeq 1$ independent of density. The approximation that $P_{decay} = 1$ is good to the 1% level. Therefore, the rate of prompt single lepton production from charmed particle decays (i.e., the number per incident hadron) does not depend on λ_{eff}, or more to the point, on the density ρ_{eff}. However, for the other sources of single leptons, $\lambda_{eff}/c\tau\gamma\beta << 1$. Therefore, ignoring high order terms in $(\lambda_{eff}/c\tau\gamma\beta)$,

$$P_{decay} = (\lambda_{eff}/c\tau\gamma\beta)(1 - \lambda_{eff}/c\tau\gamma\beta).$$

From this it follows that for sources for which $\lambda_{eff}/c\tau\gamma\beta$ is negligible compared to one, the rate of single lepton production will be proportional to λ_{eff}, and therefore inversely proportional to ρ_{eff}. The quantity $\lambda_{eff}/c\tau\gamma\beta$, as shown in Table 1-2, is negligible to a very good

Table 1-2: The sources of non-prompt single leptons, their lifetimes times the speed of light, the minimum energy they can have to decay to 20 GeV/c muons, and the ratio $\lambda_{eff}/c\tau\gamma\beta$ for that minimum energy. The value assumed for λ_{eff} was 27 cm, which is appropriate for the experiment described in this thesis. The value of $\lambda_{eff}/c\tau\gamma\beta$ is not small for all hyperons; however, these states have small production cross sections and small branching ratios to muons. The non-linearity in the density extrapolation due to hyperons will be discussed later.

Particle	$c\tau$ (cm)	E_{min} (GeV)	$\lambda_{eff}/c\tau\gamma\beta$
$\pi^{\pm}$	780	20	2.4×10^{-4}
$K^{\pm}$	371	20	1.8×10^{-3}
K_L	1554	22	4.0×10^{-4}
Λ°	7.9	74	.05
Σ^{+}	2.4	55	.24
Σ^{-}	4.4	54	.14
Ξ°	8.7	41	.10
Ξ^{-}	4.9	41	.18
Ω^{-}	2.5	29	.63

approximation for pions, kaons and hyperons. (The quality of this approximation will be discussed later.) Therefore, the total measured single muon rate $R_{1\mu}$ will obey the parameterization

$$R_{1\mu} = R_1 + R_2(\rho/\rho_{eff}),$$

where R_1 is the prompt rate and R_2 is the non-prompt rate. If $R_{1\mu}$ is measured for at least two different values of ρ_{eff}, the values of R_1 and R_2 can be determined.

The problem in these experiments is then to measure the rates for producing single leptons as a function of target density, and of course as a function of lepton momentum and transverse momentum. From these measurements, the momentum and transverse momentum distributions of the prompt single leptons can then be determined. Finally, it is possible to compare these distributions with various charm production hypotheses, or models, to determine which agree or disagree. This comparison, it should be noted, is somewhat indirect in that the charm production models predict the production distributions of the charmed particles themselves, while the experiments measure the distributions of one of the daughter particles from the decay of the charmed particles. Therefore, in practice, this comparison

requires a Monte Carlo program which performs the semi-leptonic decays of charmed particles in order to convert the predicted charm distribution into the measured lepton distribution.

Two additional complications to interpreting these measurements deserve to be mentioned. The first is that the semi-leptonic branching ratios of different charm particles are different, and in some cases not very well known. This, combined with the fact that the ratios of D^+ to D^0, or D to D^*, or D to F or Λ_c production are not known, leads to model dependence in the total charm cross section measured in these experiments. The second is that the charmed particles that are produced in the dump need not be produced in the primary interaction. Charmed particles can also be produced by secondary hadrons when they re-interact. This is probably only about a 15% effect, but does cause still further model dependence because an enery dependence for charm production must be assumed in order to calculate it.

Beam dump experiments have been useful in studying hadronic charm production, and in fact, the subject of this thesis is one such experiment. Therefore, considerable attention will be paid to the details of such a measurement later.

1.2.3 Searching for Short Tracks

The very short lifetimes of charmed particles (between 10^{-13} and 10^{-12} seconds) makes it possible to study their production by searching for decay vertices very close to the interaction vertex (within about a millimeter). Such a search can be conducted in a high-resolution optically sensitive detector, such as a nuclear emulsion or a bubble chamber with high-resolution optics operated in a mode in which the bubble size is small (50 microns diameter, for example). The earliest experiments of this type were no more than nuclear emulsions placed in hadron beams.

A more sophisticated and powerful approach is to place a multiparticle spectrometer downstream of the vertex detector. This has been the philosophy in the case of one experiment[11] at CERN. A small bubble chamber with high-resolution optics has been placed in front of a spectrometer capable of particle identification and momentum measurement. A more innovative approach has been undertaken by one group by trying to develop a very high-resolution high pressure streamer chamber.[14]

1.3 Beam Dump Experiments

There are two types of beam dump experiments, those which observe prompt neutrinos and those which observe prompt single muons. Neutrino beam dump experiments have been conducted at both CERN and Fermilab. However, the beam dump technique for studying prompt single muons has been used only at Fermilab.

Two such muon beam dump experiments have been run at Fermilab, Experiment 379 and Experiment 595. Experiment 595, the subject of this thesis, has used parts of the detector from the earlier experiment but represents a considerable upgrade over Experiment 379 in almost every respect. The results of Experiment 379 have been published[15] previously.

Several features are common to both neutrino and muon beam dump experiments. For example, as remarked earlier, the dump in both cases consists of a dense material in order to suppress the non-prompt single lepton rates and the effective density of these dumps can be varied in order to use the density extrapolation technique. In addition, since the two types of experiments observe different daughter particles from the <u>same</u> decays, the same physical processes are observed by both. But the differences are significant. The systematics of the two measurements are totally different. It is instructive to

examine the strengths and weaknesses of each technique.

The advantages of the muon beam dump are:

(1) Better control of systematics. It is relatively simple to observe muons because they are charged and highly penetrating particles. Neutrinos, however, must interact via the weak interaction and as a result have a very small cross section ($\sigma_{TOT}/E_\nu \simeq .6 \times 10^{-38}$ cm^2/GeV for neutrinos and about half that for antineutrinos). As a consequence of this small cross section it is necessary to have a high flux of neutrinos even with the largest and most massive detectors (one interaction per 10^8 neutrinos passing through the detector is typical). This dictates that the highest intensity proton beam possible be used, usually about 10^{13} protons per one millisecond spill. In contrast, in the muon beam dump case, beam intensities of the order of 10^5 per one second spill are adequate. This enormous difference in the beam requirements of the two different types of experiments allows three significant advantages of the muon technique to be identified:

(i) No beam scraping. There are losses from any beam. When protons are lost, they plow into beam pipes or magnets and produce pions, which in turn decay to muons and neutrinos. The muons present no problem, at least in principle, because they can be ranged out before they reach the detector, for

example in an earth berm, or they can be magnetically deflected. The neutrinos however cannot be stopped. Therefore, they represent a serious background, which is both difficult to monitor and independent of target density (so they will appear to be prompt).

(ii) Tracking of beam particles. Because of the low beam intensity it is possible to detect and measure the trajectory and momentum of each incoming particle. Selection criteria can be imposed to "clean up" the events and protect against sources of background such as interactions upstream of the dump.

(iii) Live beam dump. In the muon case, the beam dump can be instrumented. This allows the hadronic energy and shower shape to be measured event by event. Such measurements can be very important in eliminating background events, as will be shown later. Also, signals from the "live dump" can be put into the trigger.

(2) Better statistics. Even with the most intense proton beams available, neutrino beam dump experiments are still limited by the small neutrino cross section. It requires a lot of beam time to obtain a few events. One CERN experiment[16] reported a rate of 4.6 events per 10^{18} protons per ton of detector for 400 GeV protons incident on a full density copper dump. That means with a 500 ton detector and 10^{13} protons per spill one event

was collected every 43 spills. If there were 6 spills per minute, that was one event in 7 minutes, or 8 events per hour. In the muon beam dump experiment described in this thesis, about 25 events were collected each spill. During the course of an entire experiment, a neutrino beam dump experiment may collect a few thousand events. The muon experiment collected a few million. Therefore, greater statistical power is available to the muon type experiment.

It should be noted, however, that the situation is not nearly as bad as the raw number of events collected might suggest. The fraction of events which are prompt tends to be higher for neutrino experiments. This is because most of the muons which a muon experiment triggers on are from pion decays. When pions decay, the muons take 80% of the parent momenta on average, and the neutrinos only 20%. Therefore, most of the neutrinos from these pion decays are low momentum, frequently below the trigger thresholds of the neutrino experiments (which trigger on energy deposited by a neutrino interaction in the detector). In fact, most of the muon-type neutrinos on which a neutrino beam dump experiment triggers are from kaon decays. The effect of this larger prompt to non-prompt ratio is that fewer events are needed by a neutrino experiment to obtain the same precision in determining the prompt rate. In fact, the relative

uncertainty in the prompt rate is roughly proportional, for the same number of events, to the ratio of non-prompt to prompt production. Since the prompt to non-prompt ratio is typically 1:1 for muon-type neutrino experiments, and about 1:8 for the proton data sample for the muon experiment described here (after background subtractions), it follows that it is necessary to have about a factor of 64 more events in the muons case to have equal errors (a careful calculation reveals that the factor is actually closer to 40). Note, however, that 25 events per spill is greater than one event in 43 spills by a factor of 1075, so that spill-for-spill, the muon experiment wins out by a large factor.

Two additional comments are relevant: (1) The neutrino experiments are statistically limited by the fundamental fact that the neutrino cross section is small, while the limitation of $\sim$25 events per spill for the muon experiment was a detector limitation and could be improved upon substantially in princlple (the limiting "dead-time" was due to spark chambers; drift chambers, for example, are much faster). (2) Because of the additional statistical power of the muon experiment, more systematic checks, such as taking data at three densities (rather than the two which are standard for neutrino experiments) can be made.

(3) Larger acceptance for charm. In the muon beam

dump case, the muon detector can be placed immediately downstream of the dump. In the neutrino case, enough space must be left between the dump and the neutrino detector to allow the muons produced in the dump to be either ranged out or magnetically swept away. This allows a larger angular, and therefore transverse momentum, acceptance in the muon beam dump case.

(4) Different hadron beams. This is perhaps the most significant advantage of the muon beam dump technique. Charm production can be studied with different incident hadrons. Neutrino beam dump experiments can only be run with protons because both pions and kaons, if present in the beam, would decay in sufficient numbers to neutrinos that the experiment would be totally swamped.

The muon beam dump experiment described in this thesis took data with both protons and negative pions.

The advantages of the neutrino beam dump experiments are:

(1) Ability to detect electron neutrino events. The prompt single electrons produced in the semi-leptonic decays of charmed particles do not escape the dump and are unobservable. However, the associated neutrinos can be detected in a neutrino detector. This allows these experiments to test e-μ universality. Also, since the

only sources of non-prompt electron-type neutrinos are rare pion, kaon and hyperon decays (the largest is $K \rightarrow \pi^0 e\nu$, which has a branching ratio of 4.8%), the prompt to non-prompt ratio is substantially higher than for muon-type neutrinos. In fact, it may be on the order of 10 to 1, depending on the details of the experiment. However, other backgrounds become problematic, such as cosmic rays, neutral current ν_μ interactions and charged current ν_μ interactions at high y. Of course, a detector with good electron identification, such as a bubble chamber, can cope with these backgrounds rather easily. (Bubble chambers, it should be noted, have substantially smaller fiducial masses than counter neutrino detectors, typically about a factor of 30 less, so that statistics become poor.)

(2) No dimuon background. By far the largest background with which a muon beam dump experiment must cope is the mis-identification of dimuon events, which are prompt, as single muon events. This can occur when one of the two muons has low momentum. It may not, for example, even escape the dump, in which case it cannot be observed. The neutrino experiments face no such problem.

1.4 Fermilab Experiment 595

Fermilab Experiment 595 is the subject of this thesis. The experiment, as remarked earlier, was a measurement of prompt single muon production in hadronic interactions. Data were taken with both 350 GeV protons and 278 GeV negative pions incident on an iron target. Chapter 2 will describe the detector and the triggers used, as well as certain important data taking procedures. Chapter 3 will describe the event reconstruction and data handling. Chapter 4 will describe the analysis of the proton data taken with a trigger requiring the muon momentum to exceed 20 GeV/c. Chapter 5 will describe the analysis of the pion data taken with the same trigger. Chapter 6 will address the question of what can be learned about hadronic charm production from these measurements.

CHAPTER 2

APPARATUS

The apparatus in Experiment 595 consisted of a beam incident on a target followed by a detector. The momentum and trajectory of the incident beam particles were measured by a proportional wire chamber (PWC) spectrometer upstream of the target. The target, a "beam dump," was actually a fully instrumented hadronic calorimeter, and the detector was 700 tons of steel with scintillation counters and spark chambers scattered throughout. Each of these components will be described in this chapter. Also, the triggers will be described, along with certain important procedures which were followed while taking data.

2.1 The Beam

The detector was housed in Laboratory E in the Neutrino Area at Fermilab. The hadron beamline into Lab E was referred to as the N5, and was originally built as a hadron beam to the 15′ Bubble Chamber (which was located downstream of Lab E). Since bubble chamber experiments require few particles per pulse a very small acceptance (about .3 microsteradians in solid angle and ±.5% in momentum) was adequate.

Among the goals of Experiment 595 was to compare charm production with protons and pions, and for such a comparison to be meaningful, it was necessary that the pion beam energy be as close to that of the proton beam as possible. Obtaining adequate pion flux at high energy required that the N5 be modified to increase the acceptance. This was accomplished by changing the "front-end" of the beamline as described in detail in Reference 17. The acceptance of the upgraded N5 was calculated to be 2.7 microsteradians in solid angle (with the momentum bite unchanged). The actual acceptance was smaller due to misalignments of the beamline elements. But the upgrade did yield a <u>measured</u> increase in pion flux of a factor of 9 over the original beamline. Ultimately, 278 GeV/c was chosen as the energy of the pion beam because it was roughly the highest energy at

which adequate flux could be obtained.

The proton data were taken with a 350 GeV diffracted proton beam. The beam as it entered Lab E measured 2.6 cm horizontally and .6 cm vertically. Figure 2-1 shows the momentum profile of the proton beam. The width is consistent with that expected from the resolution of the PWC spectrometer, suggesting that the momentum spread of the beam was narrow, as expected for diffracted protons. The distribution is slightly asymmetric with a small excess on the low momentum side, probably due to a "quasi-elastic" component in the momentum distribution (i.e., due to protons scattering elastically from nucleons in the target rather than from target nuclei).

The pion data were taken with a 278 GeV negative beam produced from 350 GeV protons incident on a target of one interaction length of alumimum. The beam as it entered Lab E measured 4.4 cm horizontally and 1.0 cm vertically. The momentum profile is shown in Figure 2-2. The width is larger than expected from spectrometer resolution alone. The momentum spread of the beam can be determined if it is assumed that the momentum spread and resolution add in quadrature to produce the observed width. This calculation yields a momentum spread of ±.48%, in good agreement with the expected momentum acceptance of the beamline.

Since the beamline transported all negatively charged

particles produced within its acceptance, the particles reaching Lab E included negative kaons and antiprotons as well as negative pions. This "contamination," however, was of a rather insignificant magnitude. The particle production results of other experiments[18] indicate that the kaon fraction of the beam at the downstream end of the production target in this experiment (i.e., for 278 GeV/c secondaries from 350 GeV primaries) was (.6 ± .3)% and that the antiproton fraction was negligible (less than .01%). Of course, both pions and kaons sometimes decayed in flight between the production target and Lab E (a distance of 880 meters) giving rise to a muon component of about 1%. Also, since kaons are more massive and shorter lived than pions, the K/π ratio at Lab E was less than at the production target by a factor of .72. Therefore, the <u>hadrons</u> in the beam were overwhelmingly pions (99.6±.2%).

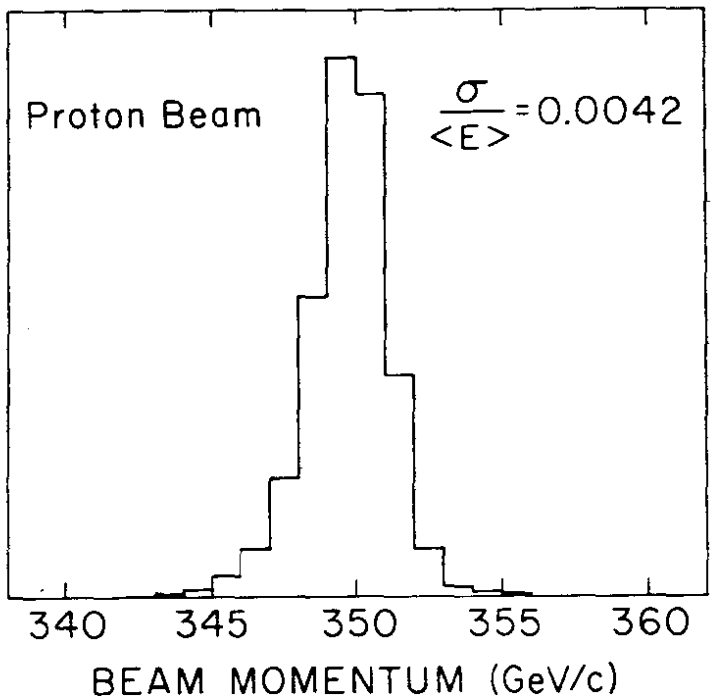

Figure 2-1: Momentum distribution of the proton beam measured with the beamline PWC spectrometer.

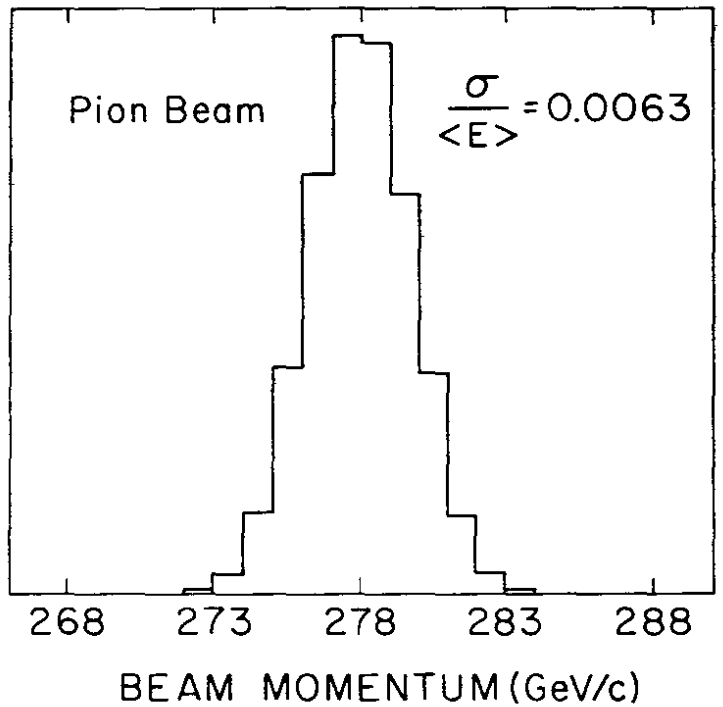

Figure 2-2: Momentum distribution of the pion beam measured with the beamline PWC spectrometer.

2.2 The Detector

The detector consisted of, from upstream to downstream, a beamline PWC spectrometer system, a target-calorimeter, a large acceptance muon identifier and an iron toroid spectrometer. The layout is shown in Figure 2-3. Each of these systems will be described separately.

2.2.1 The Beamline PWC Spectrometer

The beamline spectrometer consisted of 16 proportional wire chambers and two Main Ring dipole bending magnets. For reasons which were mainly historical, three different designs of PWC's were used, each with a different readout system. Eight of the chambers had 24 wires with 1 mm spacing, four had 64 wires with 1 mm spacing, and four had 64 wires with 2 mm spacing. The arrangement of chambers, nine of which measured position in the horizontal plane and seven of which measured position in the vertical plane, is shown in Figure 2-4. The three different PWC types can be distinguished by their size in the figure.

The PWC's were located both upstream and downstream of two Main Ring dipole bending magnets which deflected

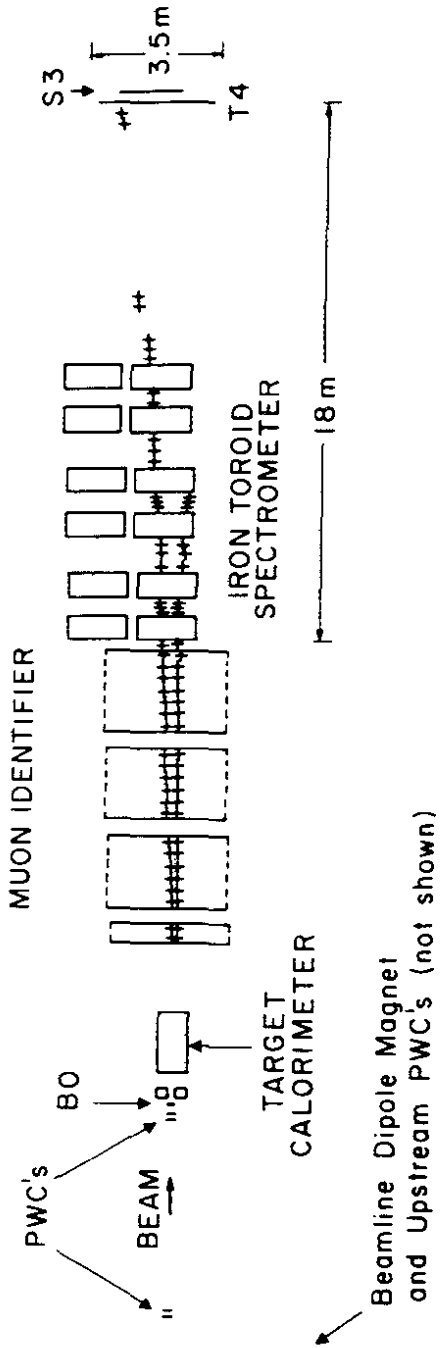

Figure 2-3: Plan view of the apparatus.

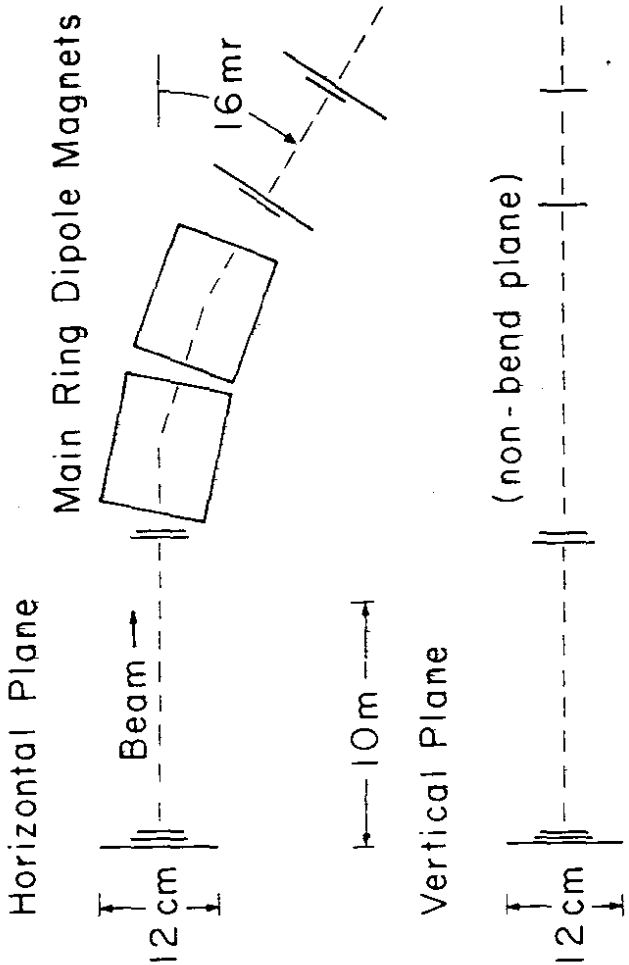

Figure 2-4: Layout of the beamline PWC spectrometer.

the beam by 16 mr in the horizontal plane. This system provided a momentum resolution of ±.42%, as inferred from the measured width in momentum of the 350 GeV diffracted proton beam. The large number of chambers provided considerable redundancy so that the performance of the system did not depend on any single chamber. Indeed, the three independent readout systems provided protection against the failure of any single system (fortunately, no such failure occurred during the 13 week data taking period). The efficiencies of the PWC's were typically greater than 95%. One chamber developed an internal breakdown late in the run.

Signals from the PWC's were latched and written to tape for each triggering event. Signals from the PWC's were not used in triggering.

2.2.2 The Target-Calorimeter

The target-calorimeter, shown in Figure 2-5, served three basic functions in this experiment: (1) beam definition, (2) variable density interaction target (i.e., beam dump), and (3) hadronic calorimetry. These three functions will be addressed separately:

(1) Beam Definition. Four scintillation counters which were mounted near the upstream end of the

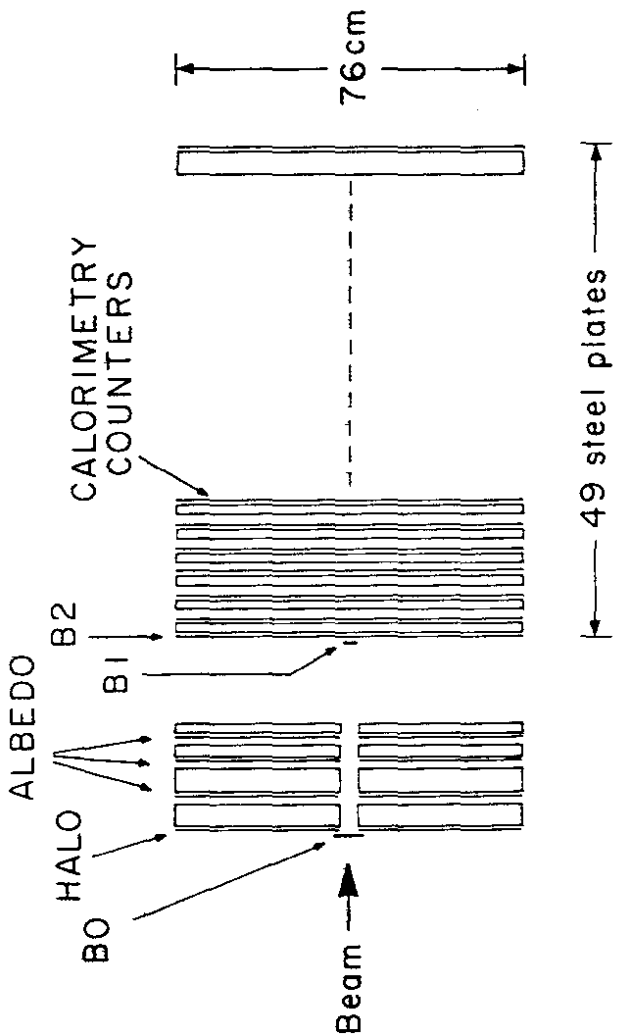

Figure 2-5: The layout of the target-calorimeter. The beam-defining and calorimetry counters are shown.

target-calorimeter were the primary beam defining counters in this experiment. They were referred to as B0, B1, B2 and HALO, and their positions are shown in Figure 2-5. All four were centered on the beam. B0 served as the timing reference for the entire experiment. It was 7.6 cm x 7.6 cm. B1, the smallest of the four counters, was 5.1 cm x 5.1 cm. B2 was a large counter, 76.2 cm x 76.2 cm, the same size as the steel plates. HALO was also 76.2 cm x 76.2 cm, but it had a 7.0 cm x 7.0 cm hole in the center through which the beam passed. HALO was used as a veto since a hit in HALO indicated a particle outside the beam. All four counters were viewed by Amperex 56AVP photomultiplier tubes. The way signals from these counters were used in defining the beam particles will be described in detail in a later section on beam logic and triggering (Section 2.3.1).

(2) Variable Density Beam Dump. The target-calorimeter consisted of 49 steel plates, each measuring 76.2 cm x 76.2 cm. The first 20 plates were 3.8 cm thick, the next 25 plates were 5.1 cm thick, and the final 4 plates were 10.2 cm thick, providing a total of 2.4 meters of steel. All 49 plates were mounted on rails that allowed them to be moved along the beam direction. By varying the spacing of the plates the effective density of the target-calorimeter could be changed. The most compact configuration, that is, the

most dense, had a density equal to $.75\rho_{Fe}$. The reason it was less dense than iron was that scintillation counters were mounted between the plates. Data were taken in three configurations, referred to as COMPACTED, SEMI-EXPANDED, and EXPANDED, the effective densities of which were in the ratio 1:2/3:1/2, respectively. These three configurations are illustrated in Figure 2-6. (In fact, data were also taken in two additional configurations which will be referred to as SPECIAL 1 and SPECIAL 2, which had the same effective density as COMPACTED. These configurations will be described in Section 4.1.4.) In changing the density the gaps between only the first 38 plates were varied, corresponding to 1.7 meters of steel. The remaining plates were kept at the same density, fully compacted, in each of these three configurations. When the density was changed, the position of the fifth plate was kept fixed, as illustrated in Figure 2-6. This had the effect of holding the mean interaction point fixed, so that the acceptance of the downstream muon detector did not depend on density.

(3) Hadronic Calorimeter. A 76.2 cm x 76.2 cm x .6 cm plastic scintillation counter was mounted on the downstream face of each steel plate. The first 40 counters were viewed by RCA 6342A photomultiplier tubes. The last 9 counters were viewed by Amperex 56AVP

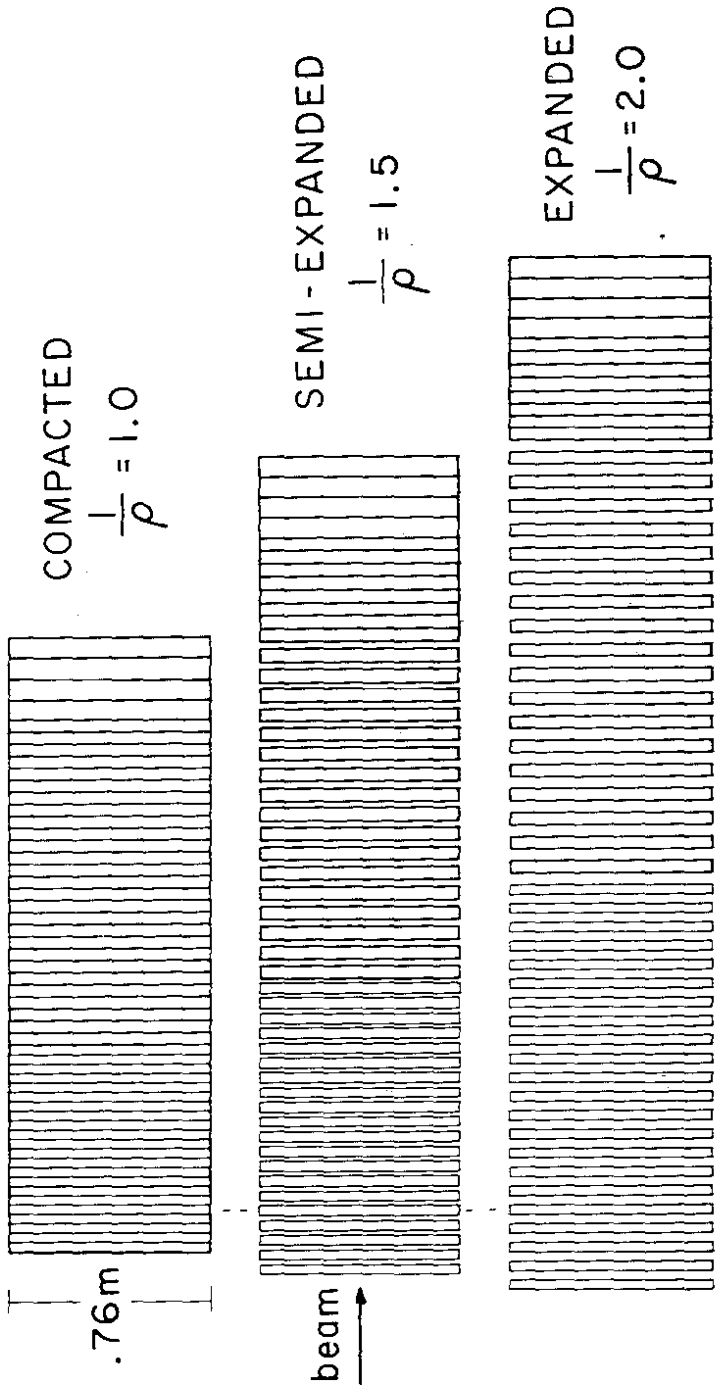

Figure 2-6: Illustration of the three configurations of the target-calorimeter.

photomultiplier tubes. The photomultiplier output from each of the first 40 counters was split into two equal signals and one of the signals was amplified by a factor of 40. These amplified "HI's" went directly to ADC's ("analog to digital converters," which integrated the phototube signals and stored the values), and were used to determine the response of these counters to muons. The unamplified signals were again split via resistive divider into a "LOW" (75%) and a "SUPERLOW" (25%). The SUPERLOW signals were used only when the LOW's saturated. The calorimeter logic is shown in Figure 2-7. The calorimetry, including the flasher system and special hardware for high rate corrections, has been described in detail in Reference 19. The hadronic energy resolution measured in this experiment was gaussian with σ/E equal to $.69/\sqrt{E}$ for protons and $.66/\sqrt{E}$ for pions.

In addition to providing energy and shower shape information off-line, two signals generated by the calorimeter were used in triggering. One, referred to as ESUM, was a hardware sum of the first 40 counters. The other, referred to as E4-11, was also a hardware energy, but was calculated only from the fourth through eleventh calorimetry counters (eight counters in all). The use of ESUM and E4-11 in the beam logic and triggering will be described in Section 2.3.1.

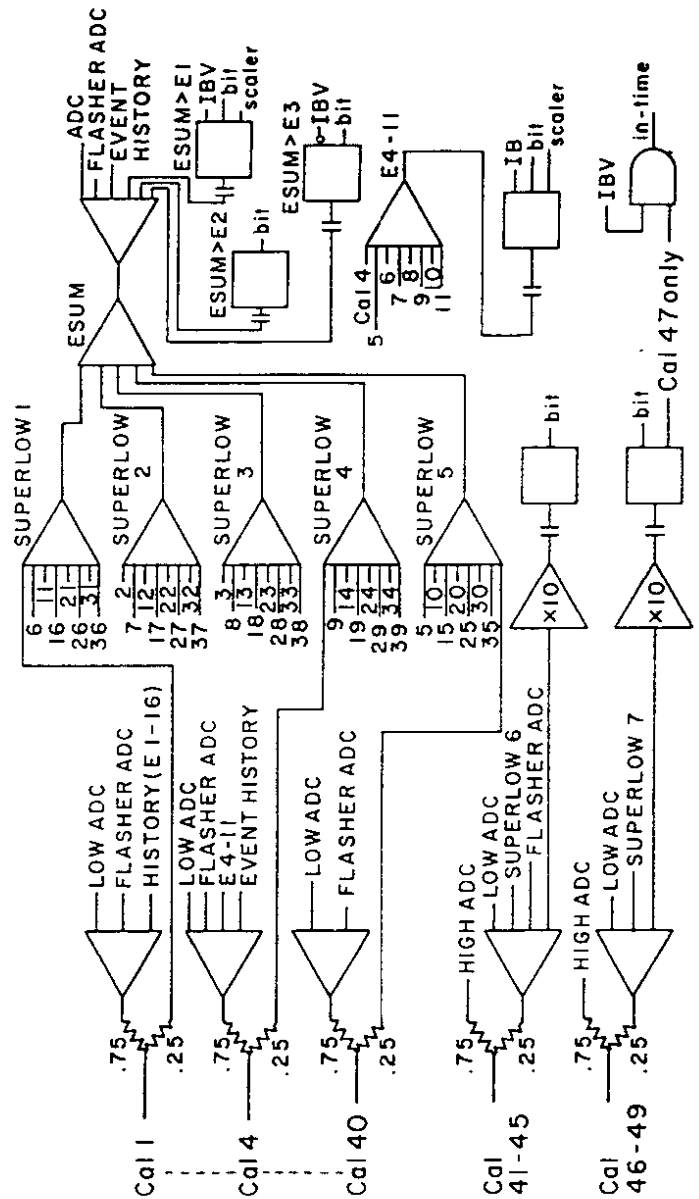

Figure 2-7: Calorimeter logic.

2.2.3 The Muon Identifier

The muon identifier consisted of 3 m x 3 m scintillation counters and spark chambers sandwiched between 3 m x 3 m x 5.1 cm steel plates. This device provided identification and tracking of muons with very large (200 mr) angular acceptance.

As can be seen from Figure 2-3, there were four separate units comprising the muon identifier. The first unit consisted of four steel plates with two spark chambers and two counter hodoscopes (one with 28 cm horizontal segmentation and the other with 28 cm vertical segmentation) intersperced, all followed by an array of large proportional wire chambers. These chambers were 3 meters in length with 2.54 cm wire spacing. There was a single horizontal measuring plane and a single vertical measuring plane, each plane consisting of four separate chambers with 32 wires each.

The remaining three units were identical "carts" which were built as part of the neutrino target for Fermilab Experiment 356. Each cart consisted of 28 steel plates (1.4 meters in all), with six 3 m x 3 m magnetostrictive readout spark chambers sandwiched between every 4 plates (20.3 cm of steel) and fourteen 3 m x 3 m liquid scintillation counters with wave-shifter light pipes sandwiched between every 2 plates (10.2 cm of

steel). The spark chambers provided a position resolution of about ±.5 mm for muons passing through them. These carts have been described in greater detail in Reference 20.

The large liquid scintillation counters served two functions: triggering, and the separation of dimuon events from single muon events. Each counter was viewed by four RCA 6342A photomultiplier tubes. Figure 2-8 shows the design of these counters and the associated logic that was relevant to this experiment. An "S" signal was formed for each counter by discriminating the amplified (x100) sum of the four phototubes. The discriminator thresholds were set at values at which each S would be efficient (greater than 90%) for a single muon passing through the counter. The S signals were used in triggering.

Pulse height information from each counter was used, along with tracking information from the spark chambers, to separate dimuon events from single muon events. This separation will be described in later chapters.

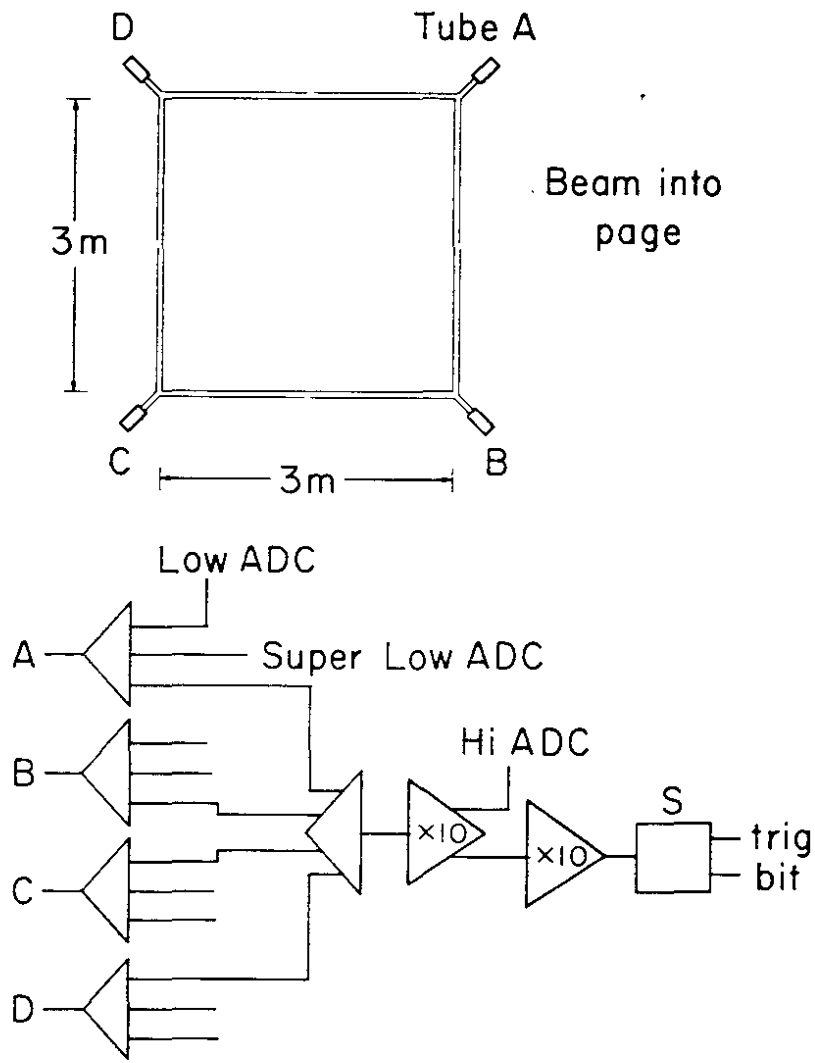

Figure 2-8: Shown are a liquid scintillation counter from the muon identifier and the associated logic relevant to this experiment.

2.2.4 The Toroid Spectrometer

The toroid spectrometer consisted of a toroidal magnet with spark chambers and scintillation counters positioned periodically throughout its length. The magnet itself consisted of 24 iron disks, each 1.73 m in radius with a 25 cm diameter hole in the center and 20.3 cm thick. Eight of these disks were mounted on each of three movable carts. An azimuthal magnetic field of about 17 kilogauss was created in each disk by passing current through copper coils, which were wound through the central holes and around the eight disks of each toroid cart. A .95 cm air gap divided each disk into an upper and a lower half. The magnetic field was measured in these gaps for each disk, as a function of radius. A detailed field map was generated and used in the calculation of muon momentum. During the entire run of this experiment the polarity of the toroid magnet was in the direction to focus negative muons. Also, the toroid spectrometer was "off-axis," that is, it was displaced from beam center by one half radius, as shown in Figure 2-3. This avoided the loss in acceptance for high momentum muons which would have resulted if the central hole had been centered on the beam.

Three planes of magnetostrictive readout spark chambers were located after every four toroid disks (a

few of these spark chambers were the same as in the muon identifier, but most were 152 cm x 305 cm and were of older construction). Five additional planes of spark chambers were located behind the toroid where there was no magnetic field. The position resolution of these spark chambers was about ±.5 mm. A 3 m x 3 m acrylic scintillation counter was mounted on the downstream side of each disk. Each counter actually consisted of four pieces of scintillator, as shown in Figure 2-9. Each counter had wave-shifter light pipes and was viewed by ten RCA 6342A photomultiplier tubes. The logic associated with these counters is also shown in Figure 2-9. An S signal, efficient for a single muon, was generated for each counter, but only if the muon passed through the right half of the counter (the side the beam was centered on). These toroid S's were used in triggering on high momentum muons.

In a building separate from Lab E and farther downstream, two additional planes of spark chambers and two scintillation counters, T4 and S3, were located. These chambers improved the determination of the angles of muons exiting the toroid. The counters were also used in triggering.

The momentum resolution achieved was 11% and was dominated (in the relevant momentum range, below 150 GeV/c) by multiple scattering. Muon calibration data

were taken at incident muon momenta of -278, -225, -100, -50, -25, +50, +100 and +200 GeV/c. A momentum dependent correction factor, which was everywhere less than 2% for muon momenta less than 150 GeV/c, was determined from this calibration data. After this small correction is applied, the absolute momentum calibration is believed to be good to about 1%.

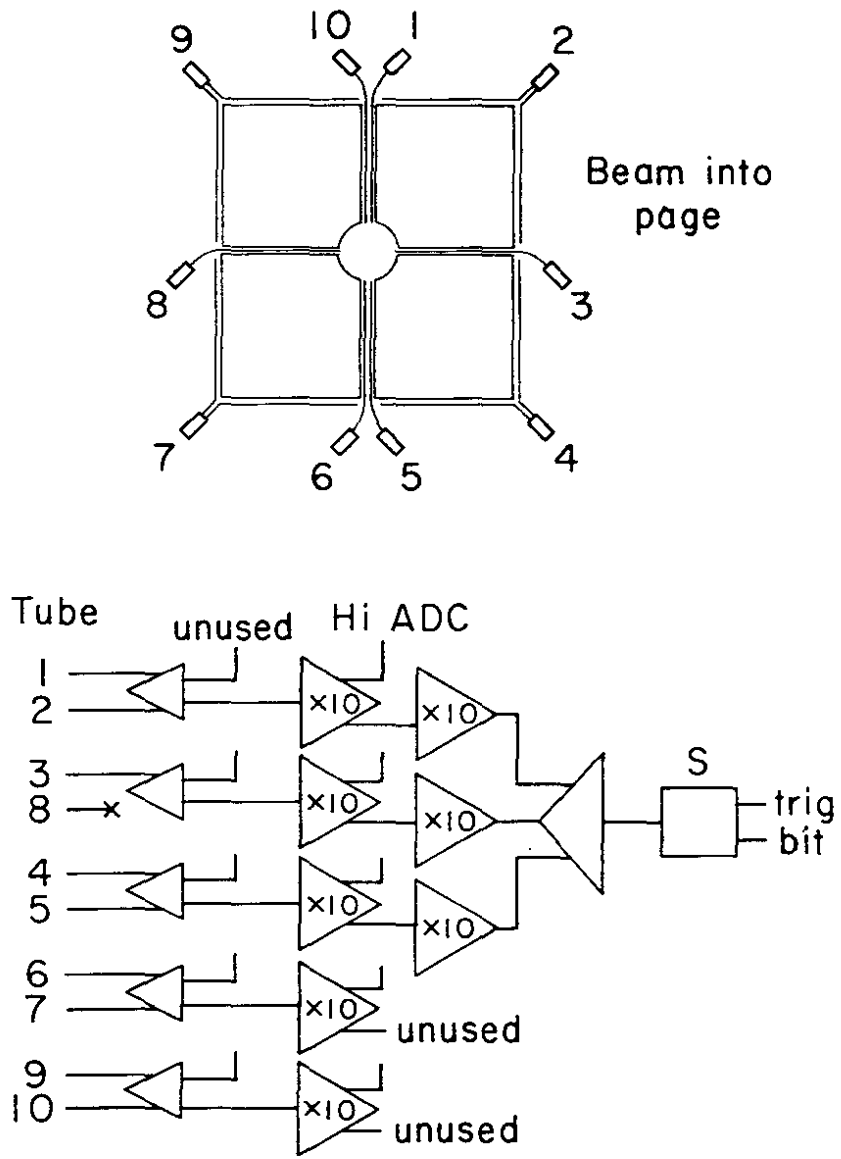

Figure 2-9: Shown are an acrylic scintillation counter from the toroid spectometer and the associated logic relevant to this experiment.

2.3 Beam Logic and Triggering

The decision to trigger in this experiment, that is, to record an event on magnetic tape for later analysis, was made on two levels. The first depended only upon the incoming beam particles as observed by scintillation counters in the target-calorimeter and was made by the "beam logic." The second depended upon the coincidence of an acceptable beam particle and the passage of a muon through the appropriate counters in the muon identifier or toroid spectrometer. It is therefore appropriate to discuss the beam logic, which provided an "interacting beam trigger," and the muon logic, which determined the passage of a muon, separately.

2.3.1 The Interacting Beam Trigger

The beam logic is shown in Figure 2-10. The main features are that a coincidence of hits in B0, B1 and B2 created a signal referred to as BEAM. A signal called CLBM (clean beam) was generated if BEAM occured along with (1) no hit in HALO and (2) pulse height of less than twice minimum ionizing in B0. A coincidence between CLBM and greater than a given amount of energy (about 10 GeV for the proton data and about 5 GeV for the pion data) in

E4-11 created a signal called IB (interacting beam). The E4-11 requirement eliminated those hadrons which did not interact near the front of the target-calorimeter. This insured both that the hadronic showers would be contained in the calorimeter and that all muons produced in the calorimeter would have to penetrate approximately the same amount of steel to reach the muon identifier.

The interacting beam trigger, IBV as it was called (interacting beam with vetos), required an IB to occur in coincidence with a total energy in the target-calorimeter of greater than 30 GeV (ESUM>E1), but in the absence of several possible veto conditions. The ESUM requirement eliminated muons which had deposited enough energy in the front of the calorimeter to satisfy the E4-11 requirement. An IBV was vetoed if any of the following conditions occurred:

(i) ESUM greater than 500 GeV (ESUM>E3). This eliminated triggers with two hadrons in the same rf bucket.

(ii) An additional beam particle (i.e., a hit in B0 or HALO) within 88 nanoseconds before or 76 nanoseconds after the triggering particle.

(iii) A hit in either of two scintillation counter vetos. One of these was a 1.5 m x 1.5 m counter that had a hole in it through which the beam passed. This counter was located 60 meters upstream of the

target-calorimeter. It vetoed halo muons associated with, but outside, the beam. (This was in place only during the pion running.) The other veto signal came from 3 m x 3 m counters (in an unused "neutrino cart") located just to the side of the target-calorimeter.

As noted earlier, IBV was a precondition for a muon trigger. It was scaled and used to normalize the number of muon triggers to the number of interacting hadrons. That is, rates quoted in this thesis are in units of events per IBV. In addition, IBV was used as a trigger, in that a random sample of IBV's was written to tape.

An additional logic signal that proved to be useful in the analysis was a coincidence between IBV and calorimeter counter 47, where both input signals were set to be 5 nanoseconds wide. The result was a "bit" which was set true only if IBV and the hit in counter 47 were simultaneous to within 5 nanoseconds, much less than the 19 nanoseconds between rf buckets. This signal was referred to as the "in-time" bit. Its use will be described in Section 4.1.1.2.

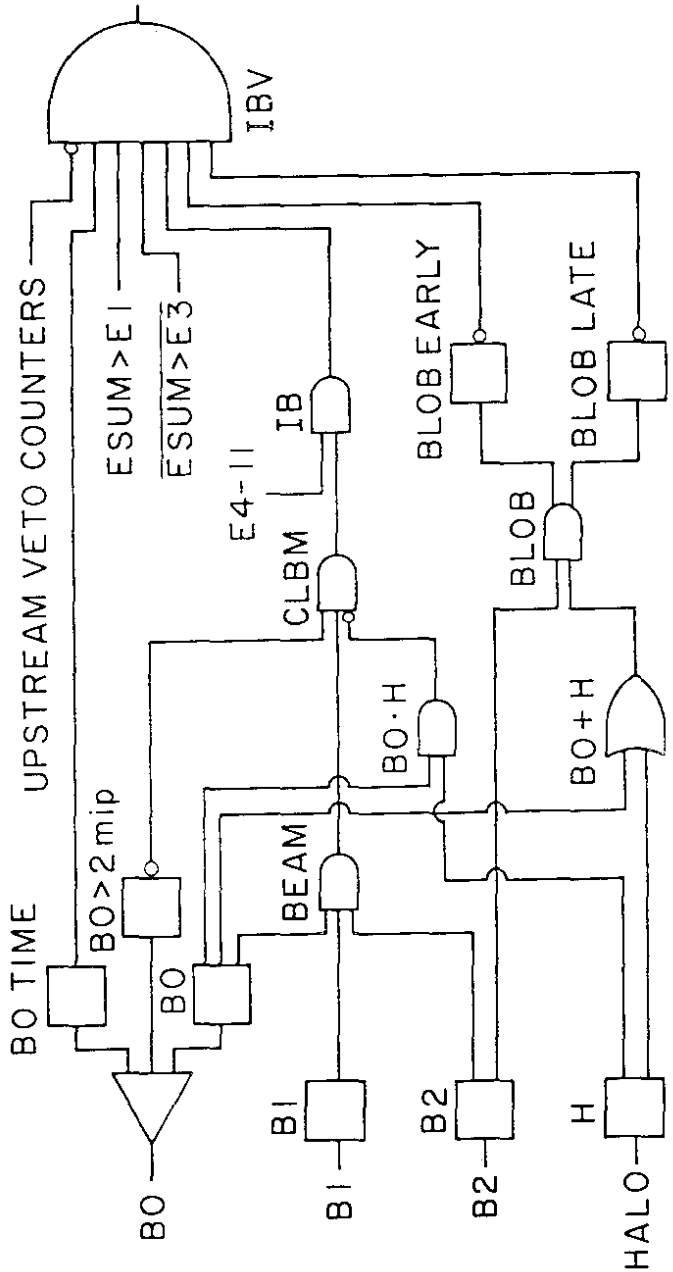

Figure 2-10: The beam logic.

2.3.2 The Muon Triggers

Data were taken with two different muon triggers. Both required an IBV in coincidence with a muon in the downstream part of the detector. One trigger, referred to as the "range" trigger, used only counters in the muon identifier and required the muons to penetrate a minimum amount of steel, corresponding to a minimum momentum of 8 GeV/c. By triggering on such low momentum muons, a very large acceptance for charm production, almost the entire forward hemisphere, was obtained, although at the cost of a small (about 5%) signal to noise ratio. Also, about 30% of the muons which passed the range trigger requirement did not penetrate into the toroid spectrometer and therefore could not be analyzed for sign. Nonetheless, these low momentum data do provide the least model dependent way possible of measuring the charm cross section using the beam dump technique. Results from the low momentum data will not be presented in this thesis.

The second trigger, the "high-p" trigger, was designed to study of the forward region of the charm production spectrum. It used the toroid acrylic counters to require muons to penetrate the entire length of the toroid spectrometer. This corresponded to a minimum momentum of about 20 GeV/c. Also, the acceptance for

positively charged muons was slightly different than for negatively charged muons because of the geometry of the toroid spectrometer. Figure 2-11 shows the high-p trigger acceptance versus p and p_T, for both signs of muons.

The logic diagram of the high-p trigger is shown in Figure 2-12. Signals from the toroid acrylic counters, which were numbered 1 through 24 consecutively from upstream to downstream, were grouped into six sets of four consecutive counters (e.g., 1 through 4, 5 through 8, etc.). A signal called a "Z" was formed when a coincidence occurred between two of the four S signals from the counters within one of these sets. The Z's were numbered 1 through 6 from upstream to downstream. The high-p trigger required a coincidence of IBV with Z2, Z4 and Z6.

Special triggers were set up to monitor the hardware efficiency of both the range trigger and the high-p trigger. These special triggers used independent sets of counters and could not be satisfied unless each muon passed through all the counters used in the trigger being checked. The trigger that was used to monitor the high-p trigger required a coincidence of IBV, Z1, Z3, Z5 and T4 or S3. The T4 or S3 requirement forced the muons to have passed through the counters of Z6. The efficiencies of both the high-p trigger and the range trigger were

checked throughout the run and were always greater than 99%.

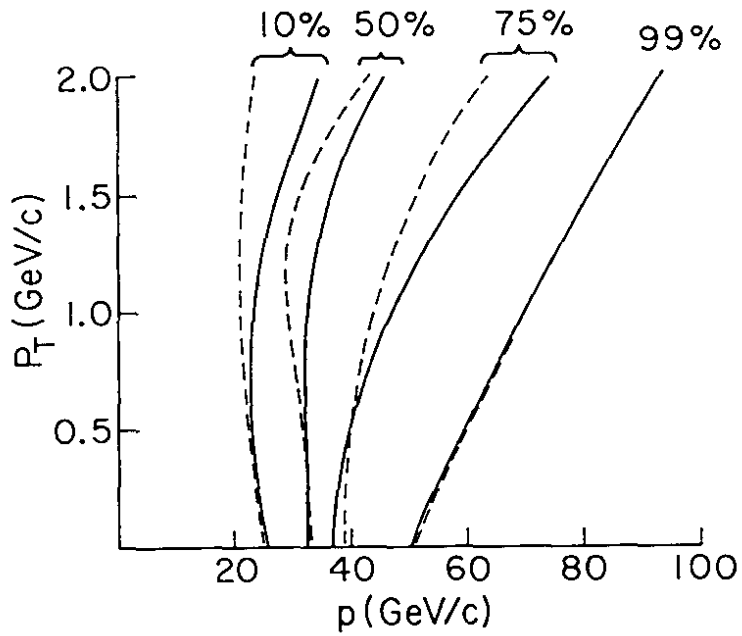

Figure 2-11: Contours of constant efficiency versus p and p_T for both signs of muons for the high-p trigger (solid lines for μ^+ and dashed lines for μ^-).

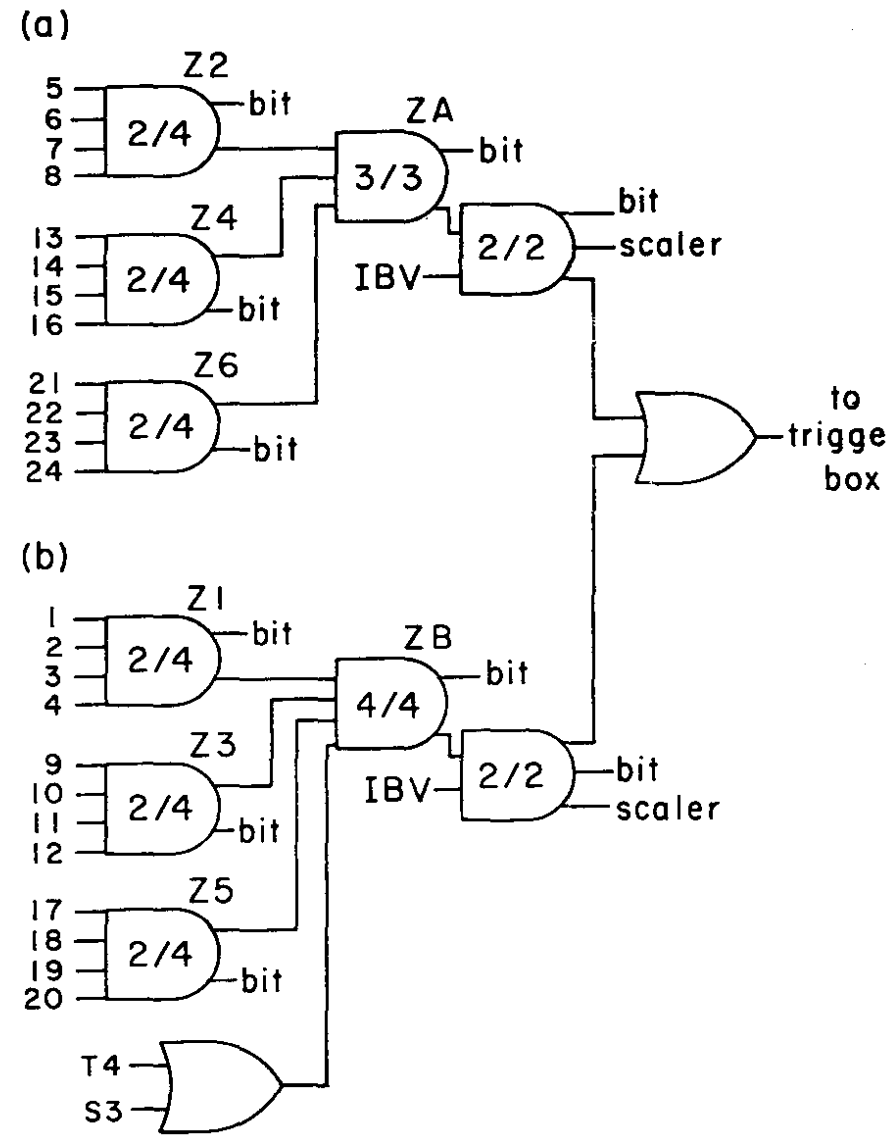

Figure 2-12: Logic diagram of (a) the high-p trigger and (b) the trigger used to monitor the hardware efficiency of the high-p trigger.

2.4 Data Taking Procedures

Data were taken during a 1.5 second "slow spill." During each spill, several types of record were written onto magnetic tape. They were:

(i) Begin Spill Record. This record contained pulse height histograms accumulated between spills from reference phototubes which viewed a radioactive Americium source embedded in a NaI(Tl) crystal. These histograms were used in monitoring the calorimetry counter gains. Reference 19 contains a more complete description of the calorimetry (gain monitoring, flasher system, etc.) than this thesis will present.

(ii) Pedestal Record. This record contained pulse height information (from all the ADC's) recorded during a gate generated just before the beginning of the spill.

(iii) Calorimeter Flasher Record. This record contained pulse height information from the calorimeter counters recorded by the "event" ADC's during an LED pulse and also by the "flasher" ADC's during a subsequent flasher pulse.

(iv) Muon Identifier and Toroid Flasher Record. The counters in the muon identifier and the toroid acrylic counters were monitored by another flasher

system which was separate from the calorimeter system.

(v) Event Record. This record was written when a trigger occurred. It contained all the information (latches, ADC pulse heights, spark locations, etc.) from the entire detector.

(vi) End Spill Record. This record contained NaI histograms accumulated during the spill and the scaler information. Numerous signals generated by the detector were scaled, most of them gated on livetime. The most important was IBV. The number of livetime IBV's was used in the analysis, described in Chapters 4 and 5, to normalize the number of muon triggers to the number of interacting beam particles.

During a typical spill about 25 event records were written to tape (along with one of each of the other record types). The beam intensity was adjusted to maintain the livetime in the range of 50% to 60%.

Data were taken at three different densities of the target-calorimeter, but in fact, in five different configurations of the target-calorimeter. Three of these, COMPACTED, SEMI-EXPANDED and EXPANDED, have been described earlier. The remaining two had the same effective density as COMPACTED. The use of the data from these other configurations will be described later. During both the proton and the pion running, data were

taken in each of the five configurations three different times. Data were taken in this "cyclic" manner in order to make it possible to look for time dependent detector effects. None were found.

The data taken with the target-calorimeter in any particular configuration were divided equally between two modes of running, referred to as "low intensity" and "high intensity." In the low intensity mode neither the range trigger nor the high-p trigger was prescaled. Since the range trigger rate was the larger by roughly an order of magnitude, the muon triggers consisted of about 90% range and 10% high-p triggers. Because the trigger rate was large in this mode (about 20×10^{-4} triggers/IBV for COMPACTED proton running), the beam intensity was kept quite low, only 10 to 20 thousand particles (depending on density) per pulse. In the high intensity mode the range trigger was prescaled so that the division of muon triggers was roughly 90% high-p and 10% range. The beam intensity was $1\text{-}2 \times 10^5$ particles (depending on density) per pulse.

Prescaled IBV's were triggered on in both modes of running. The prescaler values were chosen to cause IBV triggers to be about 20% of all triggers for each density and mode. These interaction triggers provided an important means of measuring various systematic effects, as will be described in Chapters 4 and 5.

CHAPTER 3

EVENT RECONSTRUCTION

Each triggering event was written onto magnetic tape for later analysis. The first stage in the "off-line" analysis consisted of converting the raw information, such as wire numbers, pulse heights, etc., into physical parameters such as position, energy and momentum. This process of event reconstruction was carried out by computer programs which read the raw data tapes, analyzed them and then wrote new tapes containing the results of the reconstruction programs. The important physical parameters to calculate from the data on an event-by-event basis were: the trajectory and momentum of the incoming beam particle (and whether, in fact, there was only one particle); the energy deposited in the target-calorimeter and the longitudinal distribution of this energy (i.e., the shower shape); and the number of

muons produced, their trajectories and momenta. This analysis was performed by four separate algorithms acting upon data from four different parts of the detector. These algorithms will be briefly described in this chapter.

3.1 PWC Tracking

The algorithm for the tracking of beam particles with the beamline PWC spectrometer can be viewed as consisting of three steps:

(i) Unpacking of Raw Data. The PWC data written onto tape indicated which wires had hits in a given event. These wire numbers had to be converted into positions in real space. The conversion required a knowledge of the wire spacing and the position of a reference wire within the chamber. The positions of the chambers, and therefore the positions of the reference wires inside, were known approximately from an optical survey. The chamber positions were optimized by picking two horizontal measuring chambers, and two vertical measuring chambers, and using beam tracks to calculate corrections to the positions of the remaining chambers with respect to these reference chambers. Such a procedure was

adequate because only the relative positions of the chambers, with respect to each other, had to be known precisely.

(ii) Search for Straight Segments. Finding tracks in an unmagnetized region consists of looking for hits that lie along a straight line. In this case, three separate searches were made, each in a different set of PWC's. One set consisted of the horizonal measuring PWC's upstream of the bending magnets. Another consisted of the horizontal measuring chambers downstream of the magnets, and the third set consisted of all the vertical measuring chambers. To be accepted, a segment had to have a minimum number of hits, the number being different for each set of chambers (since the number of chambers was different in each region; see Figure 2-4). Also, the segment had to pass a cut on the quality of the fit to the straight line hypothesis.

(iii) Momentum Calculation. The momentum of a particle may be calculated from the angle by which its path is deflected in passing through a known magnetic field. Having found horizontal segments both upstream and downstream of the bending magnet as described above, it would have been simplest to take the angle of deflection to be the difference between the directions of these two segments. However, a

better method was used. A least squares fit was performed in which two straight lines which were constrained to intersect at the bend point (i.e., at the center of the spectrometer magnet) were fit through the hits belonging to the two previously found segments. The momentum was then calculated from the bend angle determined from this fit, yielding a significantly better resolution than the simpler approach. Histograms of the reconstructed beam momenta were shown in Figures 2-1 and 2-2 for the proton beam and the pion beam, respectively. As discussed in Section 2-1, the measured momentum spread of the diffracted proton beam was consistent with the expected resolution of this system, and that of the pion beam was consistent with the momentum resolution folded in quadrature with the expected momentum bite of the beam.

3.2 Calorimetry

The purpose of the calorimetry software was to convert the raw pulse heights from the individual scintillation counters in the target-calorimeter into an energy. In so doing, several corrections, such as for time dependent drifts in calibration, ADC non-linearities and rate dependent effects, were made. A detailed descripion of these algorithms can be found in Reference 19. The prompt single muon results described in this thesis, however, do not depend upon a precise hadronic energy measurement. Therefore, these details will not be addressed here.

In general, hadronic energy measurement with a sampling calorimeter, such as the one used in this experiment, depends upon measuring the number of charged particles at different depths in an absorbing medium. The total energy is simply the number of charged particles in the shower multiplied by the depth of material they penetrated and the amount of energy lost per unit length. This value, however, is incorrect to the extent that small amounts of energy are "lost" in breaking up nuclei (binding energy), or carried away by muons and neutrinos, or lost due to "leakage" because of the finite size of the calorimeter (i.e., if a calorimeter is not large enough to completely contain the

showers, then the energy of the particles which escape the calorimeter will not be included in the measurement). Neutral particles (except neutrinos) ultimately interact, thereby producing charged particles which are counted.

In this experiment, the hadronic energy was calculated by first dividing the pedestal subtracted pulse height from each of the 49 calorimetry counters by a "calibration constant" which was determined for each counter. This gave the effective number of minimum ionizing particles passing through each counter. The energy for each counter was this number times the thickness of the plate in front of the counter and the dE/dx loss in steel (per unit length) for a minimum ionizing particle. The total energy was just the sum of the energies in the individual counters.

The method of calibration used has been described in Reference 19. Briefly, a first estimate of each calibration constant was derived from the response of each counter to a muon beam. Then a fit was performed, varying all the constants subject to two conditions: (1) the mean hadronic energy had to agree with the known beam energy and (2) the average shower profile had to be independent of where in the calorimeter the incoming beam particles interacted. By choosing the calibration constants to give the correct mean energy with a known energy beam on target, the binding energy and any other

"lost energy" effects were accounted for. After calibration the only effect of such energy losses on the calorimetry is to degrade the resolution slightly. This is due to the fact that the smaller the fraction of the total shower energy that is observed, the greater the sensitivity of the energy measurement to shower fluctuations.

The shower shape information (i.e., the energy in each counter) thus obtained can be used to ascertain several important quantities, such as the location of the hadronic interaction and the length of the shower. In fact, as will be described in Chapter 5, shower length information does play an important role in the analysis of the data taken with a pion beam. The shower profile for a typical 350 GeV proton interaction is shown in Figure 3-1.

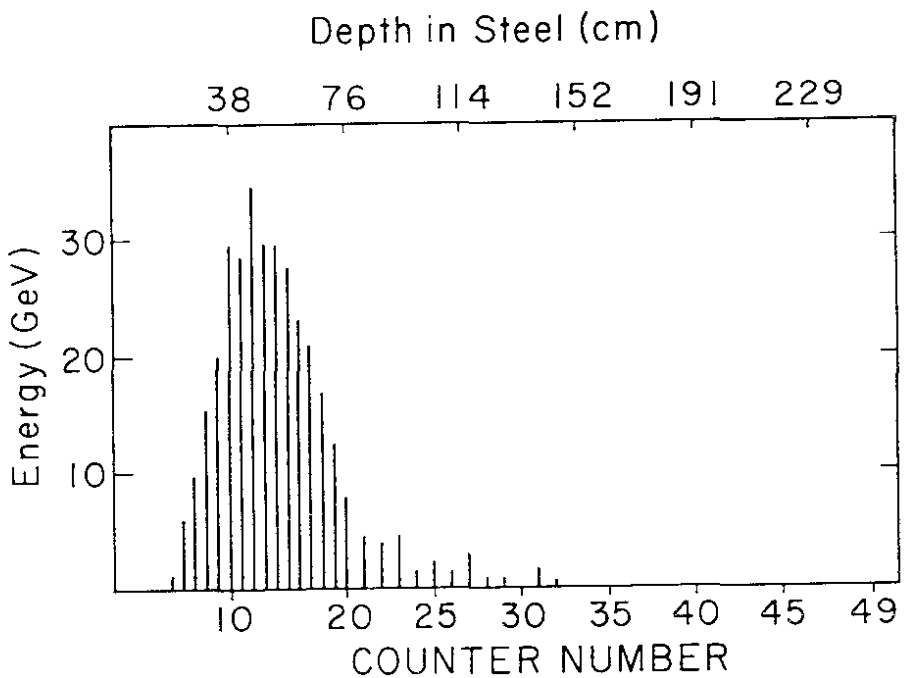

Figure 3-1: The shower profile of a typical 350 GeV proton interaction as measured in the target-calorimeter. The pulse heights shown have been converted to energy in GeV. The steel thickness was 3.8 cm for the first 20 counters, 5.1 cm for the next 25 counters, and 10.2 cm for the final 4 counters.

3.3 Muon Identification from Counters

The scintillation counters in the muon identifier were used not only in triggering, but also in the identification of muons. This provided a method which was totally independent of the spark chambers for determining the number and, in some cases, the energy of muons. Each of the 42 counters provided a pulse height which was the sum of the four phototubes viewing the counter. These pulse heights were converted to number of minimum ionizing particles by dividing by the mean pulse height determined from a sample of "clean" single muon events. Then a fit was performed to the distribution of minimum ionizing particles versus counter number (i.e., depth in the muon identifier) to find the number and range of muons that most likely produced the observed distribution. This fit is illustrated in Figure 3-2. The reliablity of the fit can be ascertained from Figure 3-3 which shows the difference in the ranges measured by the counters and the spark chambers for both single muon events and the lower energy muon in dimuon events. The range measurement of the lower energy muon in dimuon events was less precise than that for single muons, and was more often overestimated than underestimated. The role of this fit in the analysis will be described in Chapter 4.

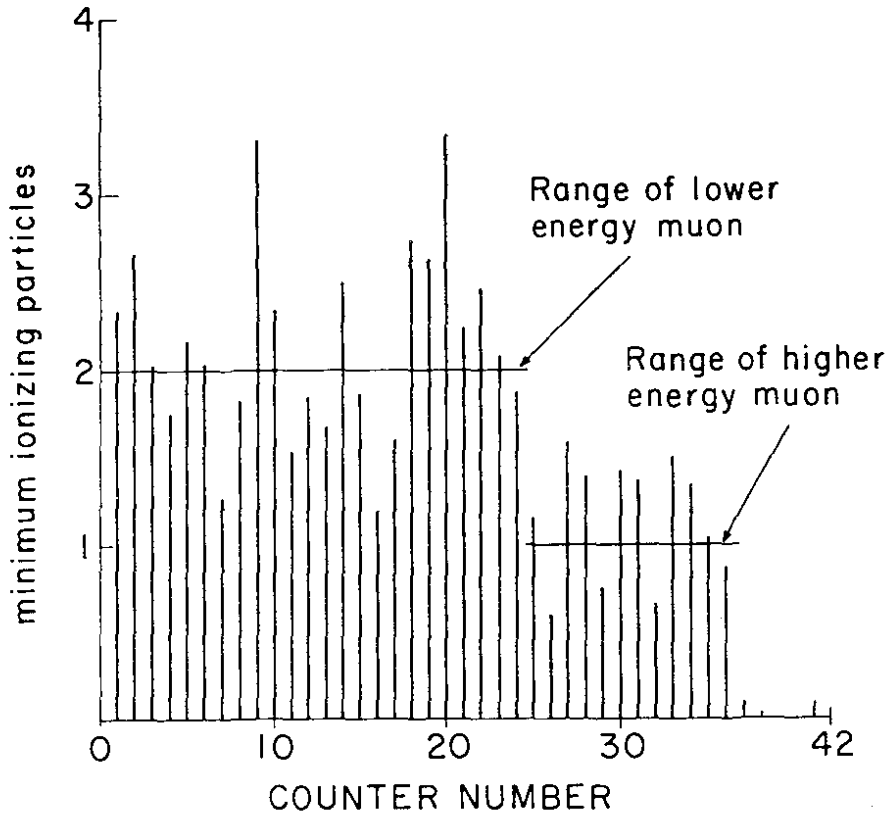

Figure 3-2: Illustration of muon range fit. Shown are the pulse heights in the 42 muon identifier counters in units of minimum ionizing particles for a single event. The solid line shows the results of the fit to the number and ranges of muons.

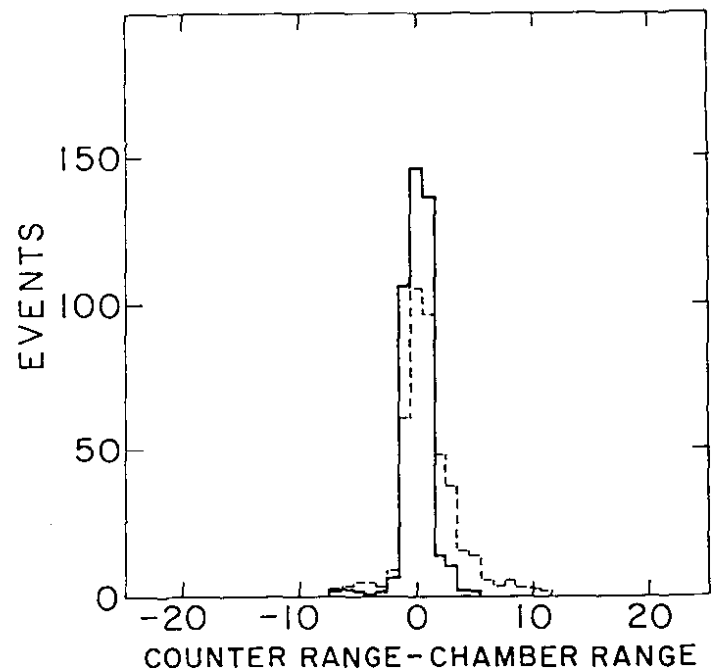

Figure 3-3: Histograms of the difference between the ranges of muons calculated from the muon identifier counters and the spark chambers. The solid histogram is for single muon events in which the muon stopped in the muon identifier. The dotted histogram is for the lower energy muon in dimuon events. The two distributions are normalized to the same number of events. The counters are separated by 10.2 cm of steel.

3.4 Muon Tracking

The positions of muons passing through the detector were measured by the spark chambers. Algorithms were used to find tracks from the measured spark positions, to calculate track directions, and for tracks that went through the toroid spectrometer, to calculate their momenta. These algorithms are summarized below. The tracking can be viewed as a three step process:

(i) Unpacking the Raw Sparks. The position of a spark in one of the spark chambers was calculated from the time it took the acoustic pulse (generated by the spark) to travel down the magnetostrictive wand. It was this time, along with the times of two reference sparks, called fiducials, that was actually recorded. (For each wand up to 16 sparks, including fiducials, could be recorded.) The first step in the analysis of the spark chamber information was to convert the spark locations from "clock counts" (each count corresponded to 5×10^{-8} seconds) into positions in real space. The conversion required a knowledge of either the positions of both fiducials, or equivalently, the position of one fiducial and the speed of sound in the wand. The fiducials were a known, fixed distance apart so that the time difference between them could be used to calculate

the speed of sound for each wand. By keeping a running average of the speed of sound for each wand small variations (due to temperature dependence, for example) were corrected for. The position of the first fiducial for each chamber was known approximately from an optical survey. More accurate positions were later calculated using high energy muon calibration data.

(ii) Finding Tracks. Tracks were first sought in the muon identifier (which was unmagnetized), where finding tracks amounted to finding straight segments. Finding tracks in the toroid spectrometer, however, was complicated by the magnetic field which bent tracks by an amount which depended on momentum. The algorithm used did not search for tracks in the toroid. Rather, it tried to trace, or "swim," tracks which had been previously found in the unmagnetized regions into the toroid. As can be seen from Figure 2-3, several planes of spark chambers occupied an unmagnetized region downstream of the toroidal magnet. Tracks found in this region were the first to be extrapolated into the magnetized region. Sparks belonging to these tracks were flagged as used. Tracks found in this way were then "linked" to the appropriate tracks from the muon identifier. Finally, any remaining muon identifier tracks were

extrapolated into the toroid and followed to the point where they exited the toroid.

(iii) Calculating the Muon Momenta. The calculation of momentum in the toroid spectrometer was complicated by multiple scattering in the iron disks that comprised the magnet. A fit which included the extra multiple scattering parameters was performed. The momentum resolution obtained was approximately ±11%. The momentum reconstruction was checked with calibration muons at several momenta, as described in Chapter 2. A small (less than 2%) momentum dependent correction was calculated from these calibration data and has been applied on an event-by-event basis. Figure 3-4 shows the reconstructed momentum distributions for two different calibration momenta. It should be noted that the resolution is not expected to be gaussian in momentum (p), but rather in 1/p, since the multiple scattering angle, which has a gaussian distribution, is proportional to 1/p. The tails on the low momentum side of the distributions shown in Figure 2-4 are consistent with expected energy loss distributions for muons passing through iron.

The transverse momentum of each muon was calculated by multiplying its momentum by the angle (strictly speaking, the sine of the angle) its trajectory made with

respect to the incoming beam particle. The angle was determined from the locations of the sparks in the first 6 muon identifier spark chambers which had a spark associated with the track. The longitudinal position of the interaction in the target-calorimeter was not used in the calculation (even though in principle the p_T resolution could have been improved by doing so) since that would have coupled the p_T measurement to the positions of the target-calorimeter plates. In order for the density extrapolation method to work properly, it is necessary that the resolution not depend on density. Therefore, p_T was calculated in a way which guarenteed density independence, but at the price of some loss in p_T resolution.

In order to assure a good p_T measurement it proved necessary to impose a cut on the χ^2 calculated from a fit of the first 6 sparks on each track to a straight line (in both the horizontal and vertical views). This meant that some events could not be used for the measurement of p_T distributions. The fraction of single muon events rejected by this cut ranged from .13 for COMPACTED to .17 for EXPANDED. This mild density dependence resulted from the fact that the number of sparks in the upstream most spark chambers increased as the density was reduced because of low energy particles escaping out the sides of the target-calorimeter. The extra sparks increased the

probability that a wrong spark would be assigned to a track. Such errors were eliminated by the χ^2 cut.

The p_T resolution was poor because each muon had to penetrate around 3 meters of steel before the measurement of its angle was made. Multiple Coulomb scattering in the steel limited the p_T resolution to about $(.021\ \mathrm{GeV/c}) \times (L/X_0)^{.5}$, where L is the length of steel and X_0 is the radiation length in iron (1.76 cm). For L = 300 cm this corresponds to a resolution of .27 GeV/c. The p_T resolution was measured from the p_T distributions of calibration muons (for which the true p_T was zero) to be .29 GeV/c.

An interesting check on the tracking and momentum reconstruction was provided by the ψ, the only mass peak accessible to this experiment. Figures 3-5 and 3-6 show the mass distributions obtained for opposite sign dimuons with 350 GeV protons and 278 GeV pions incident, respectively. Fits to a gaussian plus an exponential background yielded masses of 3.11 ± .03 GeV for the proton data and 3.08 ± .02 GeV for the pion data, both in excellent agreement with the ψ mass, 3.097 GeV. The ψ', at a mass of 3.685, is produced at the level of about 2% of the ψ in hadronic interactions at these energies, and therefore introduces a negligible (about .01 GeV) shift in the apparent ψ mass.

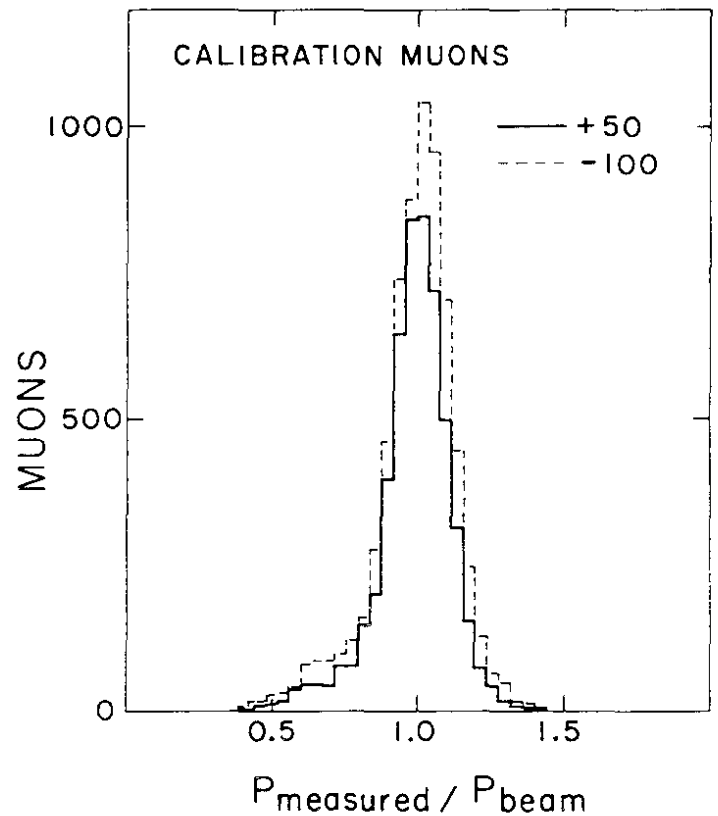

Figure 3-4: The reconstructed momentum distributions for calibration muons of +50 and -100 GeV/c. The momenta have been divided by the beam momenta so that different beam settings could be shown on the same plot. Note: The small momentum correction discussed in the text has not been applied to this data.

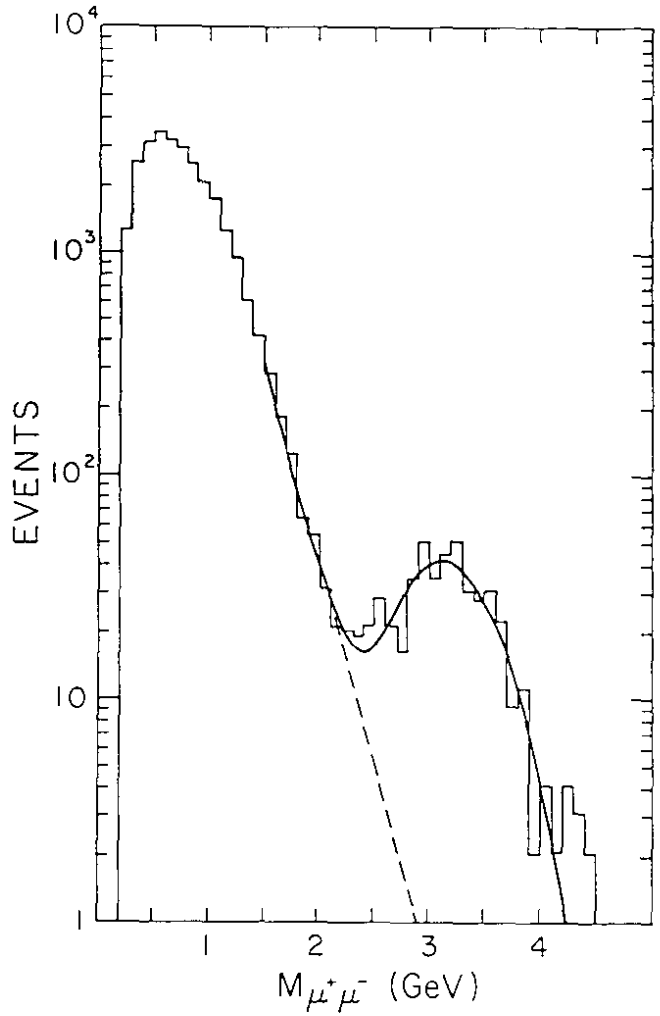

Figure 3-5: Mass distributions of opposite sign dimuons produced by 350 GeV protons. The solid curve shows the fit to a gaussian plus an exponentially falling background. The dotted curve shows the background beneath the ψ.

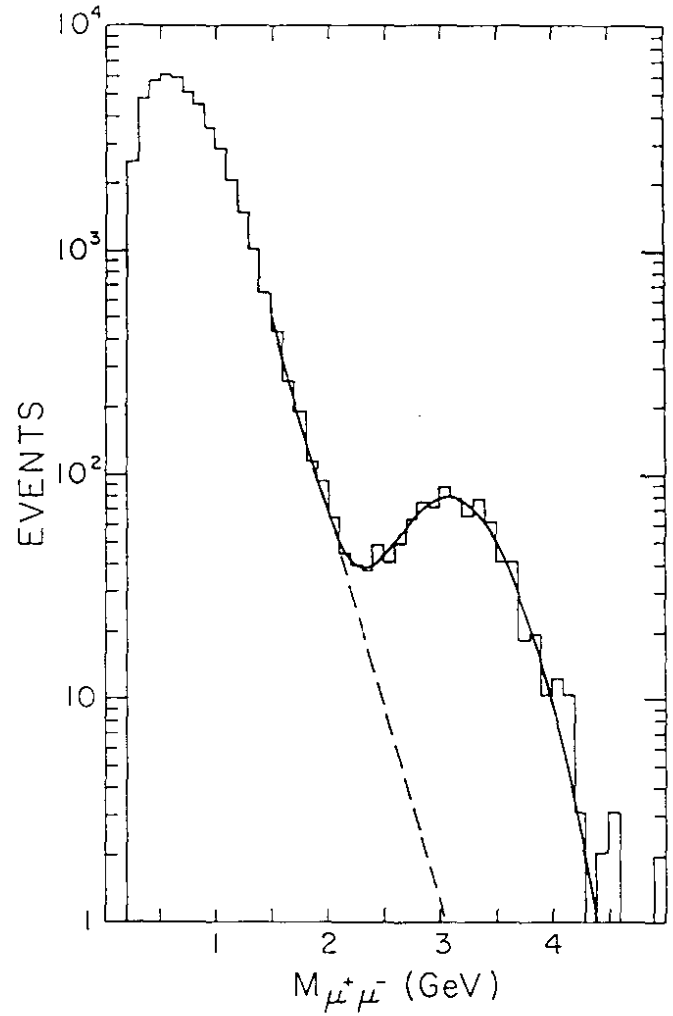

Figure 3-6: Mass distributions of opposite sign dimuons produced by 278 GeV pions. The solid curve shows the fit to a gaussian plus an exponentially falling background. The dotted curve shows the background beneath the ψ.

CHAPTER 4

ANALYSIS OF PROTON HIGH P DATA

The analysis of the 350 GeV proton high-p data leading ultimately to prompt single muon rates versus momentum p and transverse momentum p_T will be described in this chapter. The first phase of this analysis is the calculation from the data of "raw" prompt rates, as will be described in Section 4.1. The second phase, to be described in Section 4.2, is the calculation of the backgrounds which must be subtracted from these raw rates. Final prompt single muon rates and distributions will be presented in Section 4.3.

It is worthy of comment that the analysis of the pion high-p data, which will be discussed in Chapter 5, closely parallels that of the proton data described here. Indeed, the methods of analysis are identical, with the single exception of one background which must be removed

from the pion data that is not present in the proton data (triggers from beamline muons which interacted in the target-calorimeter). Therefore, most of the explanations of the analysis procedures will be presented in the present chapter and will not be repeated in Chapter 5.

4.1 Data Analysis

Data were taken in five different configurations of the target-calorimeter and in two different modes of running (high intensity and low intensity), as described in Chapter 2. In order to provide an introduction to the data, Table 4-1 shows the numbers of high-p triggers recorded, the numbers of interacting beam (IBV) triggers recorded, and the numbers of livetime IBV's on target (from scalers) for each configuration and mode.

Trigger rates, in the simplest possible case, are determined by dividing the number of triggers by the number of beam particles incident on the target. However, in an actual experiment, both of these numbers must be calculated for a restricted set of data selected by making "cuts" which eliminate spurious triggers, obvious backgrounds, etc. Therefore, the first step in the analysis of this experiment was event selection. The second step was the classification of events as either

single muon events or multi-muon events. Then the single muon rates could be calculated. Finally, the rates from different target-calorimeter densities were combined via the density extrapolation technique to arrive at the raw prompt single muon rates. These steps will be addressed separately below.

Table 4-1: Shown are the numbers of high-p triggers and interacting beam triggers recorded, and the number of livetime IBV's on target for the proton data, for each configuration of the target-calorimeter for both high and low intensity running.

High Intensity

Configuration	High-p trig	Int. Beam trig	IBV (live) ($\times 10^8$)
COMPACTED	147161	33319	6.6733
SEMI-EXPANDED	109574	21834	3.8418
EXPANDED	149800	23440	4.2411
SPECIAL 1	147674	36249	6.7910
SPECIAL 2	81545	22379	3.6666

Low Intensity

Configuration	High-p trig	Int. Beam trig	IBV (live) ($\times 10^8$)
COMPACTED	10783	23982	.4829
SEMI-EXPANDED	11268	27183	.4012
EXPANDED	12108	33479	.3454
SPECIAL 1	13093	30879	.6121
SPECIAL 2	6262	13676	.2802

4.1.1 Event Selection

Several cuts were made to eliminate events which might for one reason or another cause systematic errors in the evaluation of rates. By doing so, a clean sample of events with well understood properties was obtained. These cuts can be logically separated into two classes. One class consisted of those cuts which were placed on the beam particle. Such cuts will be referred to as IBV cuts since they may be thought of as re-defining IBV in software (see Section 2.3.1 for a discussion of IBV). It should be noted that IBV cuts reduce the effective flux of interacting hadrons on target. They do not change the acceptance of the trigger. The other class of cuts consisted of those cuts which were placed on the muons (usually only on the triggering muon in an event). These cuts are logically different from the IBV cuts because (1) they do not reduce the flux and (2) they can, depending upon the details of the cut, reduce the acceptance of the trigger. Because of this natural, and important, distinction between IBV cuts and muon cuts, they will be addressed separately.

4.1.1.1 IBV Cuts

An effect of IBV cuts, as remarked above, is to reduce the flux (in this experiment, the word "flux" refers to the number of livetime IBV's). The effect of the cuts on the flux is determined by making them on the interacting beam triggers that were written to tape. Since they were selected randomly, the fraction of these events rejected by the cuts should be the same as for all IBV's. However, since only about 20% of all triggers were interacting beam triggers, the statistical error in the determination of this fraction can become the dominant source of statistical error in the calculation of rates if the fraction is large. For example, if 125,000 high-p triggers were collected along with 25,000 interacting beam triggers (numbers which can be seen from Table 4-1 to be typical), the relative error from the flux determination would be the equal to that from the number of triggers (.35%) if the fraction of events rejected were 20%. If the fraction were larger than 20% the flux error would dominate. On the other hand, the error in the rates would not be significantly improved by making the fraction much less than 20%. Since IBV cuts can eliminate potential sources of systematic errors, it is a good idea to make rather stringent cuts so long as the flux error does not become dominant. This philosophy

has been followed, particularly in the case of the PWC tracking where each event is basically required to be "perfect." Even so, only about 10% of the IBV's were rejected. The IBV cuts applied to the data were:

(1) Events were rejected if the HALO pulse height exceeded .1 minimum ionizing particle. Recall from the discussion of beam logic (Section 2.3.1) that an IBV could not occur if there was a hit in HALO. Therefore, this software condition was redundant and served only to "back-up" the hardware. This condition removed only about .5% of the events, most of these probably resulting from soft particles emitted backwards from the hadronic interactions in the target-calorimeter rather than from HALO inefficiency.

(2) Events were rejected based on the PWC tracking information:

(i) Events were rejected unless one and only one track segment was found. As described in Section 3.1, independent searches were performed for straight line track segments in the horizontal plane both upstream and downstream of the bending magnets and in the vertical plane. Events were rejected unless one and only one segment was found by each of these three searches.

(ii) Events were rejected if the momentum fit yielded a bad χ^2. The fit was described in Section 3.1. The

χ^2 distribution is shown in Figure 4-1. Events were rejected if the χ^2 exceeded 5.

(iii) Events were rejected if the momentum determined by the PWC fit was more that 2.5% away from the central beam momentum. This corresponded to a requirement of 350 ± 8.75 GeV/c for the proton beam. Since the proton beam was narrow in momentum, this was a very loose cut (see Figure 2-1).

(iv) Events were rejected if the trajectory determined by the PWC tracking did not extrapolate through B1, the smallest beam defining counter.

(v) Events were rejected if the trajectory of the beam particle did not extrapolate to within ±3 cm of the beam center at the downstream end of the toroid spectrometer.

(3) Events were rejected if the visible energy in the event exceeded 1.2 times the nominal beam energy (i.e., 420 GeV for the proton data). The visible energy for most IBV triggers amounted to the energy deposited in the target-calorimeter. However, for events with muons, the muon energies were added to the calorimeter energy before applying this cut. This condition eliminated both events with two hadrons and events with a hadron and a muon incident. It had only a small effect on the proton data, but as will be seen in Chapter 5, was important for the pion data analysis. Table 4-2 gives the fluxes for each

density and mode after the IBV cuts have been applied.

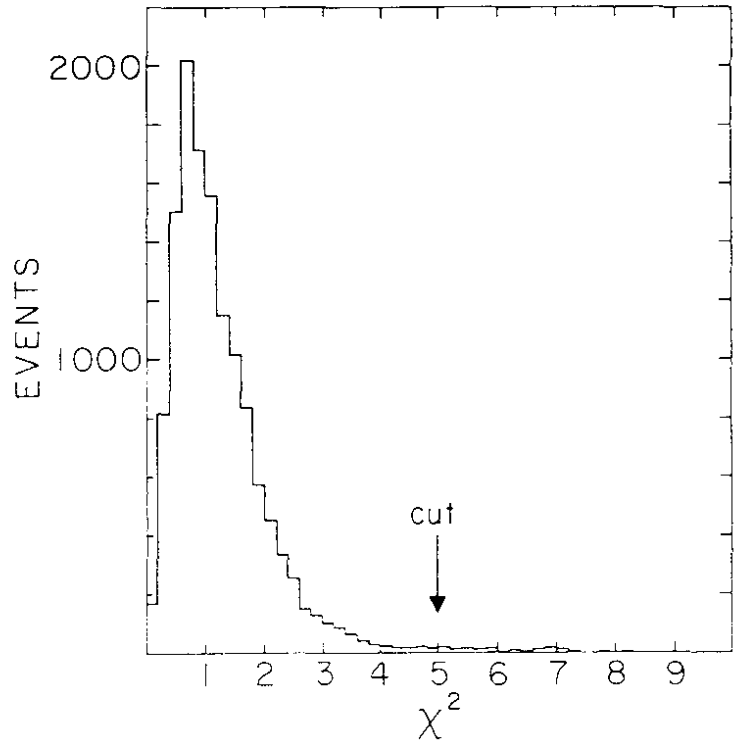

Figure 4-1: Histogram showing the χ^2 distribution from the PWC momentum fit. Events whose χ^2 exceeded 5 were rejected.

Table 4-2: Effective fluxes after IBV cuts for each target-calorimeter configuration for both high and low intensity.

Configuration	livetime IBV's (× 10^8) High Intensity	Low Intensity
COMPACTED	6.0382 ± .0119	.4578 ± .0007
SEMI-EXPANDED	3.6046 ± .0067	.3886 ± .0004
EXPANDED	4.0247 ± .0064	.3365 ± .0003
SPECIAL 1	6.3931 ± .0089	.5986 ± .0005
SPECIAL 2	3.4110 ± .0067	.2666 ± .0005

4.1.1.2 Muon Cuts

Muon cuts were imposed on the events for three reasons: (1) to reject events in which a halo muon in coincidence with an IBV caused a trigger (so-called "accidentals"), (2) to reject events in which the triggering muon did not penetrate all the toroid acrylic counters (the reason for this will be explained below), and (3) to equalize the acceptance of the trigger for different beam conditions. The muon cuts are described below. The first three rejected accidentals, but did not affect the trigger's acceptance. The fourth (which addressed the second and third goals) was a geometrical cut on the position of the track in the toroid spectrometer, and did affect the acceptance.

(1) Events were rejected if the pulse heights observed in the muon identifier counters were not consistent with the passage of at least one muon.

(2) Events were rejected if the triggering muon (the exact meaning of the term "triggering muon" will be explained below) did not originate in the target-calorimeter. In particular, a quantity, D_{min}, was calculated from the tracks found in the muon identifier. It was the distance of closest approach of the muon to the beam center in the neighborhood of the target-calorimeter. Figure 4-2 shows a histogram of D_{min}

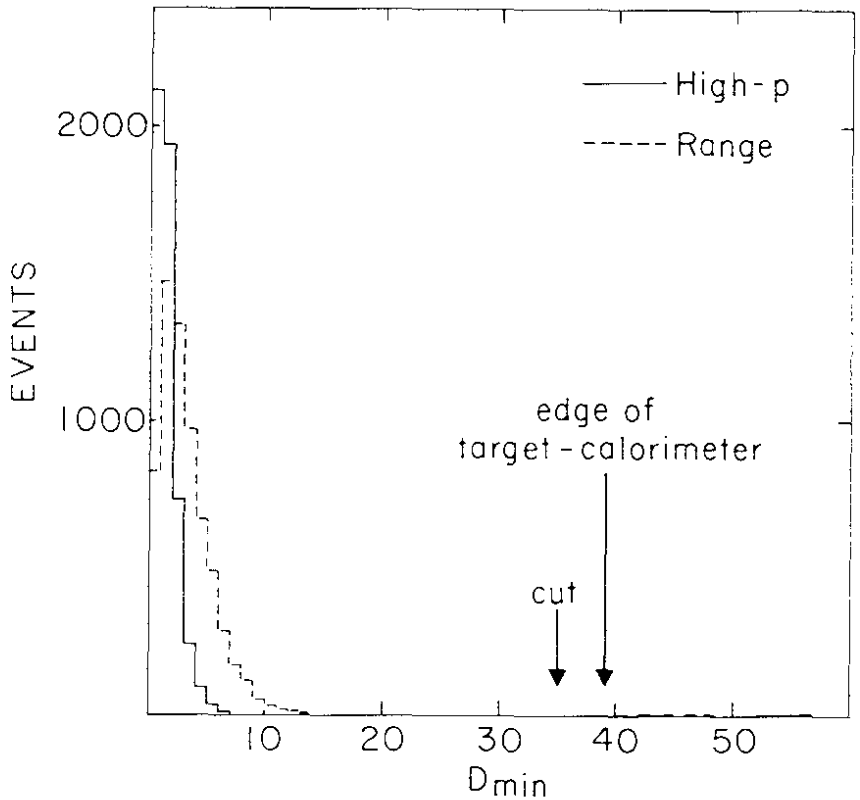

Figure 4-2: The D_{min} distributions for 5254 high-p triggers (solid line) and 6502 range triggers (dotted line).

for both high-p and range triggers. Since range trigger muons had less momentum on average, the distribution is broader for range triggers than high-p triggers due to multiple Coulomb scattering. D_{min} was a good variable on which to cut because it was less sensitive to multiple scattering than the "naive" vertex obtained by extrapolating the muon tracks back to the interaction point. Events with D_{min} greater than 35 cm were rejected. In Chapter 5 it will be seen that this cut was very powerful in eliminating accidentals triggers from the pion data. However, in the proton data there were few accidentals to eliminate.

(3) Events were rejected if there was a hit in C47 (calorimeter counter number 47), but no signal from the "in-time" bit (see Section 2.3.1 for a description of the in-time bit). This eliminated events in which the muon was not within ±5 nanoseconds of the interacting hadron. Only events with a hit in C47 were candidates for rejection so that events would not be rejected merely because of an inefficiency in counter 47 (the efficiency of C47 was typically about 98%).

(4) Events were rejected unless a muon in the event passed a geometrical requirement, which was imposed in two steps:

(i) The position of each muon track after every four toroid disks was compared to the edges of the acrylic

counters. If a track did not lie 3 cm or more inside the counters at each of the six points of comparison, then it was declared ineligible to trigger. If no muon in an event passed this test, the event was rejected. Any muon which passed the test is referred to as a "triggering muon." (Note that in dimuon events, by this standard, both muons can trigger.) Basically, two types of events were rejected by this geometrical cut. One type consisted of events in which Z6 (see Section 2.3.2) fired by accident, apparently because of "cross talk" in the electronics. These triggers were about 2 to 3% of the high-p triggers. The other type consisted of triggers in which the Z6 requirement was satisfied by a coincidence of only S20 and S21 (recall Z6 required only 2 of 4 of S20 through S24). That is, the muon left the toroid "early," before it passed though all the toroid acrylic counters. This topology was not spurious or unexpected; low momentum muons were typically bent out of the toroid. However, in order to properly calculate the hardware efficiency of the high-p trigger using the method described in Section 2.3.2 it was necessary to guarantee that the triggering muons passed through all four of the counters in Z6.

(ii) Those "triggering muons" that passed the first

test had to pass an additional requirement. The trajectory of the incoming beam particle, as measured by the PWC spectrometer, was extrapolated to the downstream end of the toroid spectrometer. (Recall that an IBV cut rejected events in which the distance between the extrapolated position and the beam center was more than 3 cm.) The "outline" of the acrylic counters was then centered on the extrapolated position. Muons which did not still lie 3 cm or more inside this shifted counter boundary were declared inelgible to trigger. The effect of this test was to equalize, event by event, the acceptance for muons produced in interactions initiated by hadrons which struck the target-calorimeter in different positions or with different incident angles. This condition, while desirable in principle, had little effect since the beam was not broad in either position or angle, and was stable over time (a small shift in the angle of the beam did occur during part of the high intensity SEMI-EXPANDED running, but was not of sufficient magnitude to introduce problems).

The geometrical requirement raised the minimum momentum accepted because it required greater penetration than the hardware trigger. In all calculations of acceptance this geometrical cut has been included.

4.1.2 Event Classification

High-p triggers were either single muon events or multi-muon events. Multi-muon events were over 99% dimuon events. The remaining events contained three muons. The rate for these tri-muon events was consistent with that expected for normal dimuons in coincidence with an extra muon from pion decay. All multi-muons events will hereafter be referred to as dimuon events.

High-p triggers were classified as either single muon (1μ) or dimuon (2μ) events based on a criterion that relied on both the scintillation counters and spark chambers in the muon identifier.

Events were classified as dimuons if: (1) the muon range fit (see Section 3.3) yielded a best fit of two muons with the range of the lower energy muon greater than or equal to 12 counters <u>and</u> there were at least two track segments (with four or more sparks on each) in either the horizontal or vertical view, or (2) the range fit preferred two muons with the range of the lower energy muon greater than or equal to 38 counters. However, tracks for which the horizontal and vertical views were "mated" (almost all of them) had to have D_{min} less than 35 cm to be counted; that is, an event with two muons was called a single muon event if one of the muons was clearly unassociated with the interaction.

The penetration of 12 muon identifier counters, or about 3.8 meters of steel (2.4 of which were in the target-calorimeter), corresponded to a minimum momentum of about 5.2 GeV/c. The choice of this as the minimum range for the identification of a second muon represented a compromise between two competing considerations. On one hand, the greater the penetration, the more reliable the determination of the number of muons (because more counters and spark chambers can be used, there is less hadronic punch-through, etc.). On the other hand, the greater the penetration required, the larger the background from asymmetric dimuons (i.e., pairs with one high momentum and one low momentum muon) in the single muon class.

The muon range fit was used to determine the penetration of the lower momentum muon because it was more reliable than the spark chamber tracking. As muons near the end of their range, multiple Coulomb scattering becomes enormous, making it difficult to fit straight lines through the sparks. Often the last spark associated with the track can be several centimeters away from the straight line trajectory indicated by the more upstream sparks, making an unambiguous range determination impossible. However, the fit to counter pulse heights was also not perfect, and as remarked in Section 3.3, overestimated the range of the lower

momentum muons in a few percent of cases. Therefore, the requirement that two segments also be found was imposed. This substantially reduced the number of mistakes due to the range of the second muon being overestimated by the fit.

Events with a calculated second muon range of 38 or more counters were classified as dimuons independent of any tracking requirement in order to protect against high energy low mass dimuons (i.e., pairs with a very small opening angle) which might be so close together that either the spark chambers could not resolve them or the tracking algorithm could not sort them out. (In fact, this was unlikely because multiple Coulomb scattering would tend to spread them apart.) It was safe to use the counter condition alone in this case because the probabilty of the fit overestimating the range by 26 counters is exceedingly small.

It is important, of course, to understand the reliability of these classification criteria. This will be discussed in Section 4.2.2.

4.1.3 Rate Calculation

The calculation of rates for single muons and dimuons amounts to dividing the number of events in these

categories by the flux. The events can be binned in momentum and transverse momentum to get the rates as a function of these variables. However, a small correction must be applied for "extra" single muons causing single muon events to be classified as dimuons. That is, there are events with two muons that are not dimuons in the proper sense. Rather, in these events, a single muon is accompanied by an extra muon which was also from one of the sources of single muons (the decays of pions, kaons, hyperons, or charmed particles). The contribution of these events must be subtracted from the dimuon rates and added to the single muon rates.

The rate for these extra single muon events is just the "true" single muon rate times the probability of a muon with a range of greater than 12 counters occurring in any given event. Call this probablity P_{12}. Then the true single muon rate $R_{1\mu}^{true}$ is related to the measured single muon rate $R_{1\mu}^{meas}$ by the relation

$$R_{1\mu}^{meas} = R_{1\mu}^{true} - P_{12}R_{1\mu}^{true}.$$

Therefore,

$$R_{1\mu}^{true} = R_{1\mu}^{meas}/(1 - P_{12}),$$

or

$$R_{1\mu}^{true} = R_{1\mu}^{meas} (1 + P_{12}).$$

The last equation is valid because P_{12} is small (about .01). Since the total number of events should not change, the true dimuon rate is given by

$$R_{2\mu}^{true} = R_{2\mu}^{meas} - P_{12}R_{1\mu}^{meas}.$$

The values of P_{12} can be determined from IBV triggers and are given for different target densities in Table 4-3. However, these values were calculated from events most of which did not contain muons. The high-p triggers, on the other hand, did have muons which on average carried away about 50 GeV. And, since there were muons, there must also have been neutrinos which carried away still more energy. The effect of this on P_{12} is difficult to ascertain. But it is reasonable as an approximation to assume that P_{12} for a 350 GeV interaction in which 60 GeV was carried off by leptons is the same as P_{12} for a 290 GeV interaction. The same energy is available for the hadronic showers in both cases.

In this experiment a small number of special runs

with low momentum negative hadron beams were conducted. The rate for muons with momentum greater than 8 GeV/c is given by the range trigger rate. The COMPACTED range trigger rate is shown versus beam energy in Figure 4-3. This rate, as well as the non-prompt rate for muons with momentum greater than 8 GeV/c which is also shown in Figure 4-3, appears to depend approximately linearly on the beam energy. Therefore, the dependence of P_{12} (which is after all only the rate for muons with momentum greater than 5.2 GeV/c) has been assumed to be linear with the <u>hadronic</u> energy (i.e., $E_{beam} - E_{leptons}$). The prescription for calculating $E_{leptons}$ was to multiply the muon momentum by 1.25, a factor which gives the correct average momentum in the case of pion decay, the dominant source of these muons. This correction was applied bin-by-bin in momentum when calculating rates.

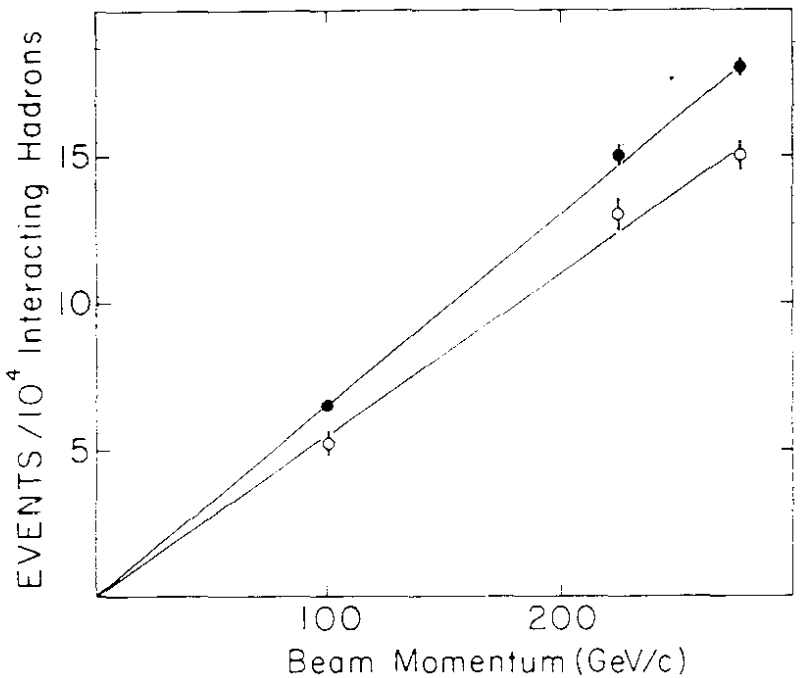

Figure 4-3: Range rates versus momentum of negative hadron beam. The solid points are the range trigger rates for the COMPACTED configuration. The open circles are the EXPANDED rates minus the COMPACTED rates, which give the rates from non-prompt sources. The lines are drawn only to illustrate that both are approximately proportional to beam energy.

Table 4-3: The probability per event P_{12}^{raw} that a muon penetrated into the muon identifier to a depth of 12 counters, corresponding to 5.2 GeV/c in momentum, measured from IBV triggers, is given for each target-calorimeter configuration. Also given are the momentum averaged values of P_{12} after the correction, described in the text, for energy dependence has been applied for both μ^+ and μ^- events separately.

Configuration	P_{12}^{raw} (%)	$P_{12}^{\mu^+}$ (%)	$P_{12}^{\mu^-}$ (%)
COMPACTED	.68 ± .04	.56 ± .03	.57 ± .03
SEMI-EXPANDED	.88 ± .04	.73 ± .04	.74 ± .04
EXPANDED	1.35 ± .05	1.12 ± .04	1.14 ± .04
SPECIAL 1	.59 ± .03	.49 ± .03	.50 ± .03
SPECIAL 2	.74 ± .05	.61 ± .04	.62 ± .04

4.1.4 Density Extrapolations

Once single muon rates have been calculated for each calorimeter density, density extrapolations must be performed to separate the prompt and non-prompt components. The principles underlying the density extrapolation method were discussed in Section 1.2.2. In practice, a density extrapolation simply amounts to performing a least squares fit of the rates versus inverse density ($1/\rho$) to the hypothesis of a straight line. The intercept at $1/\rho = 0$ is the prompt rate and the slope of the line is the non-prompt rate.

Dimuon rates should exhibit no dependence on density (all "real" dimuons are prompt). This fact provides an important systematic check that single muon events are not being misclassified as dimuon events.

Figure 4-4 shows the rates for four classes of events plotted versus inverse density (where $\rho = 1$ refers to the density of the COMPACTED target-calorimeter configuration). The four classes are: (1) single triggering positive muon ($1\mu^+$), (2) single triggering negative muon ($1\mu^-$), (3) dimuon with triggering positive muon $(2\mu)^+$, and (4) dimuon with triggering negative muon $(2\mu)^-$. Note that the third and fourth classes are not mutually exclusive since a positive muon and a negative muon in the same event can both pass the cuts placed on

the triggering muon. Clearly, the single muon rates vary linearly with inverse density, while the dimuon rates are flat. The raw prompt $1\mu^+$ rate is 11.14 ± .90 per 10^6 interacting protons (IBV's) and the raw prompt $1\mu^-$ rate is 10.51 ± .74 per 10^6 interacting protons. These rates contain background contributions which must be removed. Even so, note that the prompt $1\mu^+$ and $1\mu^-$ rates, before background subtractions, are approximately equal. The slope of the $1\mu^+$ line is larger than the slope of the $1\mu^-$ line simply because more positive pions than negative pions are produced with a proton beam.

The data can be binned in momentum p and transverse momentum p_T, and density extrapolations can be performed for each bin to determine the prompt and non-prompt distributions. Sample density extrapolations are shown in Figure 4-5 for muons of both signs in the momentum bins from 30 to 40 GeV/c and from 60 to 80 GeV/c.

Data were taken with the target-calorimeter in five different configurations, as discussed in Section 2.4. Three of these configurations, COMPACTED, SEMI-EXPANDED and EXPANDED, have been described. The remaining two, referred to as SPECIAL 1 and SPECIAL 2, had the same

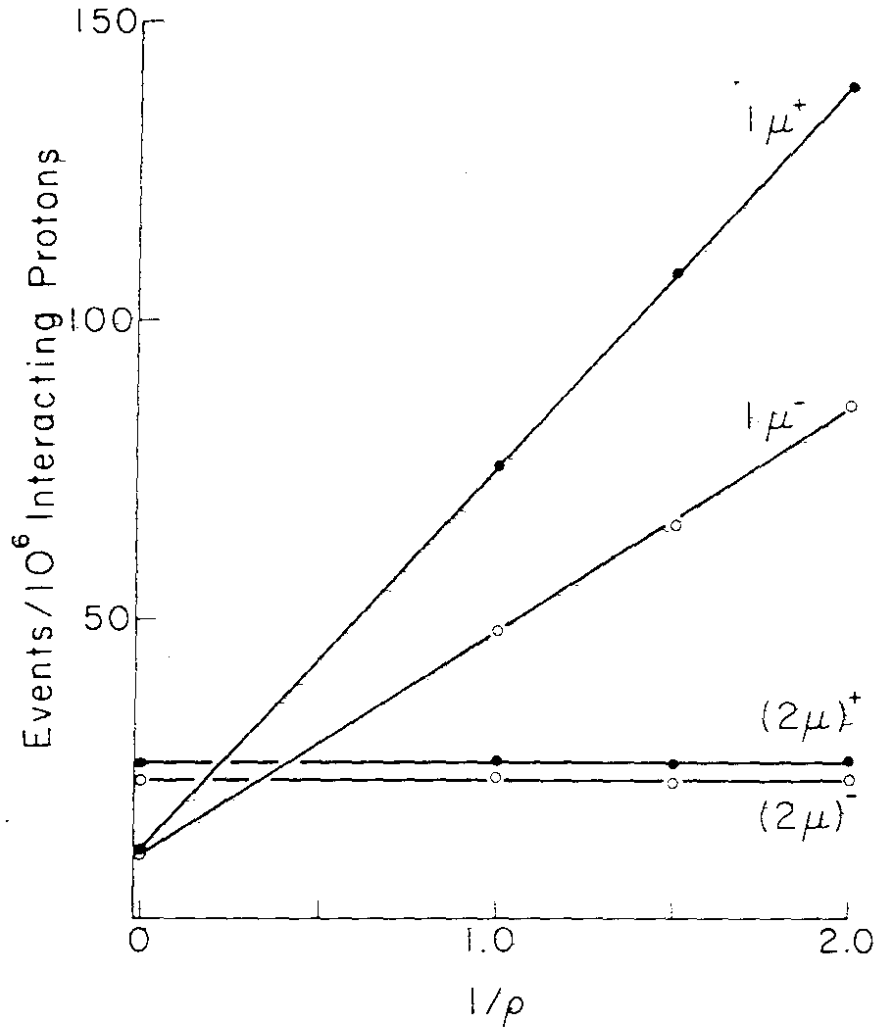

Figure 4-4: Rates for positive muons (solid points) and negative muons (open circles) for four categories of events (defined in the text) versus inverse density.

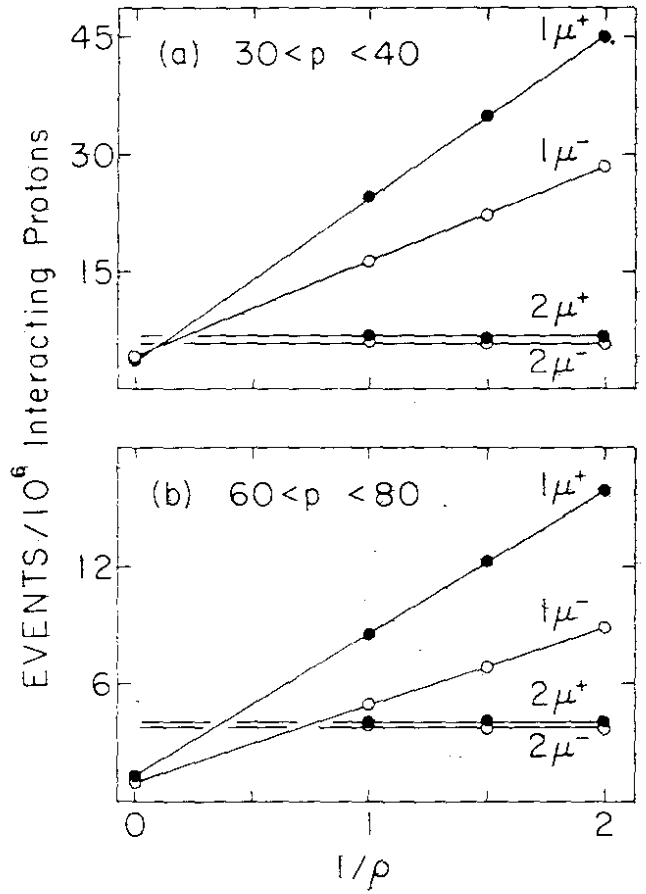

Figure 4-5: Density extrapolations in bins of momentum:
(a) $30 < p_\mu < 40$ (GeV/c) and
(b) $60 < p_\mu < 80$ (GeV/c).
The four categories of events are defined in the text.

effective density as COMPACTED. For SPECIAL 1, all of the plates were displaced downstream, as a unit, by 164.5 cm from their COMPACTED positions. For SPECIAL 2, the positions of the first 38 plates were unchanged from their COMPACTED positions, but gaps were placed between the last 11 plates. Data were taken in these two special configurations in an effort to measure the rate of apparently prompt muons (i.e., the background rate) from pion and kaon decays in the last 11 plates (which were not "expanded" in any of the three regular configurations) or in the gap between the last plate and the muon identifier. (The length of this gap depended on calorimeter configuration. It was longest, 164.5 cm, for COMPACTED, and was eliminated completely for EXPANDED.) This background will be discussed in Section 4.2.5.

The data taken in the SPECIAL 1 configuration differed from the COMPACTED data in two ways: (1) the acceptance was different because the interaction point was 164.5 cm farther downstream and (2) the contribution due to pion and kaon decays in the gap was not present (this contribution was only about .04% of the non-prompt rate, and was concentrated at low muon momentum). Of these two differences, only the first is really significant; the second is smaller than the statistical error on the rates measured in either configuration. The

acceptance difference is a few percent at low momentum. High momentum muons were not deflected as much by the magnetic field of the toroids, and consequently were less likely to pass near enough to the edges of the toroid acrylic counters for a small change in the "solid angle" to matter.

Although it is not possible (in a model independent way) to correct these two data sets to the same acceptance, it is possible to determine the momentum above which the acceptances are the same. For each muon that enters the muon identifier the horizontal angle θ_x and the vertical angle θ_y are measured. If any given muon, produced in either calorimeter configuration, had been produced in the other configuration, the effect on its trajectory would be a simple displacement Δx in the horizontal direction and Δy in the vertical direction from the actual trajectory as measured by the spark chambers. For a muon produced in the COMPACTED configuration, $\Delta x = \theta_x \cdot (164.5\ \text{cm})$ and $\Delta y = \theta_y \cdot (164.5\ \text{cm})$ in transferring to SPECIAL 1. For a muon produced in the SPECIAL 1 configuration, $\Delta x = \theta_x \cdot (-164.5\ \text{cm})$ and $\Delta y = \theta_y \cdot (-164.5\ \text{cm})$ in transferring to COMPACTED. Therefore, it is possible to determine which events would have been rejected by the geometrical cut if they had been produced in the other configuration. Muons above 80 GeV/c in momentum, it turns out, would not have been

rejected in either case.

In what follows the COMPACTED rates for muons of momentum greater than 80 GeV/c have been determined by combining the COMPACTED, SPECIAL 1 and SPECIAL 2 rates, where small corrections to the "special" rates have been included because of the pion and kaon decays in the unexpanded or gap regions. Since the interaction point was in the same position for COMPACTED and SPECIAL 2, the acceptances were probably the same at all momenta. Nonetheless, these data have been combined only above 80 GeV/c.

Figure 4-6 shows the raw prompt single muon distributions for both signs as a function of momentum. These rates were calculated as described above. Final rates, including non-prompt rates, will be given in Section 4.3.

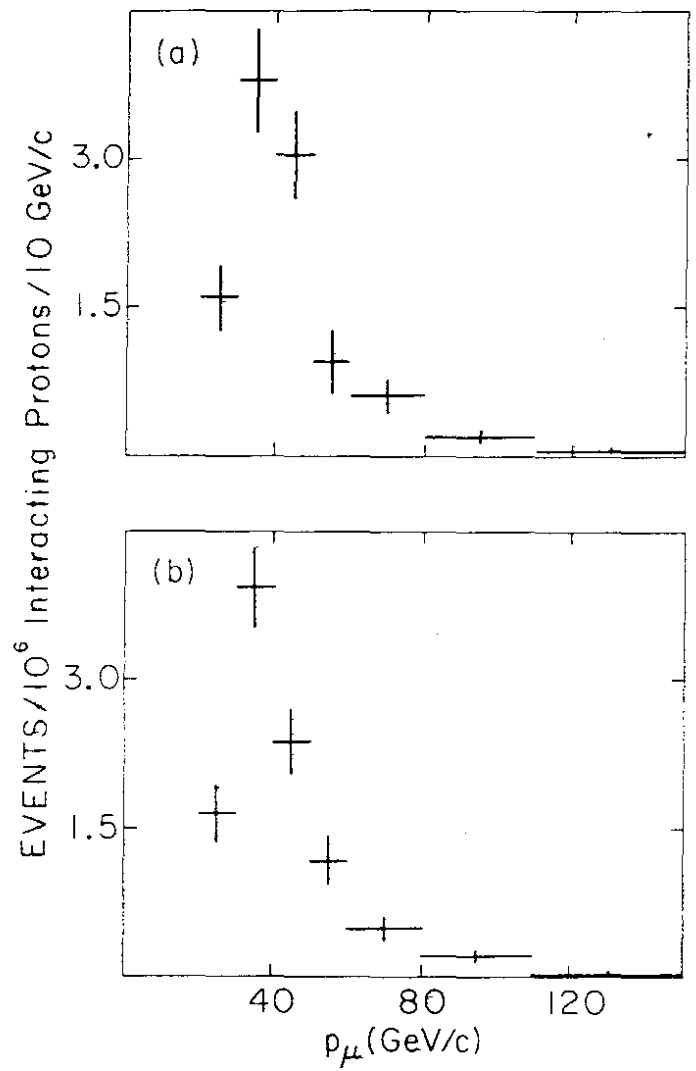

Figure 4-6: Raw prompt single muon rates (i.e., no backgrounds subtracted) versus momentum: (a) for positive muons and (b) for negative muons.

4.2 Backgrounds

The density extrapolation method allows the prompt single muon rates to be calculated. However, several possible sources of background (i.e., spurious sources of apparently prompt muons) must be investigated. All known sources have been investigated. Only one background source proves to be large, highly asymmetric dimuons which are classified as single muons because the lower energy muon, the "second" muon, penetrated to a depth of less than 12 counters in the muon identifier. While this was a small fraction of all dimuon events, it accounted for about 40% of the raw prompt single muon rate.

The potential background sources will be addressed one at a time below.

4.2.1 Accidentals

Accidentals are events in which a muon from an upstream source coincided with an IBV closely enough in time to provide a trigger. The rate for such events would not increase linearly with inverse density, so that they would appear to be prompt.

The beam for the data under consideration consisted almost exclusively of protons. Therefore, the most

obvious source of muons, pion and kaon decays in the beam, was not present. However, protons lost from the beam could interact in beam pipes or magnets, thereby producing pions and kaons which could decay to muons. Also, the beamlines of other experiments could contribute to a flux of muons through the detector. The single muon rates from such accidentals should be a function of beam intensity. For muons associated with the N5 beamline, the rate would increase as the beam intensity squared since both the number of IBV's and the number of muons would increase approximately linearly with beam intensity. If the muons were from a source other than the N5 beamline, the accidentals trigger rate should still increase linearly with intensity because of the higher rate of IBV's (of course, in this case it might also be a function of time, but the rates show no dependence on time).

Most of the event selection criteria described in Section 4.1.1 rejected accidentals. These cuts were developed, as a matter of fact, to eliminate accidentals from the pion data where accidentals constituted a much larger fraction (about 10%) of the high-p triggers. Since these cuts were successful in eliminating accidentals from the pion data, as will be shown in Chapter 5, it is natural to expect that in this less demanding situation they would also be successful.

Evidence that this is indeed the case is shown in Table 4-4, which gives the rates for single muons for both high and low intensity running for each target calorimeter configuration. There is no indication of a beam intensity dependence. A more complete discussion of accidentals will be provided in Chapter 5.

Another question that must be addressed is whether the muon cuts which eliminated accidentals triggers also eliminated good triggers. To investigate this question, a special run was conducted in which the beam intensity was reduced to about 500 particles per pulse. At this low beam intensity it is assured that almost none of the triggers were accidentals. Of the 1157 events which passed the IBV cuts and geometrical cut on the triggering muon, none were rejected by the other muon cuts (D_{min} requirement, in-time bit, etc.). This means that less than one in 1157 good events are rejected. Therefore, no correction for the rejection of good events need be applied.

Table 4-4: Single muon rates (positives and negatives summed) after event selection cuts for each configuration of the target-calorimeter for both high and low intensity running. The rates exhibit no dependence on beam intensity, indicating that "accidentals" have been successfully removed. The rates are expressed in units of 10^6 interacting protons.

Configuration	High Intensity ($\times 10^{-6}$)	Low Intensity ($\times 10^{-6}$)
COMPACTED	123.75 ± .47	127.57 ± 1.67
SEMI-EXPANDED	174.42 ± .71	174.70 ± 2.12
EXPANDED	226.45 ± .77	227.27 ± 2.60
SPECIAL 1	122.73 ± .45	122.04 ± 1.43
SPECIAL 2	125.26 ± .62	126.71 ± 2.18

4.2.2 Misclassification of Events

There are three ways in which events could have been misclassified: (1) events containing only one muon (i.e., "real" single muon events) could have been called dimuons, (2) dimuons with a second muon which ranged out before penetrating 12 muon identifier counters could have been called dimuons (a mistake because of the definition of the dimuon category), and (3) dimuons with both muons penetrating the required amount of steel could have been called single muons. Each of these three types of mistake would lead to an error in the evaluation of the prompt single muon rates. They are addressed individually below.

(1) Single muon events could be classified as dimuons. Of the three possible mistakes, this is the least likely. It not only would require the range fit to make a very large error (12 counters), but also would require two track segments to be found where only one was present. In fact, practically all such spurious segments were due to muons not associated with the event, either halo muons or muons from previous interactions for which all the ionization had not dissipated (the memory time of the spark chambers was about 800 nanoseconds). In either case, it remains unlikely that the event would be misclassified. In the former case, the D_{min} requirement

would probably reject the segment, and in the latter case, the range fit would have to err by 12 counters.

The data can be used to investigate this type of error. One way is to scan events which have been classified as dimuons to see if any were really single muons. To maximize the sensitivity of this scan, it was conducted on data taken in the EXPANDED configuration of the target-calorimeter, since in that configuration the single muon rate was largest with respect to the dimuon rate. A scan of 500 EXPANDED dimuon events yielded no single muon events. Since the EXPANDED single muon rate (both signs) was 227 per 10^6 IBV's and the dimuon rate was 45, it follows that less than one in 2522 single muon events were misclassified as dimuons, corresponding to an error in the final prompt single muon rates of less than .05%.

Another way to investigate this is to look at the density dependence of the dimuon rates. Since dimuons are prompt, the dimuon rates should be independent of target-calorimeter density. If a fraction of the single muon events were being misclassified as dimuons, then the dimuon rates would increase with inverse density. No such increase in dimuon rates was observed, but the power of this check was limited by statistics. A least squares fit of a straight line to the dimuon rates versus inverse density yielded a slope of $-.14 \pm .32$ and $-.85 \pm .30$ per

10^6 IBV's for $2\mu^+$ and $2\mu^-$ events, respectively. While these values are consistent with zero, they do not rule out a fake prompt single muon background as large as 5% of the final prompt signal. However, from the results of the scan it is clear that this possible source of error was negligible.

(2) Events with two muons, one of which ranged out before reaching counter 12, could be classified as dimuons (recall that the "dimuon" category, as defined, consists of events where both muons penetrated 12 or more counters). This effect must be present at some level since the range fit could overestimate the range of a low energy "second" muon by a few counters quite easily. The question is, how large is the effect? Also, it should be realized, this error is basically due to a resolution; that is, due to the measurement error from the range fit which can overestimate or underestimate the range. Therefore, to the extent that the resolution was symmetric, no net error is incurred (i.e., as many were overestimated as underestimated, and the two cancel). However, from Figure 3-3 it would appear that the resolution was not symmetric, and again the question becomes, how large is the effect?

The answer, or at least a good estimate, can be obtained by calculating the second muon's range from the spark chamber information for events which have passed

the 12 counter range requirement. The spark chamber range, as discussed in Section 4.1.2, is not always reliable. Therefore, a reduced set of events was defined for which the spark chamber range was more reliable: those events for which the second muon range from sparks in the horizontal view agreed with the range from sparks in the vertical view. It was found that .67% of the dimuons passing the range fit requirement had a spark chamber range corresponding to less than 12 counters. Before relating this to a prompt background, the "canceling" error should be investigated.

(3) Dimuons (both muons traversing 12 or more counters) could be classified as single muon events. This type of error could occur in either of two ways: it could result from an inefficiency in the tracking, since two track segments were required for an event to be called a dimuon, or as discussed above, it could result from the range fit underestimating the range of the second muon.

Tracking inefficiency was investigated by scanning a sample of events for which the range fit favored a second muon of range 12 or more, but in which two segments were not found. The scan was performed on a data sample in which there were 4258 identified dimuons. There were 274 events in which the range fit favored a second muon of range equal to 12 or more counters, but in which no

second track segment was found. Of these 274 events, the scan indicated that 5 events had visible segments which were missed by the tracking algorithms. Therefore, tracking inefficiency was responsible for the misclassification of 5 in 4263 dimuons, or only .12%.

The magnitude of the effect of the range fit underestimating the range of second muons was obtained by once again looking only at dimuon events for which the ranges calculated separately from sparks in the horizontal and vertical views agreed. The outcome was that .38% of the events which should have been classified as dimuons were not so classified. This means that a net error of about .2% was made in the classification of dimuons; in particular, it seems that the dimuon rates were overestimated by about .2%. This corresponds to an error of about .3% in the raw prompt single muon rates. The error from the highly asymmetric dimuon events for which both muons were not observed will be discussed in the next section, and there it will be found that about 40% of the raw prompt single muon rates must be attributed to dimuons. In comparison to this large contribution, and in particular, in comparison to the error in the subtraction of this contribution, the misclassification background can be seen to be negligible. Even after the subtraction for the unobserved dimuons, the error due to the

misclassification of dimuons in the prompt single muon rates is still less than 1%.

4.2.3 Highly Asymmetric Dimuons

Dimuon events in which the lower energy member of the pair, the "second" muon, had momentum of less than about 5.2 GeV/c (corresponding to a penetration of 12 muon identifier counters) were classified as single muon events. These events were prompt, so they contributed to the raw prompt single muon rates which were calculated via the density extrapolation method. These "fake 1μ" events had to be removed. This was accomplished with the aid of a Monte Carlo calculation.

The dimuon Monte Carlo is described and its predictions compared to the dimuon distributions measured in this experiment in Appendix 1. It included the production of dimuons from the decays of the vector mesons (ρ, ω, ϕ, ψ and ψ') and also from the continuum regions below the ρ and between the resonances based on cross section, Feynmann x and p_T distribution measurements from Reference 21. Dimuons, in this calculation, were produced not only in the primary interactions, but also in the interactions of secondary hadrons produced in the primary interactions. (In fact,

only the "leading particle" from the primary interaction contributes significantly to the production of dimuons by secondaries. Dimuon production by pions and kaons produced in the hadronic cascade is very small compared to that by the leading particle.) The Monte Carlo also included dimuon production through Bethe-Heitler conversion of photons from π^0 decays. These accounted for about 15% of the dimuons.

In order to keep the model dependence to a minimum, the Monte Carlo was used to calculate only the ratio of the rate for triggering dimuons (as a function of momentum or transverse momentum) which had a second muon which penetrated to a depth of less than 12 counters into the muon identifier (corresponding to less than about 5.2 GeV/c in momentum) to rate for dimuons with both muons penetrating 12 or more counters. This ratio was multiplied by the actual observed dimuon rates bin-by-bin to arrive at the fake single muon rates. The rate for unobserved dimuons, calculated in this way, was rather insensitive to the details of the dimuon cross sections and production distributions used. The observed dimuon rates, the raw prompt single muon rates, and the calculated fake single muon rates are plotted versus momentum for both signs in Figure 4-7 and versus transverse momentum in Figure 4-8. For a more complete discussion, see Appendix 2.

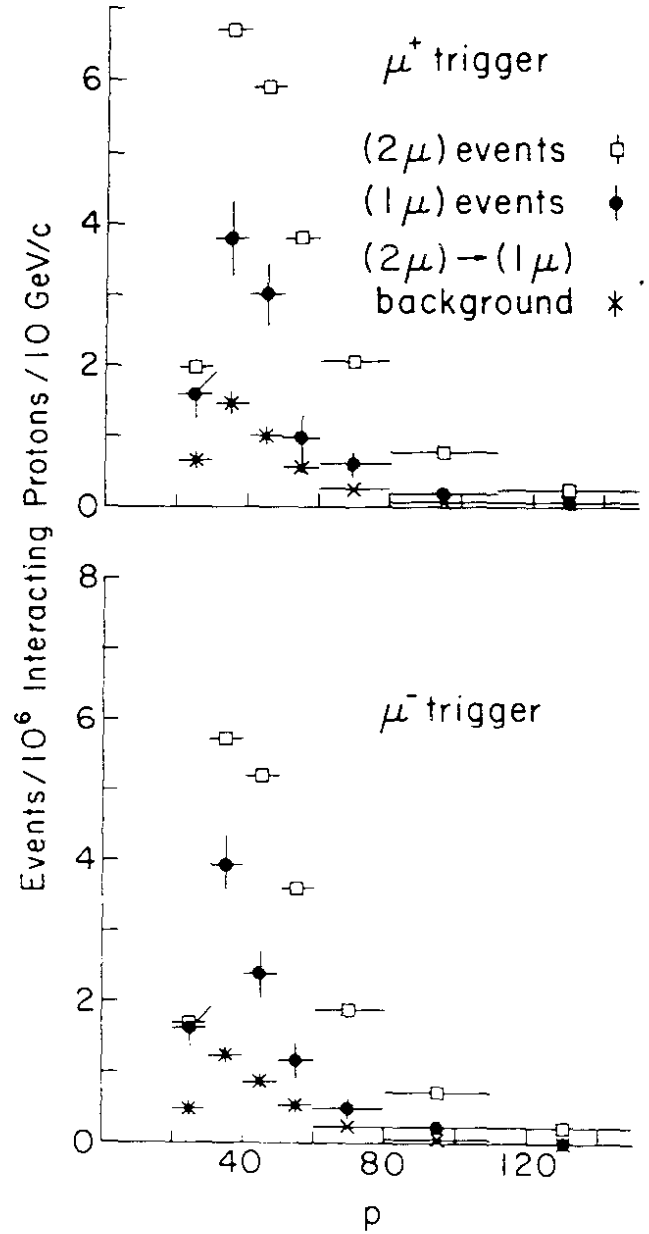

Figure 4-7: Rates for observed dimuons (open squares), raw prompt single muons (dark circles), and the calculated background (crosses) from highly asymmetric dimuons versus momentum, for events with triggering (a) μ^+'s and (b) μ^-'s.

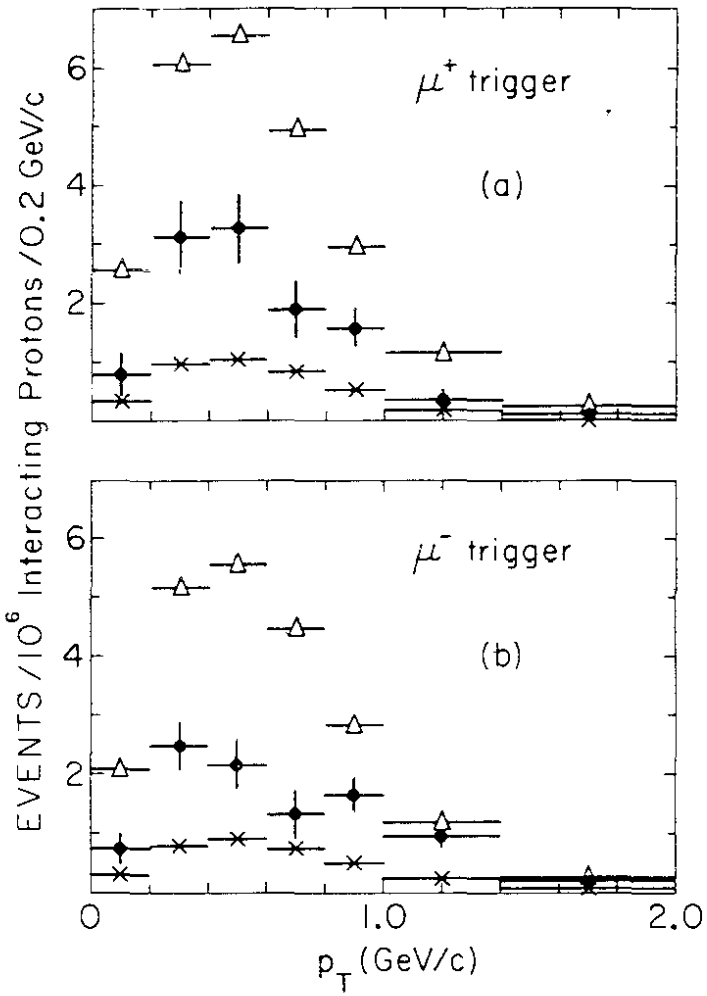

Figure 4-8: Rates for observed dimuons (open squares), raw prompt single muons (dark circles), and the calculated background (crosses) from highly asymmetric dimuons versus p_T, for events with triggering (a) μ^+'s and (b) μ^-'s.

4.2.4 Upstream Interactions

Interactions of beam particles in the material just upstream of the target-calorimeter could provide a density independent source of triggers, and therefore a fake prompt signal. This material consisted of thin titanium vacuum windows, the kapton windows and aluminum high voltage planes of the PWC's, for example, and totaled about 1.8% of an absorption length. The secondaries (mainly pions) produced in such interactions might have uninterrupted decay paths of a few meters in which they could decay to muons. Other hadrons from the interaction might somehow satisfy the IBV requirements, thereby leading to a trigger.

It should be emphasized that both hardware and software conditions imposed on the data should eliminate such background events. For example, recall that if B0 had more pulse height than twice minimum ionizing, CLBM (clean beam), and therefore IBV, was vetoed. If any of the secondaries hit HALO, IBV was vetoed. Also, events were rejected if there were extra track segments in the PWC spectrometer, or if the beam particle was more than 2.5% away from the central beam momentum. Since a particle typically loses about half of its energy in an inelastic interaction, the momentum cut alone would eliminate almost all interactions that occurred upstream

of the bending magnets.

Nonetheless, several special runs were conducted to study this background. During these runs extra material was placed in the beam. In particular, at every location, within about 50 meters of the target-calorimeter, where there was material in the beam, an additional packet of material was added. These packets consisted of the same material that was already in the beam, but ten times more. That is, the material in the beam was increased by a factor of eleven (1 + 10 = 11).

Such an increase in the material in the beam increased the number of upstream interactions by a factor of eleven. The number of triggers caused by these interactions should have increased by the same factor. By comparing the rates measured during these special runs to the nominal rates, it was possible to measure this contribution. In fact, it was found to be consistent with zero. The difference between the single muon rates (both signs summed together) for the runs with extra material and the normal data (this study was conducted for the COMPACTED configuration) was -1.94 ± 1.21 (per 10^6 interacting protons). Since the background was enhanced by the extra material, the background estimate is obtained by dividing this difference by ten, so that the result is $-.19 \pm .12$ (per 10^6 interacting protons).

Therefore, there is no evidence that upstream interactions constituted a background.

It should be noted that the above discussion does not deal with the possiblity that interactions in B0 contributed to the trigger rate. This, however, was not a problem because when the target-calorimeter configuration was changed, the distance between B0 and the first steel plate was changed by the same factor as the effective density of the target-calorimeter. Specifically, the distances between B0 and the first plate were 41 cm, 62 cm and 82 cm, for COMPACTED, SEMI-EXPANDED and EXPANDED, respectively. Because of this, the number of decays in this gap of pions and kaons produced in interactions in B0 increased linearly with inverse density and therefore contributed to the non-prompt, rather than prompt, rate from the density extrapolation.

4.2.5 Downstream Decays

Muons produced in pion or kaon decays downstream of the expanded part of the target-calorimeter (the first 38 plates, 1.7 meters of steel) would contribute to the prompt single muon rates. This downstream region, for the COMPACTED configuration, consisted of 76 cm of steel

(with effective density of 3/4 that of iron) followed by a 1.65 meter air gap. For SEMI-EXPANDED, the air gap was only half as long, and for EXPANDED, it was eliminated completely.

In an effort to measure the rate from these "downstream decays," data were taken in two special configurations of the target-calorimeter, SPECIAL 1 and SPECIAL 2. Briefly, the idea was to measure the rate from decays in the gap by subtracting the SPECIAL 1 rates from the COMPACTED rates (recall that SPECIAL 1 was the same as COMPACTED, except with all the plates displaced downstream by 164.5 cm) after equalizing the acceptance of the two configurations (see Section 4.1.4). Then the decay rate in the last 11 plates (minus the gap) was to be measured by enhancing this decay rate by a known factor of 2.75 by expanding only those plates (SPECIAL 2). This approach unfortunately proved to be statistically limited. The result was that the background rates could be anywhere from 0 to 30% of the prompt single muon rates (after the subtraction for unobserved dimuons). Obviously, a better way of evaluating this background had to be found.

For any given pion (or kaon), whose momentum and location are known, it is possible to calculate the probability that it will "survive" until it reaches the unexpanded part of the calorimeter, or the gap, and decay

there. Once the pion has decayed to a muon and neutrino, it is possible to ascertain whether the muon would provide a trigger by tracing it through the apparatus. The problem, therefore, can be addressed via Monte Carlo calculation. The only real difficulty is that the calculation depends upon the distribution of pions (and kaons) produced, and this is complicated by the fact that these particles are produced not only in the primary interaction, but also in the subsequent cascade that develops. The remainder of the calculation, the decay to muons and the propagation of muons through the detector, is well understood.

The Monte Carlo calculation is described in Appendix 2. In order to reduce the model dependence as far as possible, the Monte Carlo was used to calculate the ratio of the downstream decay rates to the decay rates in the expanded region. The measured decay rates (the slopes from the density extrapolations) were multiplied bin-by-bin by these ratios to get the background rates.

It must be remarked that the background is actually equal to the decay rate in the unexpanded steel plus <u>twice</u> the decay rate in the gap. This doubling of the gap contribution is an artifact of the density extrapolation. At $1/\rho = 2$ (EXPANDED), the gap contribution is zero, since there is no gap. At $1/\rho = 1$

(COMPACTED), if the gap rate is R_{gap}, then the extrapolation to $1/\rho = 0$ yields an intercept of $2R_{gap}$.

The total background rate (unexpanded steel plus twice the gap) was found to be .3% of the usual non-prompt rate for both positive and negative muons. The background rates are shown versus momentum in Figure 4-9. The background versus p_T was determined by multiplying the average background ratio (.3%) times the decay rates versus p_T determined from the density extrapolations. Because of the difficulty in accurately modeling a hadronic cascade, a systematic error of 100% has been used in subtracting this small background from the raw prompt single muon rates. The "downstream decays" background, then, amounts to (3.0 ± 3.0)% of the prompt single μ^+ and (1.6 ± 1.6)% of the prompt single μ^- rates (after the subtraction of unobserved dimuons). For further details of this calculation, see Appendix 2.

4.2.6 Systematic Errors in the Density Extrapolation

The density extrapolation method was discussed in Section 1.2.2, where it was shown that the extrapolation is linear to the extent that the term $\lambda_{eff}/c\tau\gamma\beta$ is negligible compared to unity. Here the question of whether there are systematic errors in the density

extrapolation, such as non-linearities, which would cause errors in the determination of the prompt rates, will be investigated. Three topics will be addressed. First, since the equations derived in Section 1.2.2 assumed that the beam dump consisted of a uniform medium, the effect of the granularity of the target-calorimeter (the finite steel plates followed by air gaps) will be discussed. Next, the question of whether the finite lifetimes of the sources of "non-prompt" muons introduce an important non-linearity in the rates versus inverse density will be treated in two parts: non-linearities from pions and kaons and non-linearities from hyperons (which sometimes decay semi-leptonically to final states containing a muon). From the values of $\lambda_{eff}/c\tau\gamma\beta$ shown in Table 1-2, it would seem that pions and kaons should not introduce a non-linearity. It should be remembered, however, that there are a lot of these particles in each interaction. Also from Table 1-2, it might seem that hyperon decays (especially those of the Ω^-) could prove problematical. In this case, however, it should be remembered that there are few of these particles (per interaction) and that their semi-leptonic branching ratios are exceedingly small (usually about 10^{-3}).

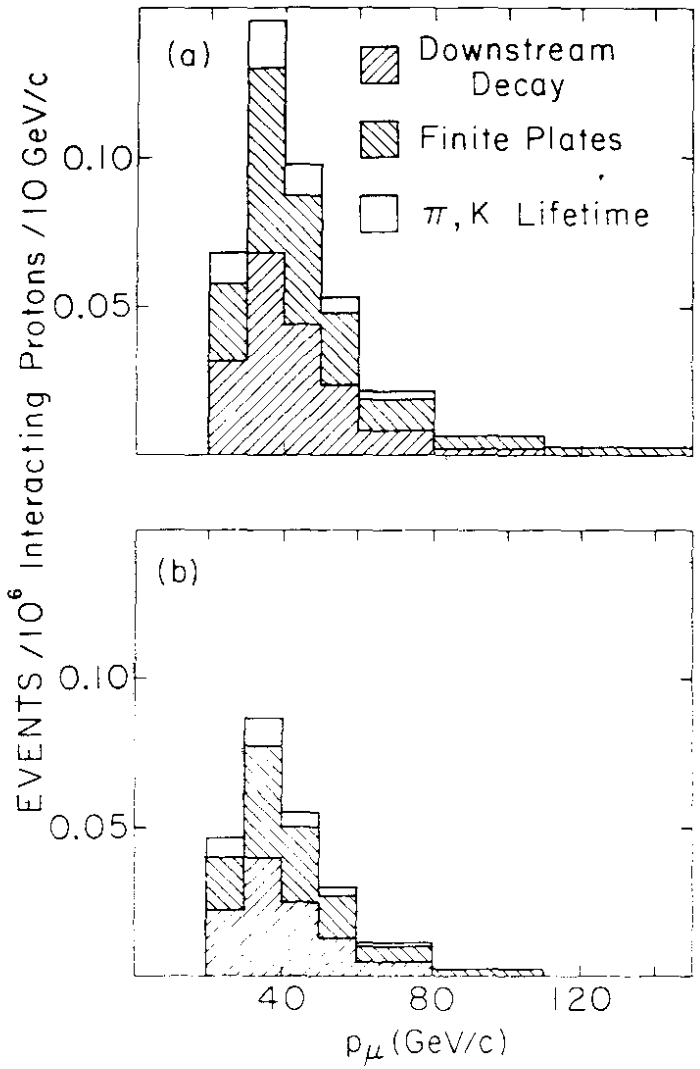

Figure 4-9: Background contributions for downstream decays and the effects due to the nonuniform density distribution of the target-calorimeter and the lifetimes of pions and kaons: (a) for positive muons and (b) for negative muons.

4.2.6.1 Finite Plate Thickness

The effect on the density extrapolation of the actual distribution of steel in the target-calorimeter (steel plates followed by air gaps) can be calculated. This calculation is given in Appendix 3. The result is that the granularity of the target-calorimeter does not introduce a non-linearity, but does introduce a false positive intercept, which is equal to

$$(\ell/\lambda)^2 R_{np}/12,$$

where ℓ is the plate thickness, λ is the absorption length in steel, and R_{np} is the non-prompt rate. Here ℓ = 3.8 cm and λ = 20 cm. This background was evaluated bin-by-bin in momentum and is shown in Figure 4-9. It amounted to 3% of the prompt single μ^+ and 1.6% of the prompt single μ^- rates (after the subtraction for unobserved highly asymmetric dimuons).

4.2.6.2 Finite Lifetimes of Pions and Kaons

The quantity $c\tau\gamma\beta$ is extremely large compared to the effective absorption length of the target-calorimeter for those pions and kaons energetic enough to decay to muons

which could cause high-p triggers, as can be seen from Table 1-2. Consequently, the muon production rate from pion and kaon decays is highly linear versus inverse density. Nonetheless, this linearity is not exact, and to the extent that the rates are non-linear, a fake prompt signal (i.e., a positive intercept at $1/\rho = 0$) will result. The magnitude of this fake prompt signal has been calculated versus muon momentum using the same Monte Carlo program that was used to investigate the downstream decays background. The calculation included three generations of the hadronic cascade, and it was verified from the contribution of each of these generations that the values were converging to negligible values, so that the inclusion of more generations would not have significantly changed the result.

The calculation was performed by evaluating the exact decay probability (see Section 1.2.2) of generated pion and kaons for each of the three effective target-calorimeter densities. These exact decay probabilities were accumulated in bins of momentum for the decay muon. Muons were not traced through the detector, but each event was given a weight equal to the probability that a muon of the given momentum (averaged over p_T) would trigger. For each bin, a density extrapolation was performed using the sums of the exact probabilities. The intercepts were divided by the slopes

in each bin in order to normalize to the observed rates. Then these fractions were multiplied by the observed non-prompt rates to arrive at the fake prompt rates. These background rates are shown for both positive and negative muons in Figure 4-9, with other previously discussed backgrounds. This background is very small, amounting to only .8% of the prompt single μ^+ and .4% of the prompt single μ^- rates (after the subtraction for highly asymmetric dimuons).

4.2.6.3 Hyperon Semi-leptonic Decays

A Monte Carlo calculation was performed to determine whether the semi-leptonic decays of hyperons to muon final states contributed to a false prompt signal, due to their relatively short lifetimes. The calculation included all hyperons (see Table 1-2), using as far as possible measured cross sections, production distributions and branching ratios. Cross sections which have not been measured at high energy were extrapolated from low energy measurements. The result was that fake prompt signals of at most $.01 \times 10^{-6}$ (per interacting proton) for either positive or negative muons can be attributed to hyperons. Since this amounts to less than .2% of the background subtracted prompt single muon rates, it can be ignored.

4.2.7 "Physics" Backgrounds

Once the prompt single muon rates have been measured, and all backgrounds removed, there is still an important question that must be addressed before they are used to study charm production. Namely, are there sources of prompt single muons other than charm?

Since these muons are "single," they must have originated in weak decays (electromagnetic decays lead only to pairs and strong decays do not lead to muons). Since they are prompt, the lifetimes of the parent particles must be very short (less than about 10^{-12} seconds). Two possible sources, besides charm, do exist: bottom particles and τ leptons.

Several experiments have indicated that hadronic bottom particle cross sections with both protons[22] and pions[23] at energies similar to this experiment are exceedingly small (no more than a few nanobarns per nucleon). In fact, a separate study from this experiment[24] has also set upper limits on hadronic bottom production. Taking the maximum cross section allowed of about 50 nanobarns/nucleon, a 15% semi-leptonic branching ratio[25], and an acceptance for bottom which is similar to that for charm, it follows that no more than about .5% of the prompt single muons observed (with a proton beam) could have resulted from bottom production (the limits on

bottom production with pions are event more stringent). Therefore, this source is negligible.

Hadronic production of τ leptons has also not been observed. An estimate of the hadronic $\tau^+\tau^-$ cross section can be obtained by integrating the dimuon cross section above a mass of twice the τ lepton mass. The integration of a simple fit to data from Reference 26 yields a cross section of .2 nanobarns/nucleon for 350 GeV protons to produce $\tau^+\tau^-$ pairs with Feynmann x greater than zero (this calculation uses the well-established scaling of dimuons in m^2/s). The branching ratio of τ leptons to muons is about 18.5%, so the branching ratio times cross section equals .04 nanobarns/nucleon. This corresponds to a rate of only .006 per 10^6 interacting protons, assuming that all muons from τ decays trigger. Thus it is clear that hadronic τ production is totally negligible as a source of prompt single muons.

4.3 Prompt Single Muon Rates

Final prompt single muon rates are calculated by subtracting the backgrounds previously discussed from the raw prompt single muon rates obtained from the density extrapolations. Only the background from the highly asymmetric dimuons is significant compared to the statistical errors on the prompt rates. The final prompt single muon rates are given in Table 4-5 versus momentum. They are plotted versus momentum in Figures 4-10 and 4-11 versus transverse momentum in Figures 4-12 and 4-13.

The prompt single μ^+ rate is $(5.90 \pm .91) \times 10^{-6}$ and the prompt single μ^- rate is $(6.36 \pm .73) \times 10^{-6}$ (per interacting proton). These rates, recall, are not corrected in any way for trigger acceptance. The drop in the rates near p = 20 GeV/c is due purely to the cutoff in the acceptance of the high-p trigger (and the software geometrical cut). The ratio of these rates is consistent with unity, even when the small difference in the μ^+ and μ^- acceptances is taken into account.

The interpretation of these data, calculations of cross sections, and comparisons to charm production models will be discussed in Chapter 6.

The non-prompt single muon rates are shown versus momentum in Figures 4-10 and 4-11 and versus transverse momentum in Figures 4-12 and 4-13. They are also given

versus momentum (for both signs) in Table 4-6. These rates were determined from the slopes of the density extrapolations which were performed in bins versus momentum and transverse momentum. Small corrections have been applied for downstream decays, the effects of the granularity of the target-calorimeter, and the finite lifetimes of pions and kaons. These corrections amounted only to adding the background rates which had been subtracted from the prompt single rates to the "raw" non-prompt rates.

The dimuon rates are shown along with the single muon rates in Figures 4-10 through 4-13. The rates are given versus the momentum of the triggering muon in Table 4-7. These rates were determined by adding the rates for highly asymmetric dimuons (which were subtracted from the raw prompt single muon rates) to the observed dimuon rates.

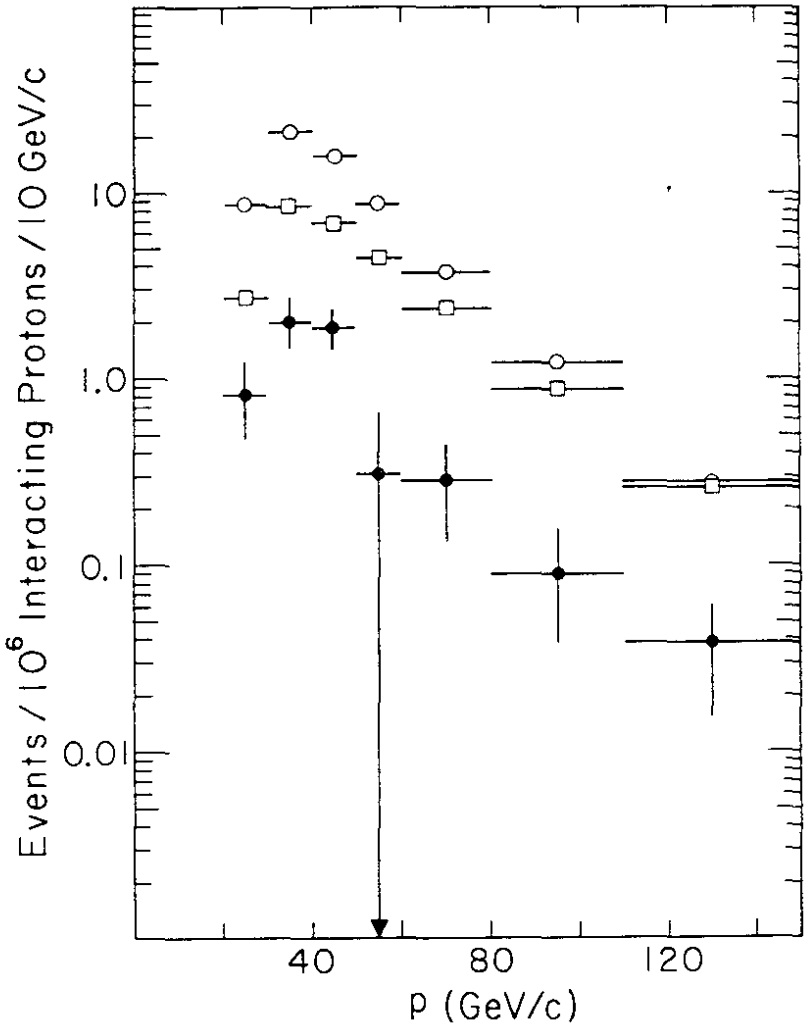

Figure 4-10: Final rates versus momentum for positively charged prompt single muons (dark circles) and non-prompt muons (open circles), and dimuons (open squares) for which the positive muon triggered.

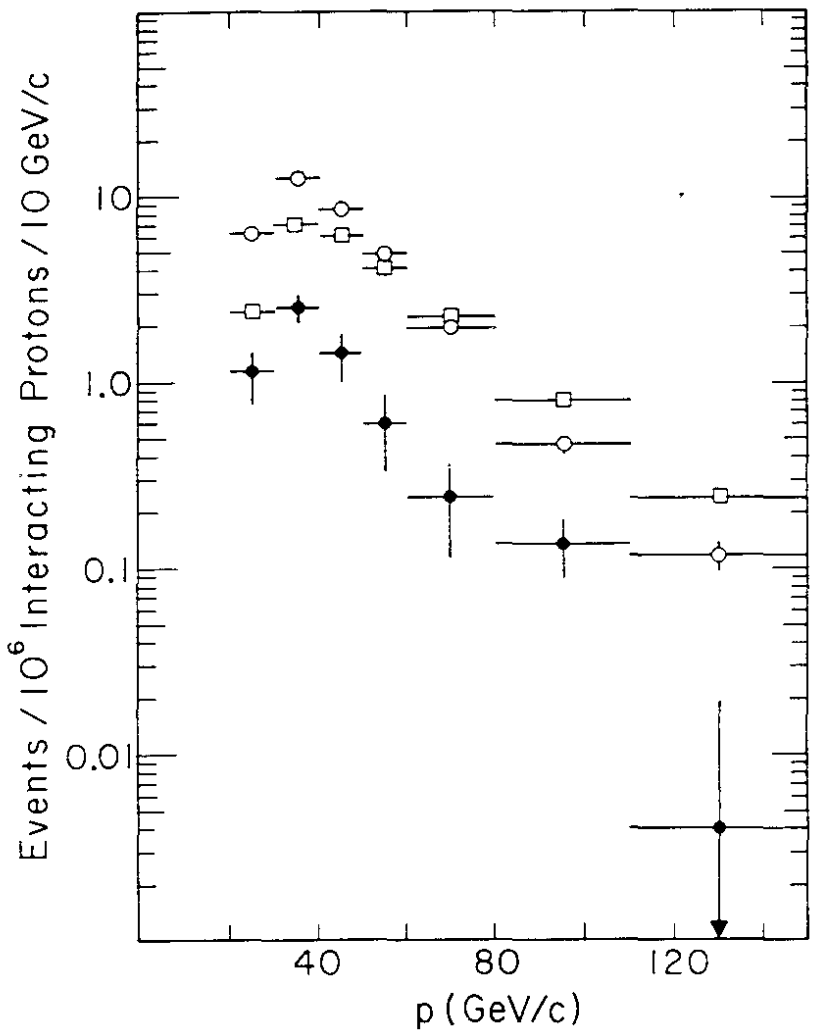

Figure 4-11: Final rates versus momentum for negatively charged prompt single muons (dark circles) and non-prompt muons (open circles), and dimuons (open squares) for which the negative muon triggered.

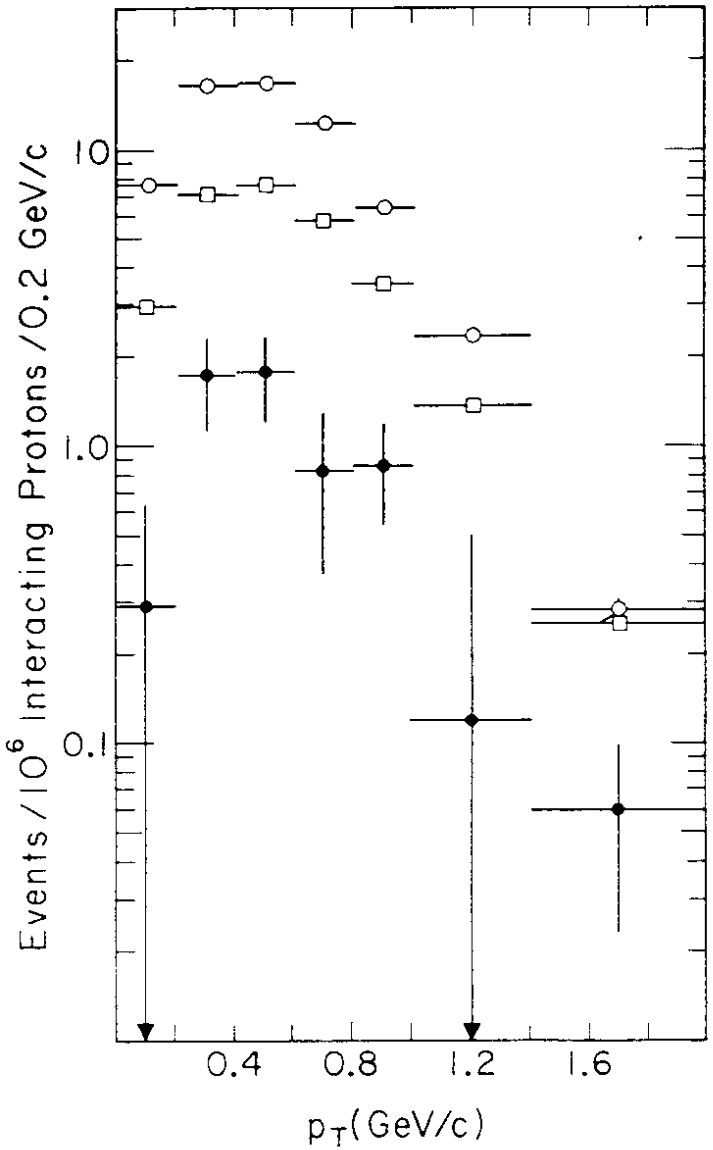

Figure 4-12: Final rates versus p_T for positively charged prompt single muons (dark circles) and non-prompt muons (open circles), and dimuons (open squares) for which the positive muon triggered.

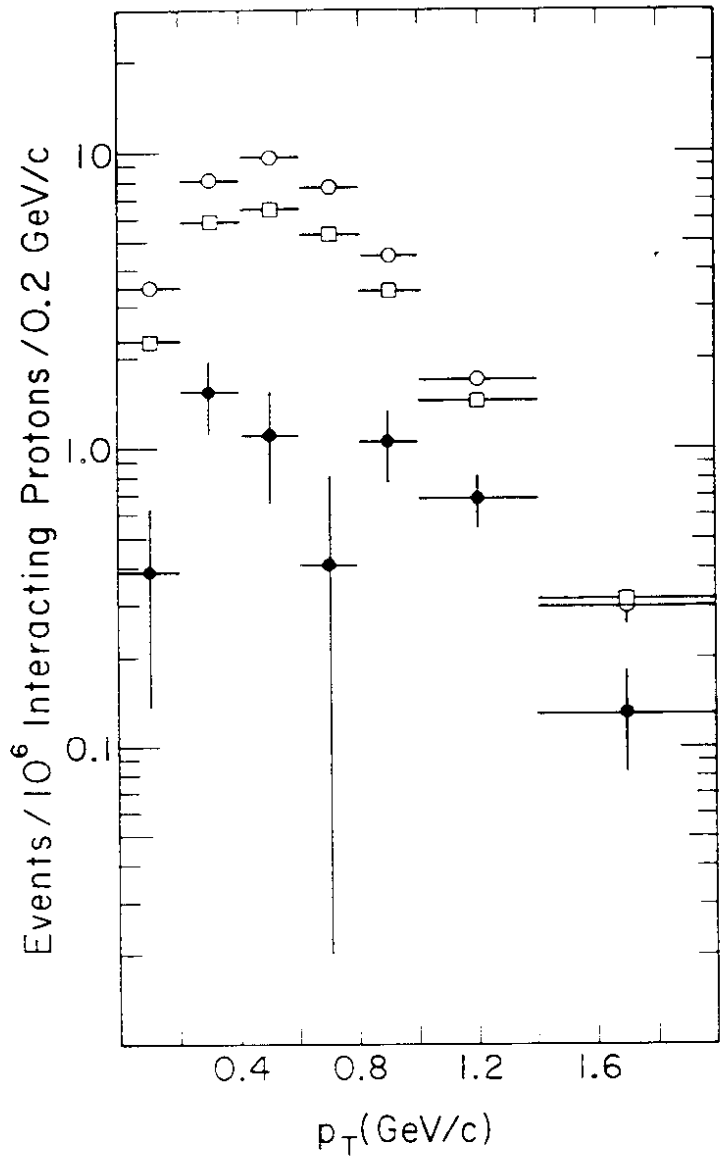

Figure 4-13: Final rates versus p_T for negatively charged prompt single muons (dark circles) and non-prompt muons (open circles), and dimuons (open squares) for which the negative muon triggered.

Table 4-5: Prompt single muon rates (per interacting proton) versus momentum after all background subtractions.

Momentum (GeV/c)	μ^+ ($\times 10^{-6}$)	μ^- ($\times 10^{-6}$)
20- 30	.81 ± .34	1.07 ± .29
30- 40	1.98 ± .53	2.48 ± .43
40- 50	1.82 ± .44	1.35 ± .35
50- 60	.31 ± .33	.58 ± .26
60- 80	.56 ± .31	.47 ± .24
80-110	.27 ± .16	.39 ± .12
110-150	.15 ± .09	.015 ± .061

Table 4-6: Final non-prompt (single) muon rates (per interacting proton) versus momentum for both signs.

Momentum (GeV/c)	μ^+ ($\times 10^{-6}$)	μ^- ($\times 10^{-6}$)
20- 30	8.77 ± .24	6.18 ± .20
30- 40	20.98 ± .37	12.37 ± .30
40- 50	14.48 ± .31	8.50 ± .24
50- 60	8.57 ± .23	4.84 ± .18
60- 80	7.44 ± .22	3.95 ± .16
80-110	3.52 ± .13	1.39 ± .09
110-150	1.11 ± .07	.43 ± .05

Table 4-7: Final dimuon rates (per interacting proton) versus the momentum of the triggering muon. Recall that some dimuon events have both a triggering μ^+ and μ^-.

Momentum (GeV/c)	μ^+ trigger ($\times 10^{-6}$)	μ^- trigger ($\times 10^{-6}$)
20- 30	2.66 ± .11	2.25 ± .08
30- 40	8.24 ± .15	7.02 ± .13
40- 50	6.93 ± .13	6.08 ± .12
50- 60	4.35 ± .09	4.10 ± .09
60- 80	4.61 ± .09	4.32 ± .09
80-110	2.60 ± .06	2.36 ± .06
110-150	1.06 ± .04	.91 ± .03

CHAPTER 5

ANALYSIS OF PION HIGH P DATA

The analysis of the 278 GeV negative pion high-p data leading ultimately to prompt single muon rates versus momentum p and transverse momentum p_T will be described in this chapter. The analysis procedures follow closely those employed in the analysis of the high-p proton data which were described in Chapter 4. In this chapter emphasis will therefore be placed on the aspects of the pion data analysis which differ from the proton data analysis. These differences largely amount to having to cope with two additional background sources, one of which proved to be important.

The calculation of raw prompt single muon rates will be described in Section 5.1. The backgrounds will be addressed in Section 5.2, and the final prompt single muon rates will be presented in Section 5.3.

5.1 Data Analysis

Data were taken in the same five configurations of the target calorimeter and in the same two modes of running (high intensity and low intensity) during the pion running as during the proton running. Table 5-1 shows the number of high-p triggers recorded, the number of interacting beam triggers recorded, and the number of livetime IBV's on target (from scalers) for each configuration and mode. However, in the pion data analysis a distinction must be made between two sets of data which were taken under different trigger conditions. These conditions will be described in Section 5.2.1 when the potential background from accidentals is discussed. For purposes other than the study of accidentals triggers, the distinction is not relevant, and the two data sets will be combined, as has been done in Table 5-1.

Table 5-1: Shown are the numbers of high-p triggers and interacting beam triggers recorded, and the number of livetime IBV's on target for the pion data, for each configuration of the target-calorimeter for both high and low intensity running.

High Intensity			
Configuration	High-p trig	Int. Beam trig	IBV (live) ($\times 10^8$)
COMPACTED	253297	53440	7.7483
SEMI-EXPANDED	184568	61864	5.0679
EXPANDED	259641	69215	5.7502
SPECIAL 1	300389	77007	9.6094
SPECIAL 2	111949	37030	3.7074

Low Intensity			
Configuration	High-p trig	Int. Beam trig	IBV (live) ($\times 10^8$)
COMPACTED	36690	61617	1.2619
SEMI-EXPANDED	20962	29666	.6076
EXPANDED	34872	73526	.8346
SPECIAL 1	44166	77513	1.5294
SPECIAL 2	13762	23837	.4882

5.1.1 Event Selection and Classification

The event selection criteria (both IBV and muon cuts) applied to the pion data were exactly the same as those applied to the proton data. They were described in detail in Section 4.1.1 and its subsections. Here the cut placed on the incoming beam particle momentum (±2.5% using the PWC fit) corresponded to a requirement of 278 ± 6.95 GeV/c. The requirement that the visible energy in an event not exceed 1.2 times the nominal beam energy rejected events whose visible energy was greater than 333.6 GeV. Table 5-2 gives the effective fluxes for each target-calorimeter configuration and mode after the application of the IBV cuts.

The event classification criteria (i.e., the criteria used in deciding whether an event belonged to the single muon or dimuon category) applied in the pion data analysis were exactly the same as in the proton data analysis. They were described in detail in Section 4.1.2 and its subsections. Because the event classification criteria were the same, the discussion of misclassification of events in Section 4.2.2 also applies to the pion data.

Table 5-2: Effective fluxes after IBV cuts for each target-calorimeter configuration for both high and low intensity for the pion data.

	livetime IBV's ($\times 10^8$)	
Configuration	High Intensity	Low Intensity
COMPACTED	7.2845 ± .0085	1.2032 ± .0011
SEMI-EXPANDED	4.7376 ± .0054	.5789 ± .0008
EXPANDED	5.4500 ± .0051	.8018 ± .0006
SPECIAL 1	8.9863 ± .0092	1.4663 ± .0011
SPECIAL 2	3.5034 ± .0046	.4699 ± .0006

5.1.2 Rate Calculations

Rates were calculated by the methods described in Section 4.1.3, with one exception. Before calculating the rates for single muon events with a triggering μ^-, it was necessary to remove events in which beamline muons (which were always μ^-'s, of course) lost substantial amounts of energy in the target-calorimeter. No such events contaminated the proton data since the beam was essentially all protons. The negative beam, however, consisted of about 1% muons (see Section 2.1). Most of these muons (harmlessly) deposited a small amount of energy, about 3 to 4 GeV, in the target-calorimeter via the usual dE/dx mechanism, namely, the ionization of the atoms in the medium. However, a very small fraction of the muons, on the order of four in 10^3, deposited enough energy via "catastrophic" energy loss mechanisms (i.e, knock-on electrons, pair production of electrons, bremsstrahlung, and inelastic scattering off nuclei) to satisfy the ESUM greater than 30 GeV requirement in IBV. (This muon "interaction" also had to take place near the front of the target-calorimeter in order to satisfy the E4-11 requirement as well.) Such muons then penetrated the muon identifier and toroid spectrometer and satisfied the downstream (i.e., muon) part of the high-p trigger. These triggers will be referred to as

"interacting muon" triggers.

Two features of interacting muon events are important here. The first is that the μ^- tends to have very high momentum. Since the energy loss distribution falls very rapidly with increasing energy loss, the energy deposited by the muon was usually just above the ESUM threshold. Therefore, the muon momentum distribution for these events was peaked at roughly 240 Gev/c. The number of such events in which the muon had low momentum was rather small. This is fortunate since it is the low momentum region where most of the muons from charmed particle decays reside.

Figure 5-1 shows the raw single muon trigger rates versus momentum for the COMPACTED configuration. The excess μ^- events at high momentum were due to interacting muons. The figure suggests, and the analysis described below confirms, that below about 150 GeV/c the interacting muons comprised a small fraction of the events.

The second important feature of interacting muon events, and a key to their removal, is that the energy deposition in the target-calorimeter for about 90% of such events was purely electromagnetic. Therefore, the showers from these events were different, and in

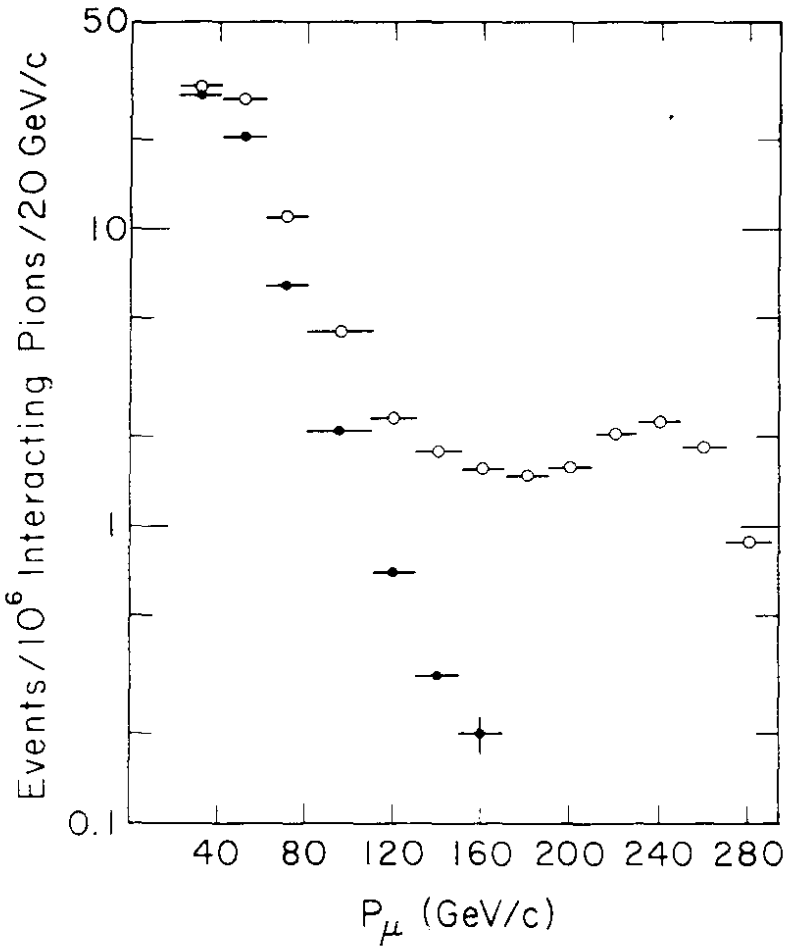

Figure 5-1: Raw single muon trigger rates versus momentum for positive muons (dark circles) and negative muons (open circles) for the COMPACTED configuration.

particular shorter, than the showers induced by hadronic interactions. (The radiation length in iron is 1.76 cm, in contrast to the hadronic absorption length which is an order of magnitude larger.)

A simple algorithm was used event-by-event to determine the length of showers in the target-calorimeter. Beginning at the upstream end of the calorimeter, a search was made for the first two consecutive counters in which significant pulse heights were recorded. The values required were 13 and 28 times minimum ionizing in the first and second counters, respectively. (These pulse heights correspond to about .8 and 1.7 GeV.) The first of these two counters was taken to be at the beginning of the shower. Next, starting from the beginning of the shower, a search was made for the first two consecutive counters in which the pulse heights fell below prescribed values, specifically below 16 and 13 times minimum ionizing. The latter of these two counters was taken to be at the end of the shower. The length of the shower was taken to be the amount of steel between the beginning and end of the shower.

Figure 5-2(a) shows the shower length distribution for all single μ^- events in the COMPACTED configuration. The interacting muon peak, at small shower length, is noticeable to say the least. It must be pointed out,

however, that this plot includes all single μ^- triggers, including those with muons with momentum greater than 150 GeV/c. About 2/3 of the interacting muons are "removed" simply by ignoring events with $p_\mu > 150$ GeV/c. Also, the fraction of events due to interacting muons was largest in the COMPACTED configuration. For EXPANDED the interacting muon rate was about the same, but the single muon rate from hadronic interactions was almost twice as large as for COMPACTED.

Shower length is expected to depend approximately logarithmically on shower energy.[27] Figure 5-2(a) includes events with a wide range of shower energies. Both hadronic and electromagnetic shower energies could vary from the minimum of about 30 GeV, imposed by the energy requirement in IBV, to the maximum of about 258 GeV, imposed by the requirement that the triggering muon have momentum of at least 20 GeV/c. Therefore, a small shower length "correction" was applied which scaled the length of each shower, under the logarithmic hypothesis, to the same energy, chosen to be the beam energy. Specifically, the length of each shower was multiplied by

$$\frac{\ln(E_{BEAM}/a)}{\ln(E_{MEAS}/a)}$$

where E_{MEAS} was the measured shower energy for that event and the parameter a was .5 GeV. Figure 5-2(b) shows the

same events as Figure 5-2(a) with this correction applied.

Figure 5-3(a) shows the corrected shower length distribution for COMPACTED single μ^+ triggers, and Figure 5-3(b) shows it for IBV triggers.

Interacting muon rates were calculated as a function of momentum and transverse momentum, starting from histograms of the corrected shower length distributions for each momentum and transverse momentum bin. These shower length distributions were fit to the sum of two functions which were known to separately fit the interacting muon and hadronic shower length shapes. This was possible because the two types of showers could be isolated for study. Hadronic showers were investigated with events in which a single μ^+ triggered. Electromagnetic showers were studied using a sample of interacting muon events which were isolated by a method which will be described in Appendix 4. It was found that both types of shower length distributions could be well fit by the sum of two gaussians with the same mean values.

The fitting method is illustrated in Figure 5-4. The fit proceeded in two steps. In the first step, the entire hadronic shower length distributions (from 0 to 186 cm) was fit. This established the initial

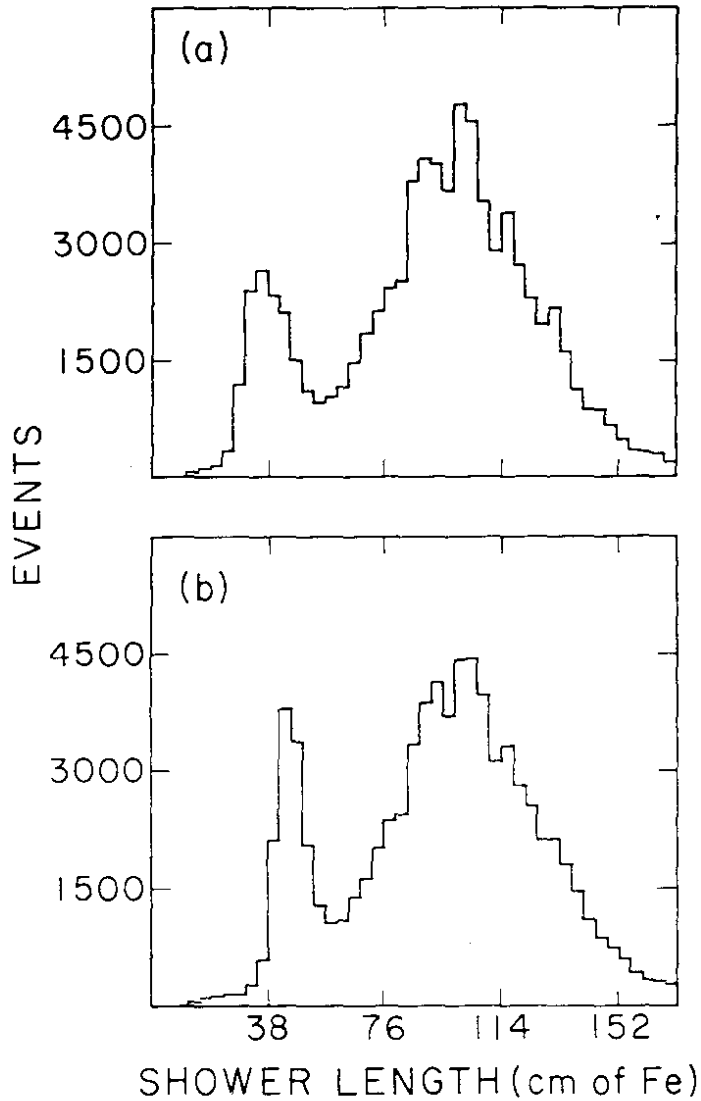

Figure 5-2: (a) Shower length distribution for single μ^- events in the COMPACTED configuration. (b) The same distribution corrected for the energy dependence of the shower length.

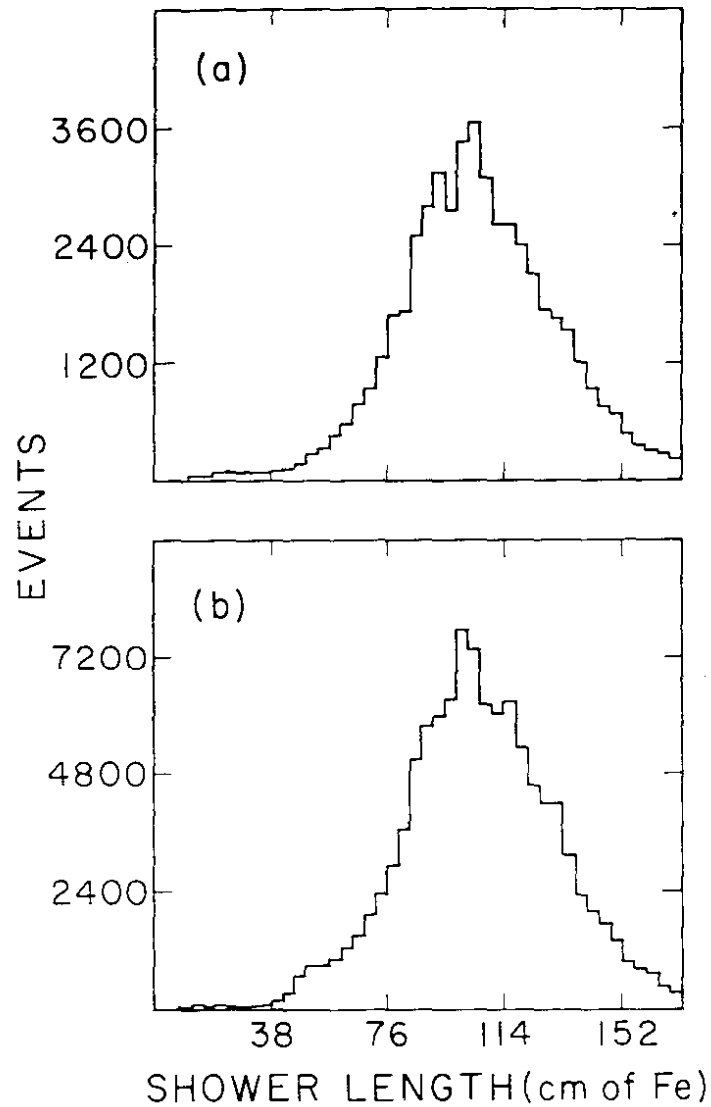

Figure 5-3: Corrected shower length distributions (a) for single μ^+ events and (b) for IBV triggers.

parameters for the second fit, which only covered the hadronic region from 0 to 84 cm. The second fit provided a better estimate of the "background" under the peak, since events far from the region of interest could affect the hadronic shower length curve in the first fit.

Interacting muons will be discussed further in Section 5.2.2 and also in Appendix 4.

The probability P_{12} (see Section 4.1.3) that an extra single muon would accompany an event was determined from IBV trigger events and the small correction for energy dependence in this probability was made bin-by-bin in muon momentum. Table 5-3 gives the values of P_{12} determined from IBV triggers for each of the target-calorimeter configurations and also gives the average values of P_{12}, after the energy dependence correction, separately for events in which positive muons triggered and negative muons triggered.

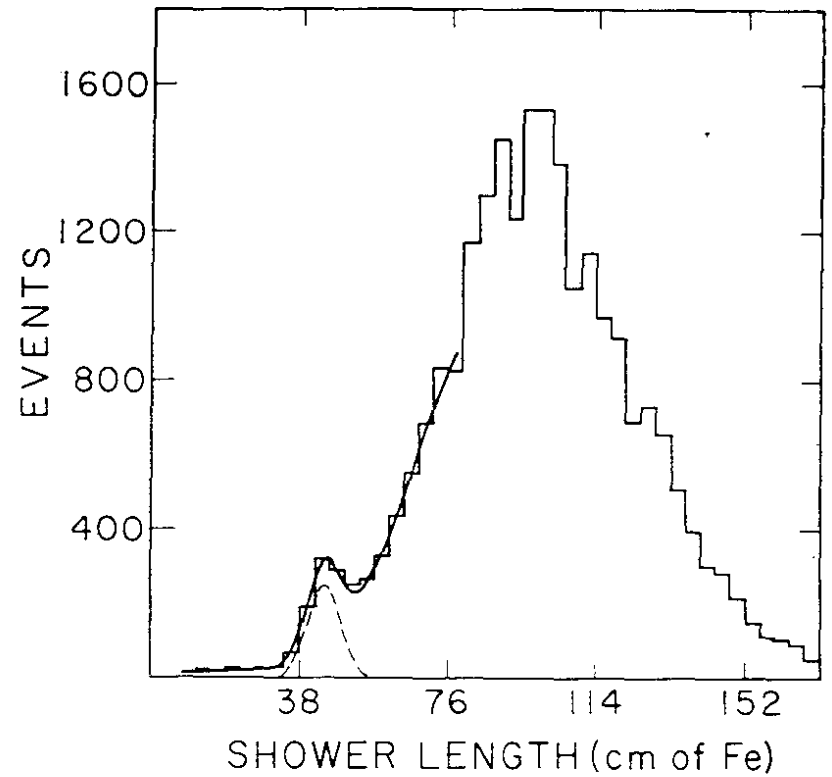

Figure 5-4: Illustration of the fit used to measure interacting muon rates. The histogram is the shower length distribution for COMPACTED single μ^- events with momentum between 20 and 40 GeV/c. The solid curve is the fit including interacting muon and hadronic shower components. The dashed curve shows the interacting muon component only.

Table 5-3: The probability per event P_{12}^{raw} that a muon penetrated into the muon identifier to a depth of 12 counters, corresponding to 5.2 GeV/c in momentum, measured from IBV triggers, is given for each target-calorimeter configuration for the pion data. Also given are the momentum averaged values of P_{12} after the correction for energy dependence has been applied for both μ^+ and μ^- events separately. Of course, interacting muons were subtracted before the momentum averageing for the μ^-'s.

Configuration	P_{12}^{raw} (%)	$P_{12}^{\mu^+}$ (%)	$P_{12}^{\mu^-}$ (%)
COMPACTED	.53 ± .02	.41 ± .02	.40 ± .02
SEMI-EXPANDED	.70 ± .03	.55 ± .02	.54 ± .02
EXPANDED	1.12 ± .03	.88 ± .02	.87 ± .02
SPECIAL 1	.49 ± .02	.39 ± .01	.38 ± .01
SPECIAL 2	.55 ± .03	.43 ± .02	.42 ± .02

5.1.3 Density Extrapolations

Rates were calculated for four classes of events, as in the proton analysis: (1) single triggering positive muons ($1\mu^+$), (2) single triggering negative muons ($1\mu^-$), (3) dimuons with triggering positive muons $(2\mu)^+$, and (4) dimuons with triggering negative muons $(2\mu)^-$. (The third and fourth classes overlap.) Figure 5-5 shows the rates versus inverse density for these classes. Events with triggering μ^-'s whose momentum exceeded 150 GeV/c were excluded. Here, in contrast to the proton case (see Figure 4-4), it is the slope of the $1\mu^-$ line which is the larger, indicating an excess of produced π^-'s over π^+'s, as expected with incident π^-'s.

The raw prompt single muon rates were 13.08 ± .67 and 18.92 ± .85 per 10^6 interacting pions (IBV's) for single μ^+'s and single μ^-'s, respectively. Note that these rates are significantly different, in contrast to the rates from the proton data where they were approximately the same. Since the dimuon rates for events with triggering μ^+'s and μ^-'s are similar (i.e., they differ only by about 10%), it follows that the subtraction for highly asymmetric dimuons which were classified as single muons will also be similar for the two signs. Therefore, the relative μ^- excess will be increased by the subtraction, suggesting a large sign asymmetry in the

production of prompt single muons by pions. The dependence of this excess on momentum will be investigated in Section 5.3. The interpretation of this result will be addressed in Chapter 6.

Here, as in the proton analysis (see Section 4.1.4), data from the SPECIAL 1 and SPECIAL 2 configurations were combined with COMPACTED data for events with p > 80 GeV/c. Figure 5-6 shows the raw prompt single muon rates versus momentum. Final rates, including non-prompt rates, will be given in Section 5.3.

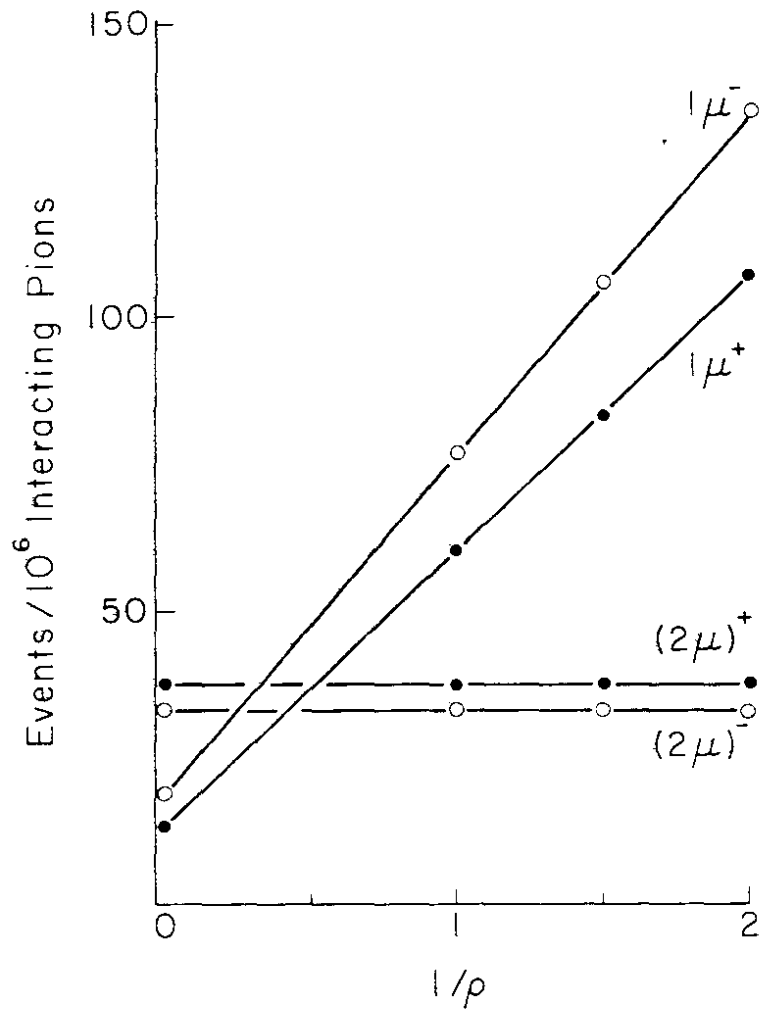

Figure 5-5: Rates for positive muons (solid points) and negative muons (open circles) for four categories of events (defined in the text) versus inverse density for the pion data. The μ^- rates are for p < 150 GeV/c.

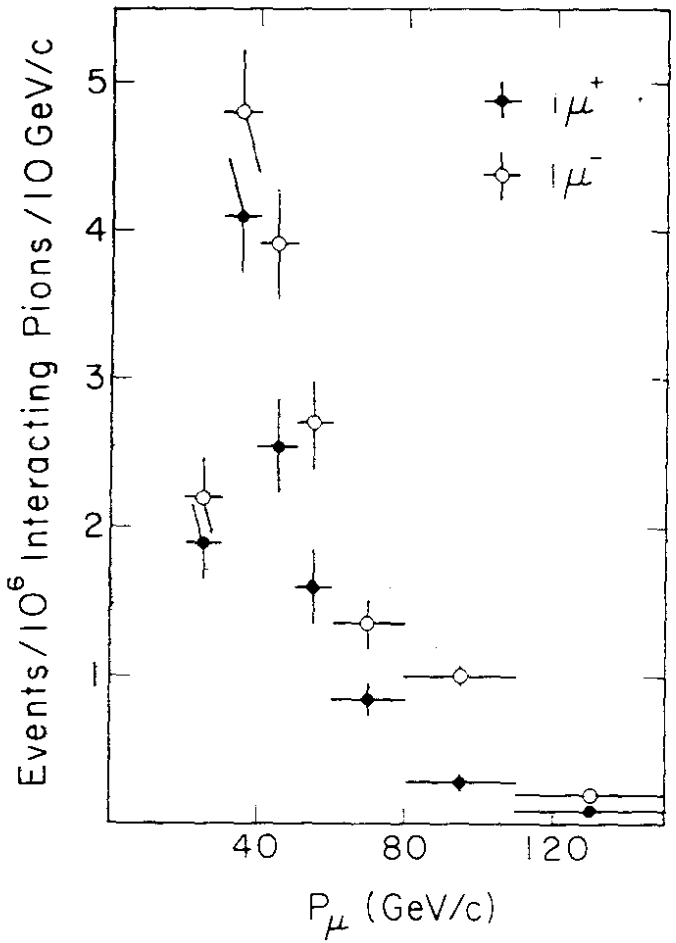

Figure 5-6: Raw prompt single muon rates (no backgrounds subtracted) versus momentum, for the high-p pion data.

5.2 Backgrounds

The backgrounds to the prompt single muon measurements will be discussed below. Most of the backgrounds were discussed in Chapter 4 for the proton data analysis, so the previous chapter can be referred to for details. However, accidentals will be treated more completely here because they constituted a larger fraction of the pion induced triggers. Also, interacting muons, which were introduced in Section 5.1.2, will be considered, along with certain semi-leptonic decays of pions and kaons in flight just upstream of the target-calorimeter.

5.2.1 Accidentals

Accidentals were events in which muons from sources upstream of the detector coincided closely enough in time with legitimate IBV's to trigger. In view of the rather low beam intensities at which this experiment was run (even "high intensity" amounted to at most 200,000 particles per 1.5 second spill), it is perhaps surprising that accidentals should be a problem at all. The explanation derives from the nature of the muon identifier and toroid spectrometer. These devices were

built for neutrino detection, an inherently low-rate application. The large sizes of the scintillation counters and the way the supporting electronics and logic were set up did not allow "tight timing."

The event selection criteria were discussed in Section 4.1.1. One of the main reasons for these cuts was to eliminate accidentals. In this section, the motivation for some of these cuts will be given and their effectiveness assessed.

Accidentals can be divided into two classes: (1) those in which the muon was in the beam and (2) those in which the muon was outside the beam. A practical definition of "in the beam" is that such muons passed through the hole in HALO. The two different types of accidentals triggers will be addressed separately, since different cuts removed them. However, one property common to all accidentals was that the total energy in the event (shower plus muon) exceeded the beam energy by a significant amount. For accidentals, the shower energy was (up to the energy resolution of the calorimeter) the energy of the beam hadron; also the muon had to have sufficient momentum to penetrate the muon identifier and toroid spectrometer (around 20 GeV/c). Because of this, a cut on the total energy in the event could remove all types of accidentals.

(1) Events with the triggering muon in the beam were

vetoed in hardware unless the muon was in the same RF bucket as the IBV hadron. This veto, as will be described below, was not always 100% efficient. The requirement placed on the "in-time" bit (see Section 2.2.2 and Section 4.1.1.2), however, eliminated events in which the muon was more than 5 nanoseconds out of time with the IBV. The only surviving accidentals with the muon in the beam, therefore, had the muon within only a few nanoseconds of the IBV. Such events could be rejected with the requirement of no extra PWC track segments. (Since the hadron and muon were almost exactly in time, the PWC efficiency was not degraded by the gate being out of time with the signal from either particle.)

(2) Events with the triggering muon outside the beam were vetoed if the muon passed through HALO within a wide time window around the hadron. This veto was very efficient and was backed up in software with a pulse height cut (which rejected events with greater than .1 times minimum ionizing). Events with muons outside HALO were removed with the D_{min} cut (see Section 4.1.1.2 for a definition of D_{min}). Figure 5.7 shows the D_{min} distribution for the high-p triggers from a typical run. About 5% of the events were rejected by the cut which eliminated events with $D_{min} > 35$ cm.

Together these cuts (single PWC track, in-time bit,

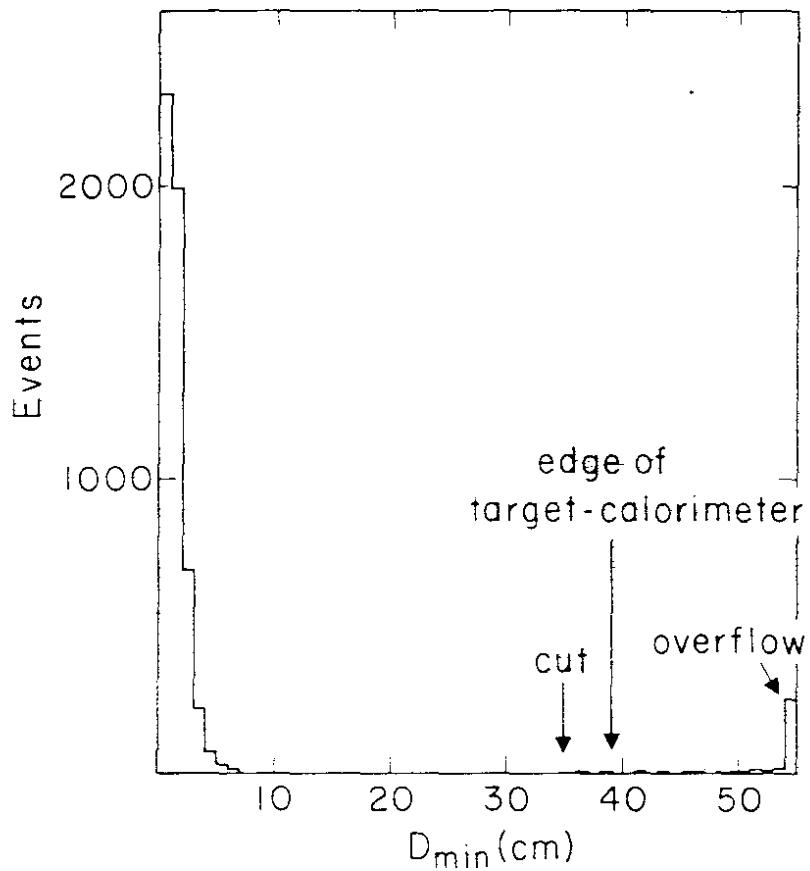

Figure 5-7: The D_{min} distribution for high-p triggers for a typical high-intensity pion run.

D_{min}, etc.) should remove all accidentals. The total energy cut should also remove all accidentals. Therefore, accidentals were rejected "twice," so that the number of accidentals not rejected at least once should be quite small indeed.

As explained in Section 4.2.1, the trigger rate from accidentals should be a strong (at least linear and probably quadratic) function of beam intensity. This dependence is clearly seen in the pion high-p rates before the application of the cuts discussed above. No such dependence remained after the cuts, as will be shown below. But before making this comparison, it is necessary to discuss the pion data sample.

At the beginning of the pion data-taking, a period of about ten days was devoted to tuning up for the pion running. During this period, changes were made which reduced the accidentals trigger rate. The veto counters, described in Section 2.3.1, were installed. It was found that the "early-late" veto in the beam logic (see Section 2.3.1) was not completely efficient for nearby RF buckets, and this problem was fixed. Also, the widths of certain logic signals from the muon identifer and toroid spectrometer (e.g., ZA) were narrowed. Taken together, these changes reduced the accidentals from almost 25% of high-intensity high-p triggers to around 8%. During this "tune-up" period, data were taken. The effect of the

cuts on these data is a very strong indicator of the success of the cuts.

Table 5-4 gives the fraction of high-p $1\mu^-$ triggers rejected by the accidentals cuts for the normal data and the tune-up data, for high and low intensity running for each target-calorimeter configuration. For the normal data, this fraction clearly depended on intensity. Also, the fraction was substantially larger for the tune-up data than the normal data. Nonetheless, the rates after the application of the cuts, given in Table 5-5, show no dependence on beam intensity and are the same for the normal and tune-up data. This indicates that the accidentals have been successfully removed.

An additional check was made by looking at special data. A special run was conducted in which the muon component of the high-p trigger was delayed by 72 nanoseconds. The events which satisfied this mis-timed trigger were all accidentals. Of the 2029 events which passed the geometrical requirements placed on high-p triggers, only 3 survived the other cuts. This also clearly suggests that the accidentals cuts were quite effective. It should be noted, however, that the accidentals which satisfied this mis-timed trigger were not necessarily perfectly representative of those which triggered during normal running (for example, the mix of in-beam versus out-of-beam muons might be different in

this sample).

Finally, as described in Section 4.2.1, other special data indicated that no significant number of good events (i.e., events which were not accidentals) were rejected by the cuts.

Table 5-4: The fraction of events (in percent) rejected as accidentals for each configuration and mode of running for both the tune-up and normal data. The fraction depends on beam intensity as expected, not only between high and low intensity, but also between configurations of the target-calorimeter (the intensity, for a given mode, was about the same for COMPACTED, SPECIAL 1, and SPECIAL 2, but was lower for SEMI-EXPANDED and lower still for EXPANDED). Also, the fraction is significantly higher for the tune-up data taken before all the vetos were in place. No tune-up data were taken in the SEMI-EXPANDED and SPECIAL 2 configurations.

	Tune-Up		Normal	
Config	High (%)	Low (%)	High (%)	Low (%)
C	22.7 ± .2	6.1 ± .2	8.3 ± .1	2.1 ± .1
S	____	____	6.8 ± .1	1.4 ± .1
E	13.6 ± .2	2.8 ± .2	5.1 ± .1	.9 ± .1
SP1	25.6 ± .3	5.7 ± .3	7.8 ± .1	2.2 ± .1
SP2	____	____	8.7 ± .1	1.9 ± .1

Table 5-5: Single μ^- rates (p_μ < 150 GeV/c, interacting muons subtracted) for each configuration of the target-calorimeter and mode of running for both the tune-up and normal data. The fact that these rates are the same for both high and low intensity running and for both the tune-up and normal data is strong evidence that accidentals triggers have been successfully eliminated. All rates are per 10^6 interacting pions.

	Tune-Up		Normal	
	High	Low	High	Low
C	76.5 ± .7	78.6 ± 1.5	76.7 ± .4	78.9 ± 1.0
S	____	____	105.6 ± .5	106.7 ± 1.4
E	135.0 ± 1.1	131.0 ± 2.4	135.4 ± .6	133.2 ± 1.7
SP1	77.0 ± .9	74.1 ± 1.7	75.5 ± .4	75.8 ± .9
SP2	____	____	76.9 ± .5	76.3 ± 1.4

5.2.2 Interacting Muons

Interacting muon events have been discussed previously, in Section 5.1.2, where the procedure which was used to subtract events characterized by purely electromagnetic showers in the target-calorimeter was described. This procedure removed interacting muon events due to bremsstrahlung, direct production of e^+e^- pairs, and knock-on electrons. Muon interactions in which hadrons were produced were not removed by this subtraction. Such events comprised about 10% of all muon interactions and contributed a rate which has been calculated to be .29 ± .04 per 10^6 IBV's for events with $p < 150$ GeV/c. This amounts to about 2% of the prompt single μ^- rate (after the subtraction of highly asymmetric dimuons). The subtraction for these events is made as a function of p and p_T.

Appendix 4 addresses the issue of interacting muons in detail. There it is shown that the shower shape subtraction agrees with what is expected for purely electromagnetic showers. Also, the calculation of the subtraction for events in which muons produced hadrons is discussed.

5.2.3 Semi-leptonic Pion and Kaon Decays in Flight

The decays $\pi^- \to \gamma\mu^-\nu$, $K^- \to \pi^0\mu^-\nu$, and $K^- \to \gamma\mu^-\nu$ (with branching ratios $(1.24 \pm .25) \times 10^{-4}$, $(3.20 \pm .09) \times 10^{-2}$, and $(5.3 \pm 3.5) \times 10^{-3}$, respectively) in the region between the PWC spectrometer magnet and the target-calorimeter (7.7 meters) were a potential source of background. Such events could trigger if the photons deposited sufficient energy in the target-calorimeter and if the muon penetrated to the end of the detector. These events, it should be noted, led to purely electromagnetic showers in the target-calorimeter. Therefore, the shower-length fitting procedure subtracted these events along with interacting muons. Nonetheless, the trigger rate from these decays was calculated.

A Monte Carlo calculation was performed in which these (three-body) decays were simulated. Since the masses and lifetimes of the particles, as well as their momenta and the length of the decay space are known, the sources of error in the calculation are the uncertainties in the branching ratios, the exact value of the ESUM threshold for electromagnetic showers, and the kaon fraction of the beam. Although all three decays were considered, the channel $K^- \to \pi^0\mu^-\nu$ dominates, and its branching ratio is very well known. Also, for this

channel the kinematics of the decay are such that the π° is usually very energetic, so that the rate depends only weakly on the ESUM threshold. The uncertainty in the kaon fraction of the beam, however, contributed an overall normalization error of about 50%.

The calculated total trigger rate for all three decays (for $p < 150$ GeV/c) was $.4 \pm .2$ per 10^6 interacting pions.

5.2.4 Highly Asymmetric Dimuons

As in the proton data, the largest background to the prompt single muon measurement for pions came from highly asymmetric dimuons in which one muon had momentum less than 5.2 GeV/c. Such events were classified as single muons. Since dimuons are prompt, these events were not removed by the density extrapolation technique. This background was subtracted from the raw prompt single muon rates with the aid of a Monte Carlo calculation.

The dimuon Monte Carlo is described and its predictions are compared to dimuon distributions measured in this experiment in Appendix 1. In order to minimize model dependence, the Monte Carlo was used to calculate only the ratio of unobserved dimuons to observed dimuons. These ratios, calculated for each momentum and transverse

momentum bin, were multiplied by the observed dimuon rates to arrive at the "fake" single muon rates. The observed dimuon rates, the raw (i.e., uncorrected) prompt single muon rates, and the calculated fake single muon rates are shown in Figure 5-8 versus momentum and in Figure 5-9 versus transverse momentum.

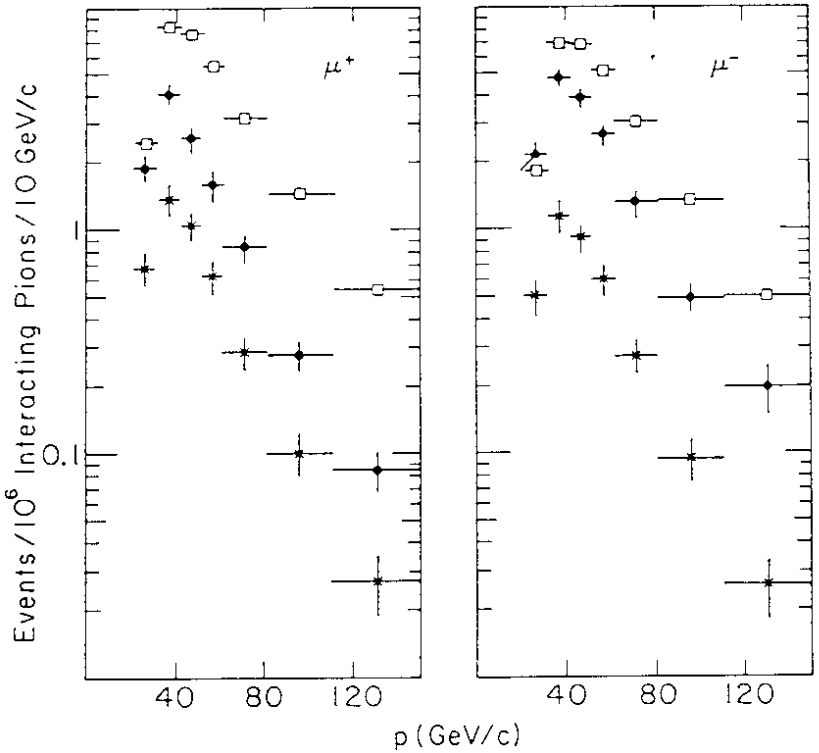

Figure 5-8: Rates for observed dimuons (open squares), raw prompt single muons (dark circles), and the calculated background (crosses) from highly asymmetric dimuons versus momentum for events with triggering μ^+'s and μ^-'s.

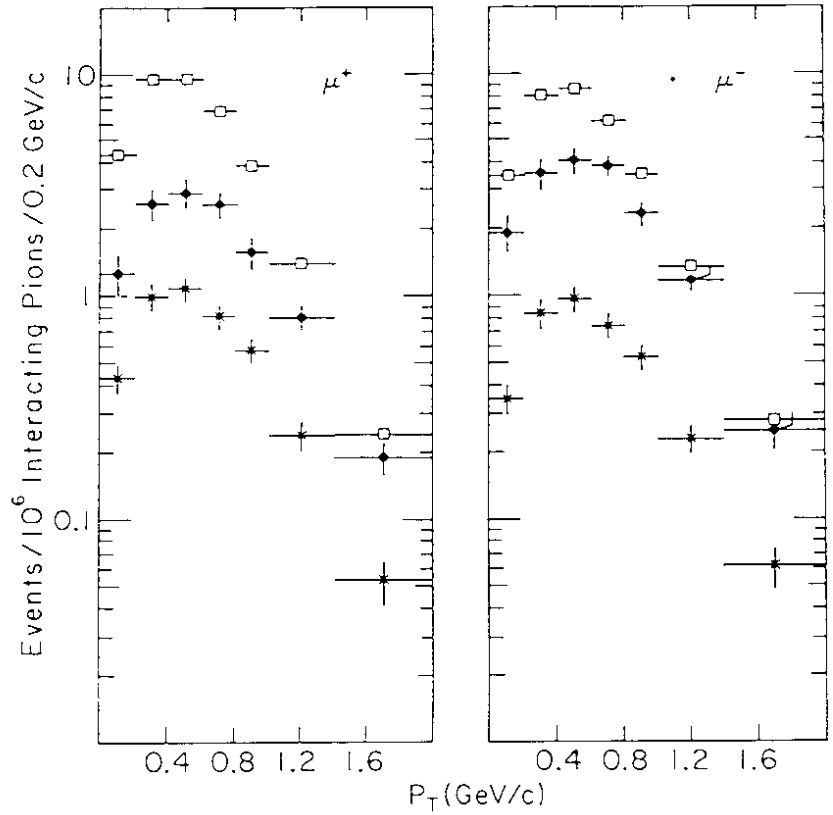

Figure 5-9: Rates for observed dimuons (open squares), raw prompt single muons (dark circles), and the calculated background (crosses) from highly asymmetric dimuons versus p_T for events with triggering μ^+'s and μ^-'s.

5.2.5 Upstream Interactions

The potential background from interactions upstream of the target-calorimeter (in vacuum windows, PWC's, etc.) was discussed in Section 4.2.4. The method used to study this background was described there (i.e., increasing the background by a factor of 10 by increasing the material). During the pion running, special extra material runs were conducted in both the COMPACTED and SPECIAL 1 configurations of the target-calorimeter. The difference between the single muon rates (both signs summed) for the runs with extra material and the normal data was -1.07 ± 1.53 (per 10^6 interacting pions) for COMPACTED and $.31 \pm 1.93$ for SPECIAL 1. Combining these and dividing by ten yields a background estimate of $-.05 \pm .12$ (per 10^6 interacting pions). As in the proton data, there is no indication that upstream interactions constituted a background.

5.2.6 Downstream Decays

The nature of the background due to downstream decays was described in Section 4.2.5. It was calculated via Monte Carlo, as described in Appendix 2. The background rate was found to be small, only .19% of the non-prompt

rate for μ^+'s and .25% of the non-prompt rate for μ^-'s, which amounts to .09 and .14 events per 10^6 pion interactions for μ^+'s and μ^-'s, respectively. Therefore, downstream decays amounted to 1.2% of the prompt single μ^+ rate and 1.0% of the prompt single μ^- rate after the subtraction for highly asymmetric dimuons (a systematic error of 100% was been used in subtracting this background).

5.2.7 Systematic Errors in the Density Extrapolation

Three sources of systematic error in the density extrapolation method have been investigated (as in Section 4.2.6): (1) the granularity of the target-calorimeter (i.e., the steel plates followed by air gaps; see Section 4.2.6.1), (2) the finite lifetimes of pions and kaons (see Section 4.2.6.2), and (3) the semi-leptonic decays of hyperons (see Section 4.2.6.3). The calculation of each of these was described in the previous chapter in the listed sections.

The false prompt single muon rates from the granularity of the target-calorimeter was found to be .3% of the non-prompt rates, or .14 and .18 events per 10^6 interacting pions for μ^+'s and μ^-'s, respectively. The finite lifetimes of π's and K's contributed a practically

negligible rate of .011 and .014 events per 10^6 interacting pions for μ^+'s and μ^-'s, respectively. The production of hyperons by both pions and kaons (.4 ± .2% of the beam) were included in the calculation. The background from semi-leptonic decays of hyperons was found to be completely negligible (less than .01 events per 10^6 interacting pions to either sign).

Together these small background sources amount to only 1.9% of the prompt single μ^+ signal and 1.3% of the prompt single μ^- signal (after the subtraction for highly asymmetric dimuons). Nonetheless, they will be subtracted from the raw prompt single muon rates versus both p and p_T.

5.2.8 "Physics" Backgrounds

The term "physics backgrounds," as used here (see Section 4.2.7 also), refers to sources of prompt single muons other than charm. Bottom particles and τ leptons are the only known sources which could contribute in this energy regime.

Upper limits on the cross section for bottom particle production by pions have been set by several experiments[23], including this experiment.[24] Taking a upper limit of 10 nanobarns/nucleon, a 15% semi-leptonic

branching ratio[25], and the same acceptance for bottom as for charm, it follows that no more than about .2% of the prompt single μ^+ and .1% of the prompt single μ^- signals could have originated from bottom particles.

The cross section for τ lepton production may be estimated (τ's have not been observed yet in hadronic experiments) by integrating the pion induced dimuon cross section above twice the τ mass (i.e., above threshold). Integrating a simple fit to data from Reference 28 yields a cross section of .30 nanobarns/nucleon for 278 GeV/c pions to produce a $\tau^+\tau^-$ pair with Feynmann x greater than zero. The τ branching ratio to muons is about 18.5%, so the brancing ratio times cross section is only .06 nanobarns/nucleon, which corresponds to a rate of only .006 events per 10^6 pion interactions assuming that all muons from τ decays would trigger. Therefore, it is clear that hadronic τ production is a completely negligible source of prompt single muons.

5.3 Prompt Single Muon Rates

Final prompt single muon rates are obtained by subtracting the backgrounds (discussed above) from the raw prompt single muon rates (from the density extrapolations). These rates are given versus momentum in Table 5-6. They are plotted verus momentum in Figures 5-10 and 5-11 and versus transverse momentum in Figures 5-12 and 5-13.

The prompt single μ^+ rate is $(7.78 \pm .74) \times 10^{-6}$ and the prompt single μ^- rate ($p < 150$ GeV/c) is $(13.85 \pm .87) \times 10^{-6}$ (per interacting pion). These rates are not corrected in any way for trigger acceptance. However, the striking difference in these rates (almost a factor of two) is not due to acceptance. Recall that in the proton case the rates were approximately equal.

The interpretation of these data, in particular the difference of the μ^- and μ^+ rates, calculations of charm cross sections and comparisons to charm production models will be discussed in Chapter 6.

The non-prompt single muon rates are shown in Figure 5-10 and 5-11 versus momentum and are tabulated in Table 5-7. They are shown versus p_T in Figures 5-12 and 5-13. The rates were determined from the slopes from the density extrapolations which were performed in bins versus momentum. Small corrections have been made for

downstream decays, the effect of the granularity of the target-calorimeter, the finite lifetimes of pions and kaons, and the mistaken identification of hadronic events as muon interactions (see Appendix 4).

The dimuon rates are given versus the momentum of the triggering muon in Table 5-8 (also see Figures 5-10 through 5-13). These rates were determined by adding the rates for highly asymmetric dimuons (which were subtracted from the raw prompt single muon rates) to the observed dimuon rates.

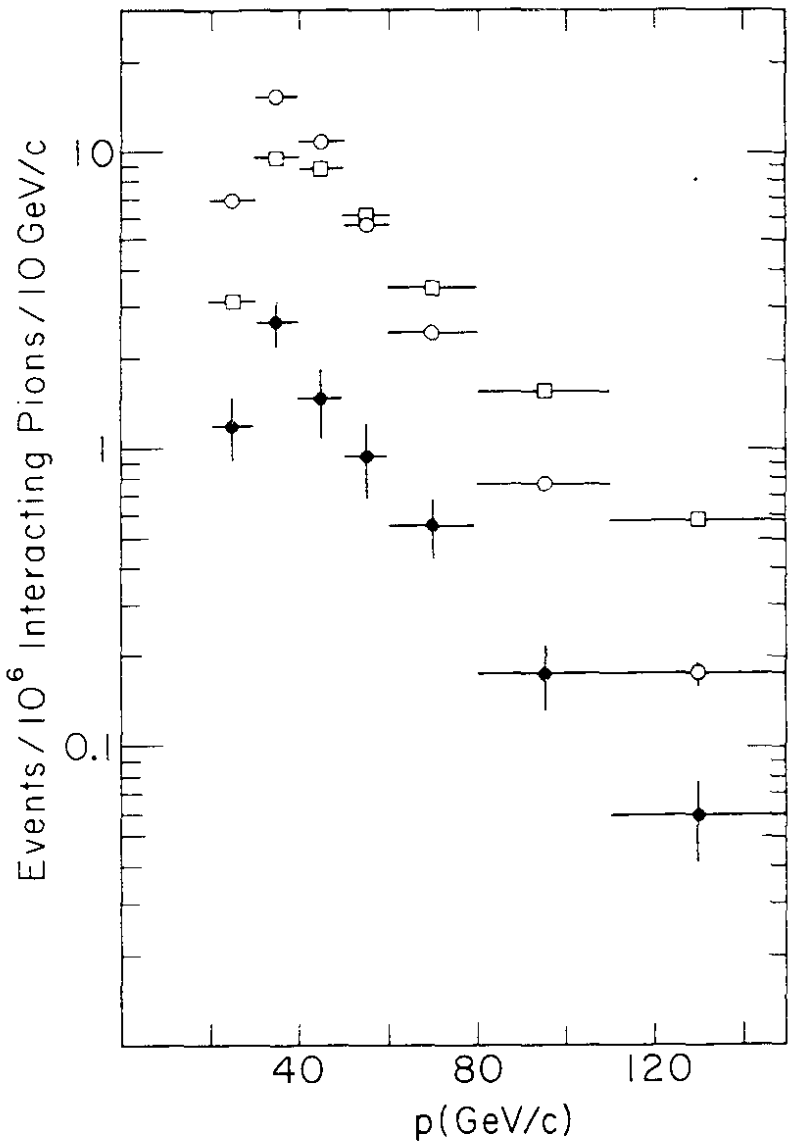

Figure 5-10: Final rates versus momentum for positively charged prompt single muons (dark circles) and non-prompt muons (open circles), and dimuons (open squares) for which the positive muon triggered (for the pion data).

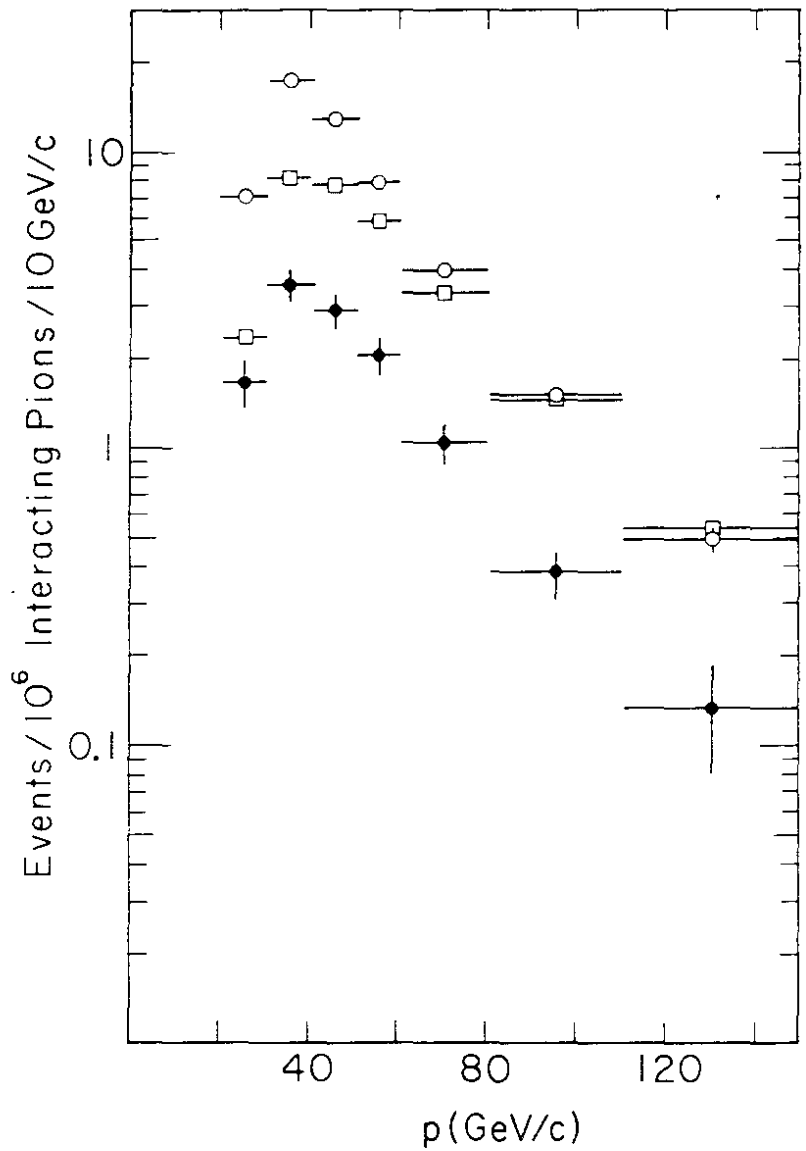

Figure 5-11: Final rates versus momentum for negatively charged prompt single muons (dark circles) and non-prompt single muons (open circles), and dimuons (open squares) for which the negative muon triggered (for the pion data).

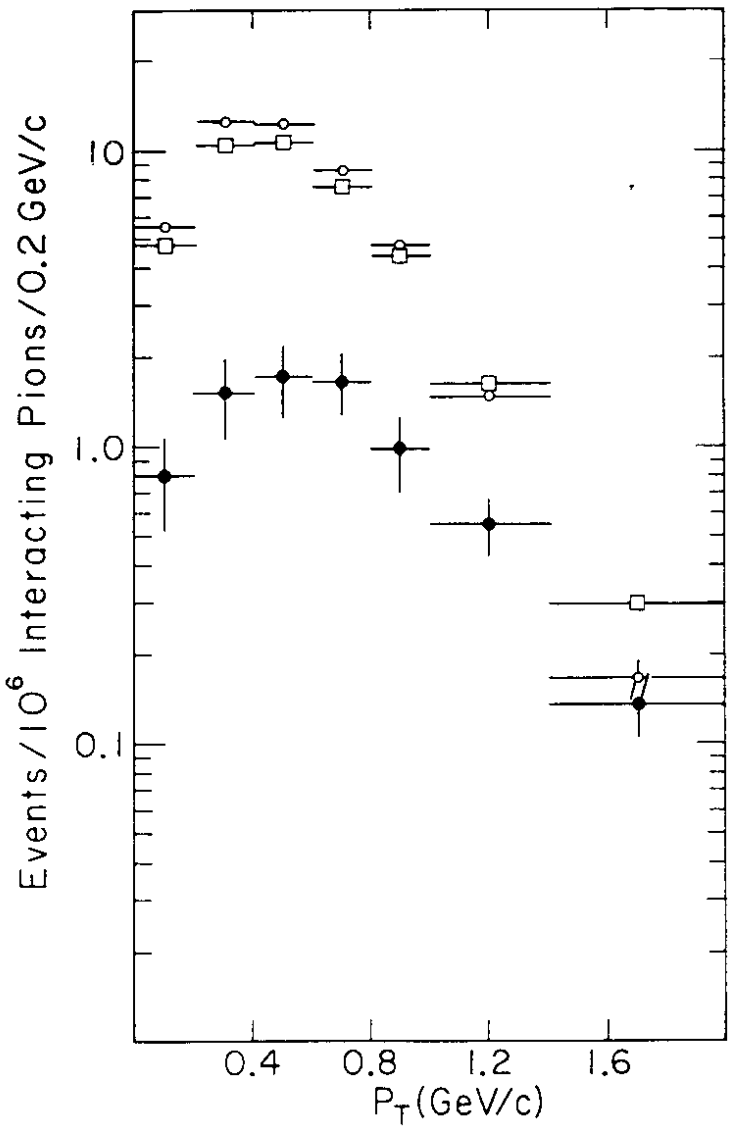

Figure 5-12: Final rates versus p_T for positively charged prompt single muons (dark circles) and non-prompt muons (open circles), and dimuons (open squares) for which the positive muon triggered (for the pion data).

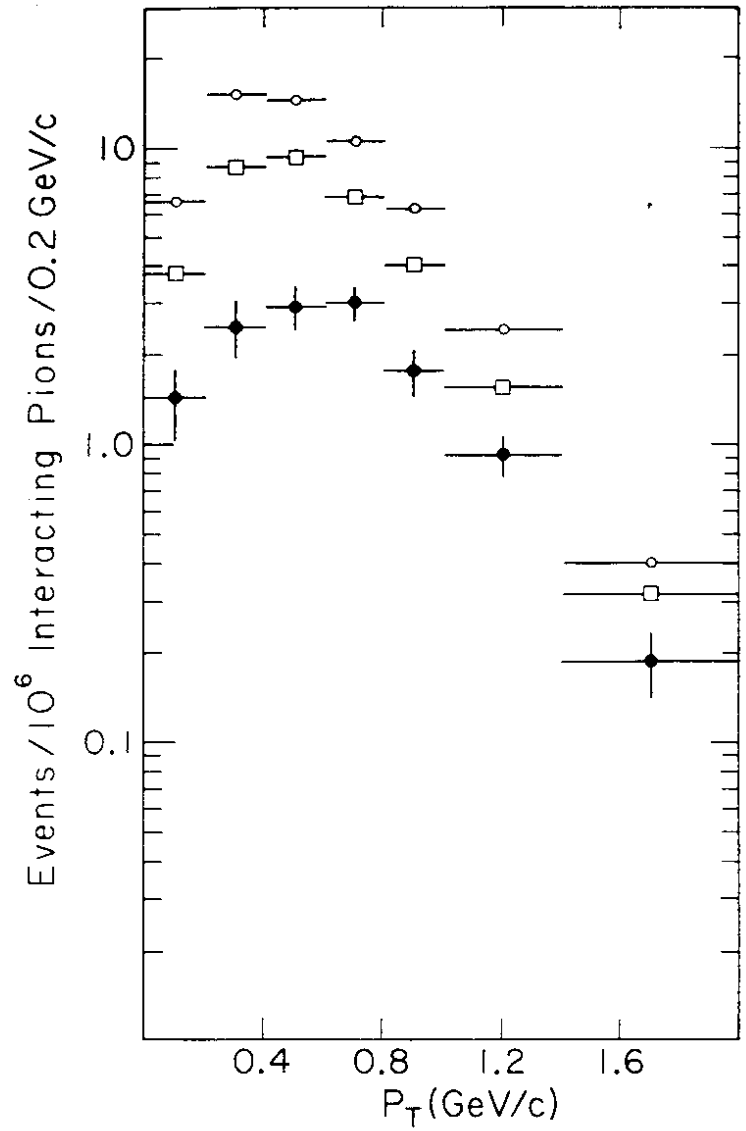

Figure 5-13: Final rates versus p_T for negatively charged prompt single muons (dark circles) and non-prompt muons (open circles), and dimuons (open squares) for which the negative muon triggered (for the pion data).

Table 5-6: Prompt single muon rates (per interacting pion versus momentum after all background subtractions. The fall in rates at low p is due to the acceptance of the high-p trigger and the analysis cuts.

Momentum (GeV/c)	μ^+ ($\times 10^{-6}$)	μ^- ($\times 10^{-6}$)
20- 30	1.18 ± .28	1.64 ± .28
30- 40	2.64 ± .44	3.53 ± .46
40- 50	1.45 ± .36	2.90 ± .40
50- 60	.94 ± .26	2.05 ± .32
60- 80	1.09 ± .24	2.08 ± .33
80-110	.52 ± .13	1.13 ± .21
110-150	.23 ± .07	.53 ± .21

Table 5-7: Final non-prompt (single) muon rates (per interacting pion) versus momentum for both signs.

Momentum (GeV/c)	μ^+ ($\times 10^{-6}$)	μ^- ($\times 10^{-6}$)
20- 30	6.94 ± .18	7.15 ± .19
30- 40	15.54 ± .28	17.37 ± .32
40- 50	10.87 ± .23	13.00 ± .28
50- 60	5.76 ± .17	7.84 ± .24
60- 80	4.89 ± .24	7.98 ± .24
80-110	2.26 ± .09	4.54 ± .18
110-150	.69 ± .05	1.97 ± .15

Table 5-8: Final dimuon rates (per interacting pion) versus the momentum of the triggering muon. Recall that some dimuon events have both a triggering μ^+ and μ^-.

Momentum (GeV/c)	μ^+ trigger ($\times 10^{-6}$)	μ^- trigger ($\times 10^{-6}$)
20- 30	3.11 ± .12	2.34 ± .09
30- 40	9.66 ± .22	8.18 ± .18
40- 50	8.74 ± .17	7.77 ± .15
50- 60	6.06 ± .12	5.82 ± .12
60- 80	6.88 ± .11	6.69 ± .11
80-110	4.63 ± .08	4.41 ± .08
110-150	2.27 ± .05	2.14 ± .04

CHAPTER 6

RESULTS ON CHARM PRODUCTION

The preceding two chapters have described the methods by which the prompt single muon rates were measured as functions of p and p_T. In this chapter, these rates will be discussed in the context of hadronic charm production. Such conclusions as can be drawn from these data will be presented. The various theoretical models of hadronic charm production will be discussed to see what impact on theory these data have. The results of other charm experiments will be considered and compared, where possible, to this experiment.

6.1 Theoretical Considerations

No generally accepted theoretical picture of hadronic

charm production exists at the present time, primarily because the experimental situation is so confusing. Several experiments conducted at the ISR (a proton-proton collider at CERN) have reported charm cross sections of the order of 1 mb at center of mass energy of 62 GeV, while the majority of lower energy, fixed target experiments ($E_{cm} \sim 25$ GeV) have indicated charm cross sections which are substantially lower (see Section 6.3.2). Such a dramatic variation of cross section with energy was totally unexpected and has presented theorists with a challenging problem. Indeed, this problem may yet prove to be an experimental abberation.

In order to provide a context in which to discuss the results of this experiment, it is necessary to briefly review the basic theoretical ideas in hadronic charm production. For the most part, hadronic charm production is viewed as occurring through one (or a combination) of three mechanisms: (1) the hard scattering of quarks and gluons from the beam and target hadrons such that $q\bar{q} \rightarrow c\bar{c}$ or $gg \rightarrow c\bar{c}$ (these two processes together are sometimes called "flavor creation"), (2) the excitation of charmed quarks from the charmed sea (so-called "flavor excitation"), or (3) the diffractive dissociation of non-charmed hadrons into charmed hadrons (e.g., $\Lambda_c\bar{D}^\circ$) owing to an "intrinsic charm" component in the initial

hadronic bound state wave functions. Each of these three ideas will be discussed below.

(1) Flavor creation. The lowest order ($O(\alpha_s^2)$) QCD diagrams are shown in Figure 6-1(a). The process $gg \rightarrow c\bar{c}$ dominates in nucleon-nucleon interactions, but $q\bar{q} \rightarrow c\bar{c}$ is expected to be important in pion-nucleon interactions, because of the valence antiquark of the pion.

The cross section calculation for these processes is straightforward within a particular set of assumptions.[29] The cross section, however, is very sensitive to the assumed threshold mass, which is believed to be less than the obvious choice, $2m_D$ (twice the mass of the lowest mass charmed particle), because of the effects of interactions between off-shell charmed quarks and the other quarks and gluons present in the interaction. The proper threshold is a matter of theoretical speculation. Typically it is taken to be $2m_c$, twice the mass of the charmed quark, in which case m_c is taken to be something of a parameter. For reasonable assumptions, the charm cross section at center of mass energy of about 25 GeV is around 20 μb (see Reference 30).

The distribution in x_F of the charmed particles is expected to be mainly "central" (i.e., concentrated at small x_F)[31], although it has been argued[32] that via recombination with the valence quarks of the initial hadrons, charmed particles can indeed be produced at

large values of x_F.

(2) Flavor excitation. The lowest order ($O(\alpha_s^2)$) QCD diagrams for the flavor excitation processes $qc \to qc$ and $gc \to gc$ are shown in Figure 6-1(b). Calculations[29] have indicated that charm production via flavor excitation could be as large or larger than by flavor creation. However, two serious uncertainties in the calculations, the charm sea structure functions and the value of a cut-off parameter Q^2_{min} (the miminum momentum transfer at which the charmed sea can contribute), which is analogous to the threshold problem for flavor creation, prevent strong conclusions.

Recently, it has been claimed[33] that flavor excitation leads to a rather hard x_F distribution for the produced charmed quarks, so that the recombination of charmed quarks with beam particle fragments to form charmed baryons (in proton-proton collisions) could take place. Therefore, the flavor excitation mechanism, along with a sufficiently small value of Q^2_{min}, could account for the large ISR Λ_c cross sections.

(3) Intrinsic charm. This model, proposed[34] specifically to explain the ISR results, postulates that about 1% of the time, the proton exists as a $|uudc\bar{c}\rangle$ state, where the c and $\bar{c}$ are intrinsic, as opposed to being produced in any interaction. When such a state is diffractively excited, it decays to charmed hadrons, for

example to $\Lambda_c\bar{D}^\circ$. This model will be addressed rather directly later.

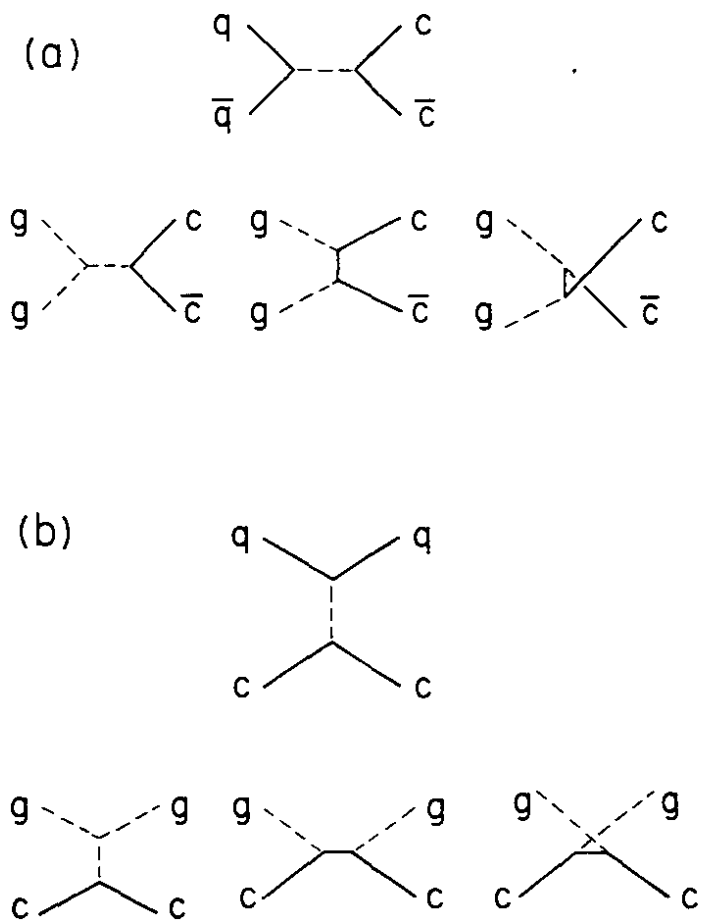

Figure 6-1: Lowest order QCD diagrams for (a) flavor creation and (b) flavor excitation.

6.2 Method of Analysis

The interpretation of prompt single muon measurements in terms of charm production is complicated by the fact that the observed muons were produced when the charmed particles of interest decayed. The momenta and transverse momenta of the parent charmed particles cannot be inferred on an event-by-event basis. Instead, a Monte Carlo procedure is required to convert a hypothetical charm production distribution into a muon distribution which can be compared to the data. By repeated comparisons of different charm production distributions, it is possible to decide which best reproduces the measured muon distributions. In this section the details of how these comparisons have been made are described.

It was assumed, unless specified otherwise, that D mesons (either D^+ or D^0 or their antiparticles D^- and D^0) were produced according to the formula

$$E \frac{d^3\sigma}{dp^3} \sim (1 - x_F)^{\alpha} e^{-\beta p_T},$$

where x_F is the Feynmann x and p_T the transverse momentum of the D. The parameters α and β were varied to determine their best values. Other functional forms for the p_T distributions were also tried, mainly to facilitate comparisons with other experiments.

The semi-leptonic decays of D meson were assumed to proceed 60% of the time through the channel $D \rightarrow K\mu\nu$ and 40% of the time through $D \rightarrow K^*\mu\nu$. This assumption is based on SPEAR data[35] where the electron spectrum from D decays indicates such a mixture. Matrix elements for the decay were taken from Reference 36.

The semi-leptonic decays of the Λ_c have not been studied as extensively as those of the D mesons. Therefore, when simulating the decays of Λ_c, it has been necessary to make an assumption which unfortunately is not experimentally supported. The assumption made here is that the decay proceeds 50% of the time into $\Lambda^\circ\mu\nu$ and 50% of the time into $\Lambda(1520)\mu\nu$. The sensitivity of the results to this assumption can be investigated by changing the assumption. Indeed, studies indicate that the acceptance increases by no more than 20% if 100% $\Lambda^\circ\mu\nu$ is assumed and decreases by no more than 20% if 100% $\Lambda(1520)\mu\nu$ is assumed.

A complication is introduced by the fact that the interaction target, the "beam dump," was thick. It is therefore not guaranteed that the charmed particles produced in such a dump were all produced in the primary interactions. That is, the production of charm by secondaries must also be included in the Monte Carlo generation of charmed particles. This introduces a model dependence because an assumption must be made as to the

variation of the charm cross section with center of mass energy. Also, the production of secondary hadrons must also be simulated in the Monte Carlo.

The energy dependence of the charm cross section used has been taken from the QCD calculation of Reference 37. The energy dependence (in the region of interest, $E_{cm} < 27$ GeV) is given approximately by

$$\sigma_{charm} \sim e^{-41.0/E_{cm}} \quad \text{for protons,}$$

and

$$\sigma_{charm} \sim e^{-33.5/E_{cm}} \quad \text{for pions,}$$

where E_{cm} is the center of mass energy (these are rough fits to published curves). Under these assumptions secondary production amounts to 10% to 20% of all charm, depending on α. For small α (i.e., flat x_F distribution), the secondary production tends toward the upper end of the given range. However, in comparisons with the intrinsic charm model, the energy dependence implied by this model[34] has been used.

Muons, once generated, were traced through the apparatus. The effects of dE/dx (including bremsstrahlung, pair production, and knock-on electrons) and multiple Coulomb scattering were included. Monte Carlo "data tapes" were written which contained raw data

in the form of spark chamber hits, etc. These Monte Carlo data tapes were put through the same reconstruction and analysis as the real data. The Monte Carlo distributions that were finally compared to the real data were these fully reconstructed and analysed distributions, with one caveat. The Monte Carlo was not run for each choice of α and β. This would have been very inefficient. Instead, events were generated for a given set of parameters and then each event was given a weight, calculated from the x_F or p_T of the D (these were recorded on the Monte Carlo tapes), to modify the distributions to other values of α or β.

When fitting to β, α was held fixed. When fitting to α, β was held fixed. The specific sequence followed was:

(1) With $\beta = 2.5$, find the best α for the μ^+ and μ^- momentum distributions separately.

(2) Using the values of α from step 1, find the best values of β for the μ^+ and μ^- p_T distributions separately.

(3) Using the best β's from step 2, find the best α's once again. These are the final values of α.

(4) Using the final α's, find the final β's.

This iterative procedure was employed in order to remove any dependence of the outcome on the intial choice of parameters. But as a matter of fact, α and β were only weakly coupled. That is, the outcome of step 3 was

not significantly different from that of step 1, and the outcome of step 4 was not significantly different from that of step 2. Below, only the final (step 3 and step 4) results will be presented.

In general, the term "fitting" as used here refers to the process of comparing Monte Carlo distributions generated with different choices of parameters to the data in order to determine which values of the parameters minimize the quantity χ^2. This quantity is defined by the equation

$$\chi^2 = \sum_i \frac{(R_i^{data} - R_i^{MC})^2}{\sigma_i^2}$$

where R_i^{data} and σ_i were the rate and the error on the rate for the ith bin, and R_i^{MC} was the Monte Carlo prediction (which was a function of the parameters, one of which was the effective branching ratio times cross section) for the ith bin. The sum was taken over the relevant bins.

The charm production cross section, as noted above, was treated as a parameter (in particular, a normalization) in this fitting procedure. However, it should be noted that the cross section is given by the formula:

$$B(1 - B)\sigma_{charm} \text{ (per nucleon)} = \frac{R_{1\mu}\sigma_{TOT}}{\varepsilon A^{\kappa}},$$

where $R_{1\mu}$ is the prompt single muon rate, σ_{TOT} is the total inelastic cross section for protons or pions on iron, ε is the acceptance for charm (i.e., the fraction of semi-leptonic charm decays which provide muons which pass all cuts), A is the atomic weight of the target (A = 56 for iron), and κ is a parameter which gives the dependence of the charm cross section on A. Typically, it will be assumed that $\kappa = 1$; the issue of A-dependence will be discussed later. The values for the total inelastic cross sections have been taken from Reference 38. They were:

$$\sigma_{TOT}(pFe) = 704 \text{ mb},$$

and

$$\sigma_{TOT}(\pi Fe) = 556 \text{ mb}.$$

It should be noted that the factor B(1 - B) enters into the charm cross section calculation (instead of B alone) because these are <u>single</u> muon results. Events in which both charmed particles decayed semi-leptonically were classified as dimuons. Therefore, the cross section is weighted by $(B - B^2)$ in the single muon data.

An uncertainty in the charm cross section derives from the fact that the value of B is not precisely known.

Indeed, the uncertainty in B has two sources. First, the mixture of different charmed particles (D°, D^+, F or Λ_c) is not known, and second, the semi-leptonic branching ratios of these states are only poorly measured. Measurements of the "average" semi-leptonic branching ratio has been measured[35] to be (8.0 ± 1.5)% for D mesons produced in the decays of the $\psi(3770)$, where the mixture is 56% neutral D's and 44% charged D's (from phase space). Recent measurements[39] of the average charm semi-leptonic branching ratio for charm states produced in e^+e^- collisions with center of mass energy of 29 GeV indicate a value of (6.3 ± 2.4)%. The mixture of charm states contributing to this average may be more representative of the hadronic production case than the D's from the $\psi(3770)$, but the errors are large. Therefore, it would seem that B could range from about 4% to perhaps 9%. Obviously, this dilutes the power of this experiment to measure the charm cross section accurately. Fortunately, several significant issues can be addressed even with this level of uncertainty.

6.3 Charm Production by Protons

In this section, the production of charmed particles in nucleon-nucleon and nucleon-nucleus interactions will be considered. The high-p data from this experiment, discussed in Chapter 4, will be considered in Section 6.3.1. The results of other experiments will then be summarized and compared, where possible, to these results in Section 6.3.2.

6.3.1 Results from the Proton High-p Data

In discussing the proton high-p data, the following four questions will be addressed:

1) What is the total charm cross section?
2) Is the production dominately forward or central?
3) What level of associated $\Lambda_c\bar{D}$ production is allowed by the data?
4) Is the intrinsic charm model viable?

In order to address the first two questions, the hypothesis of D meson production, according to

$$E \frac{d^3\sigma}{dp^3} \sim (1 - x_F)^{\alpha} e^{-\beta p_T},$$

where x_F is the Feynmann x and p_T the transverse momentum

of the D, has been explored (see Section 6.2 for a discussion of the fitting procedure and the assumptions made). A fit to the prompt single μ^+ momentum distribution yielded $\alpha^+ = 4.2^{+1.8}_{-1.3}$, and a fit to the prompt single μ^- momentum distribution yielded $\alpha^- = 5.5^{+1.1}_{-1.0}$. Figure 6-2 shows the χ^2 distribution versus α for these fits. The values of α are consistent with being equal within errors. In view of the near equality of the total prompt single μ^+ and μ^- rates, the hypothesis of equal D and $\bar{D}$ production with the same α (i.e., $\alpha^+ = \alpha^-$) is quite natural. Indeed, this model provided a good χ^2 when fit simultaneously to both the μ^+ and μ^- distributions. The best value of α was 5.0 ± .9, and the best cross section (times branching ratio) was

$$B\ (1 - B)\ \sigma_{D\bar{D}} = 1.57 \pm .15 \pm .26\ \mu b/\text{nucleon},$$

and where B is the average semi-muonic branching ratio. This cross section is for the entire x_F range (i.e., $-1 < x_F < 1$), based on the assumption that the backward hemisphere is the same as the forward hemisphere. The first error reflects the errors in the rates and the second comes from the uncertainty in α. An $A^{1.0}$ dependence of the charm cross section has been assumed. (If $A^{2/3}$ were assumed, the above cross section would be increased by a factor of 3.8.) The issue of A-dependence will be discussed in Section 6.3.2.

Figure 6-3 shows the χ^2 and the cross section (times branching ratio) versus α for the simultaneous fit described above. Figure 6-4 shows the prompt single muon rates as a function of momentum and the Monte Carlo rates calculated for $\alpha = 5$.

Therefore, it appears that the data can be accounted for by purely central production of D mesons with a total cross section in the range of 20 to 40 μb/nulceon, where most of the uncertainty comes from the uncertainty in the branching ratio B (see Section 6.2 for a discussion of B).

Both as a check on the model dependence of these results and to facilitate comparisons to other experiments, fits to the non-invariant parameterization of the charm cross section ($d\sigma/dx \sim (1 - x_F)^n$) have also been performed. The result was that $n = 6.0 \pm .8$ and $B(1 - B)\sigma_{D\bar{D}} = 1.21 \pm .11 \pm .18$ μb/nucleon.

The results of fits to the transverse momentum distributions of the prompt single muons, in the form of χ^2 curves versus β, are shown in Figure 6-5, for fits to the μ^+ and μ^- distributions separately. The figure also shows the sum of the two χ^2 curves, which gives the best value of β to be $2.0 \pm .4$. Figure 6-6 shows the prompt single muon rates versus p_T along with the Monte Carlo distributions for $\beta = 2$.

Two other parameterizations of the p_T distributions

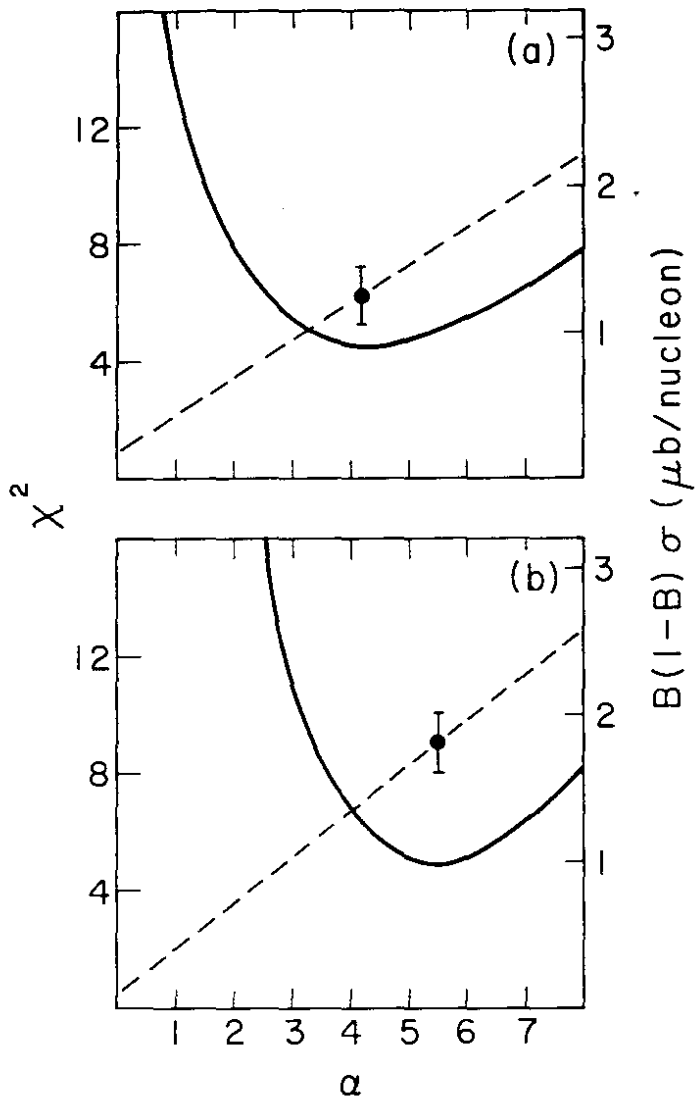

Figure 6-2: Results of fits to the proton prompt single (a) μ^+ and (b) μ^- momentum distributions. The solid curves give χ^2 and refer to the left axis. The dashed curves give $B(1 - B)\sigma$ and refer to the right axis.

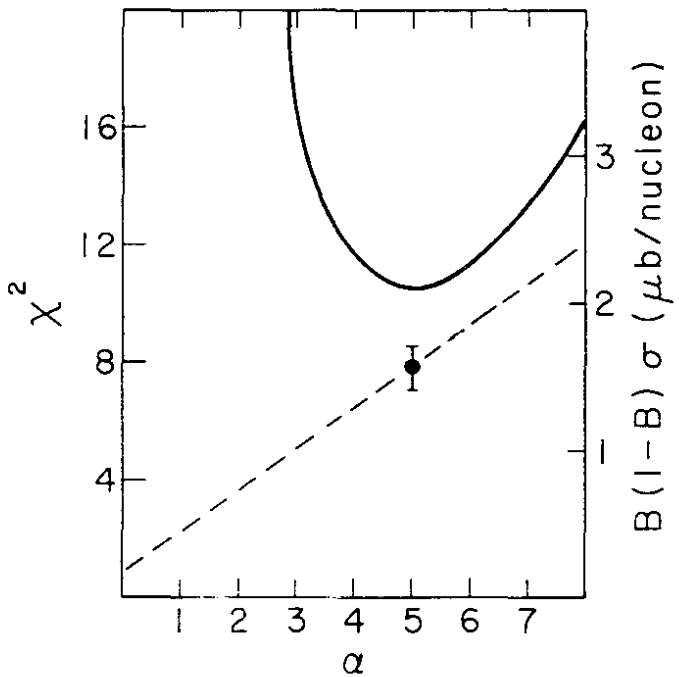

Figure 6-3: Results of a simultaneous fit to μ^+ and μ^- momentum distributions. The solid curve gives χ^2 and the dashed curve gives $B(1 - B)\sigma_{D\bar{D}}$.

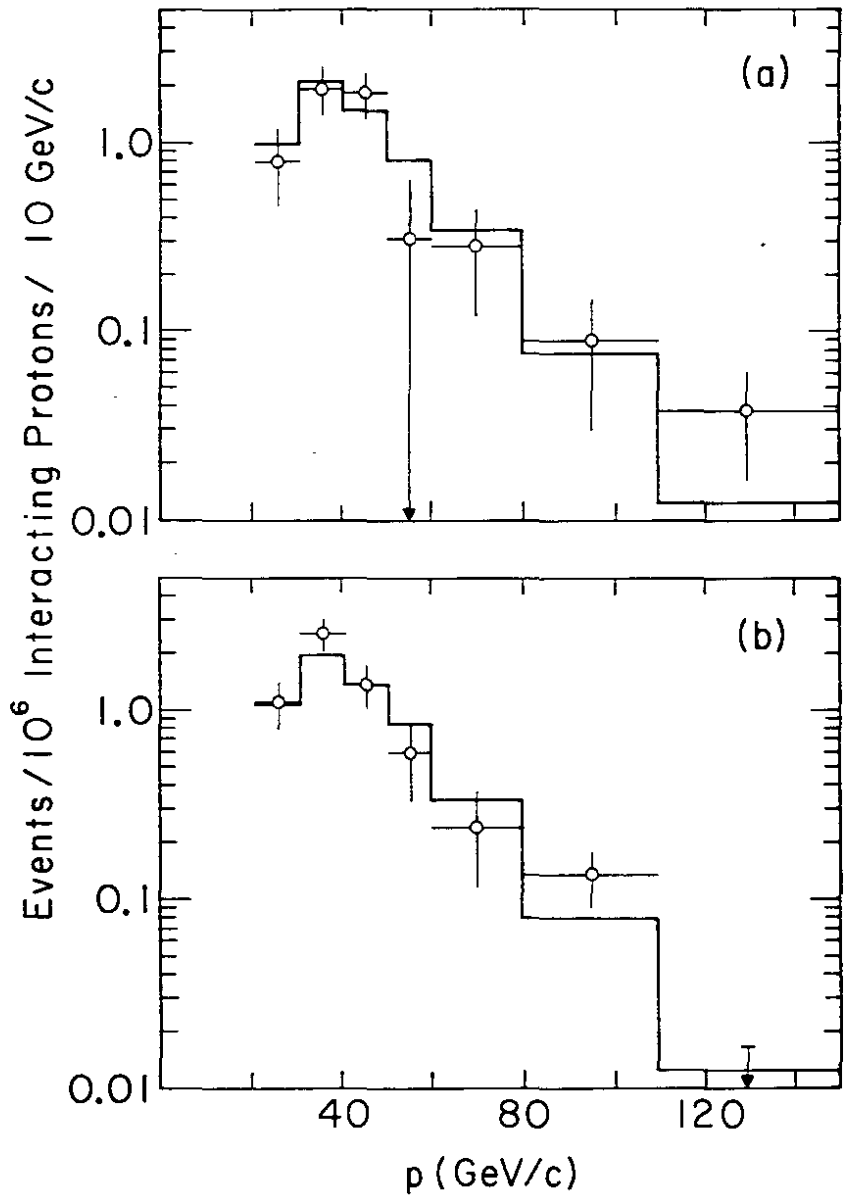

Figure 6-4: Prompt single (a) μ^+ and (b) μ^- rates versus momentum from the proton data. The solid curve gives the Monte Carlo distribution for $\alpha = 5$.

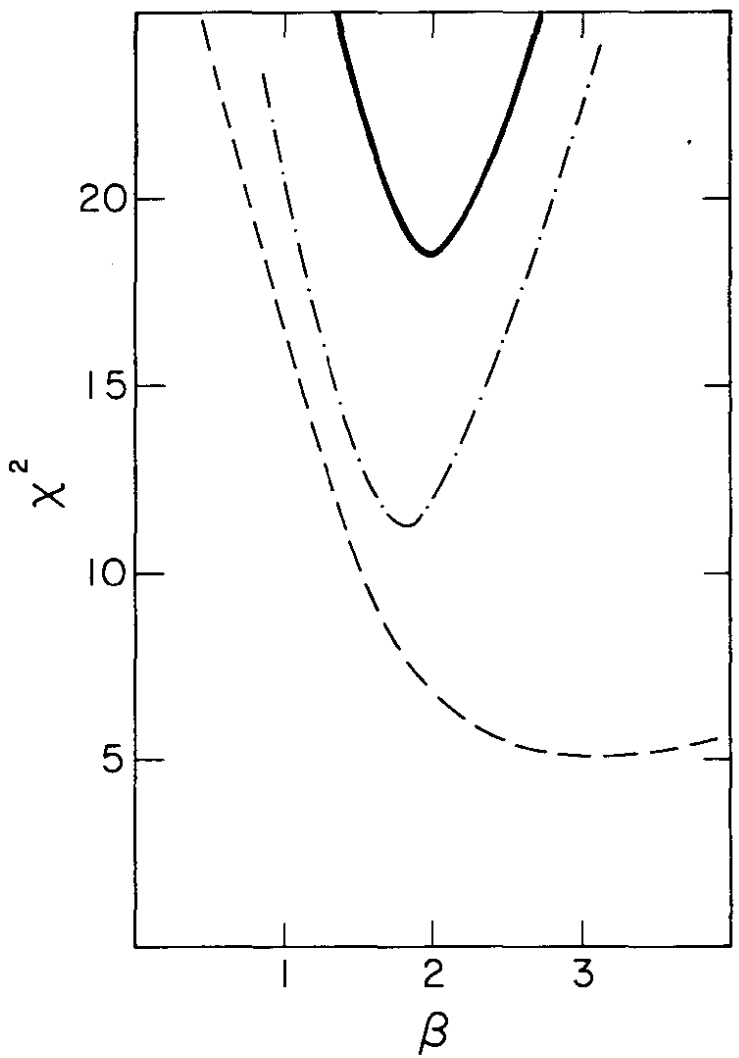

Figure 6-5: Results of fits to the transverse momentum distributions of prompt single muons produced by protons. The curves give χ^2 for μ^+ (dashed line) and μ^- (dot-dashed line) fits. The solid curve is the sum of μ^+ and μ^-.

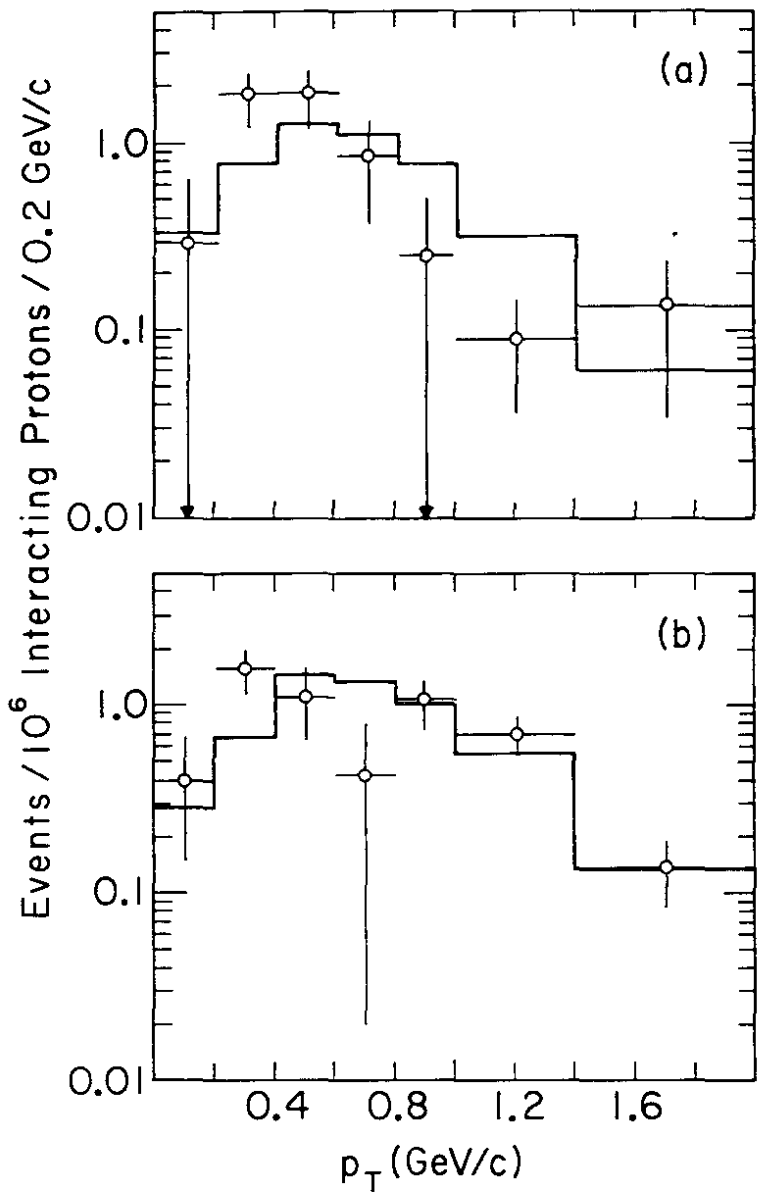

Figure 6-6: Proton prompt single muon rates versus transverse momentum for (a) μ^+ and (b) μ^-. The solid curves give the Monte Carlo distribution for $\beta = 2$.

have also been tried, not because the data is of sufficient quality to decide between them, but to facilitate comparisions with other experiments which use these parameterizations. They were: (1) $e^{-\beta' m_T}$, where $m_T = (p_T^2 + m_D^2)^{.5}$, and (2) $e^{-\beta'' p_T^2}$. The results were that $\beta' = 3.5 \pm .7$ and $\beta'' = .75 \pm .20$.

The issue of associated $\Lambda_c\bar{D}$ production is difficult to address because the x_F distributions of these particles are unknown. Therefore, the best that can be hoped is to extract an order of magnitude estimate of the level of the cross section for this process. For the Λ_c, it will be assumed that the production goes as $(1 - x_F)^1$, following quark counting arguments.[40] There seems to be no reason to assume that $\bar{D}$'s produced in association with Λ_c's should necessarily have a different x_F distribution than those produced along with D's. Therefore, the approach taken here is to ask what fraction of the prompt single μ^+ distribution could result from Λ_c production according to $(1 - x_F)^1$ in combination with the central production of D's according to $(1 - x_F)^{5.5}$ (which was the best fit to the μ^- distribution alone; see above). Note that a non-zero result from this calculation is guaranteed by the fact that the μ^+ distribution favored a value of α smaller than 5.5. It should be recalled, however, that while this test will establish the level of Λ_c production allowed, such production is not required to

explain the observed rates. With these qualifications, the result is

$$B'\sigma_{\Lambda_c} = .19 \pm .29 \ \mu b/\text{nucleon},$$

where B' is the appropriate effective branching ratio. Linear A-dependence has been assumed. The cross section would be larger by a factor of 3.8 if $A^{2/3}$ were assumed. The semi-leptonic decays of the Λ_c were generated according to the assumptions listed in Section 6.2.

The value of B', which is equal to $B_{\Lambda_c}(1 - B_{\bar{D}})$, is of course rather uncertain. The only measurement[41] of the semi-leptonic branching ratio of the Λ_c is $(4.5 \pm 1.7)\%$. (Lifetime measurements are in reasonable agreement with this branching ratio.) Therefore, a sensible assumption is that $B' = .044 \pm .017$. Using the measured branching ratio, $\sigma_{\Lambda_c} = 4.3 \pm 6.6$ μb/nucleon (assuming $A^{1.0}$).

If the Λ_c semi-leptonic branching ratio were extremely small (or zero), large $\Lambda_c\bar{D}$ production would lead to a μ^- excess in the prompt single muon rates. The absence of such an excess in the data can be used to set an upper limit on $\Lambda_c\bar{D}$ production. Figure 6-7 shows the maximum allowed value for the $\Lambda_c\bar{D}$ cross section as a function of B_{Λ_c}. The limit at large B_{Λ_c} comes from the μ^+ data alone (see above). The limit at small B_{Λ_c} comes from the measured $(\mu^- - \mu^+)$ difference of $.46 \pm 1.17$ events per 10^6 interacting protons. The assumptions in

the calculation of this upper limit were that Λ_c's are produced according to $(1 - x_F)^1$ and D's (both D and $\bar{D}$) are produced according to $(1 - x_F)^{5.5}$. The semi-leptonic branching ratio of the $\bar{D}$'s produced in association with Λ_c's has been conservatively assumed to be 4%. The limit assumes $A^{1.0}$ dependence of the cross section. For $A^{2/3}$ dependence, the limit would be increased by a factor of 3.8.

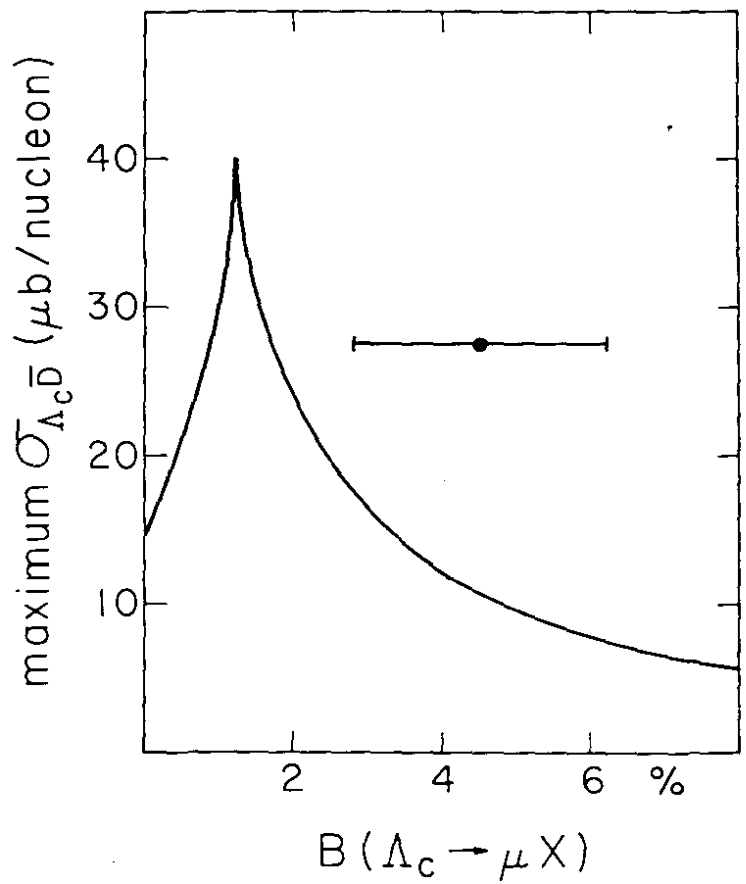

Figure 6-7: The maximum allowed cross section for associated $\Lambda_c\bar{D}$ production in 350 GeV proton interactions, versus the semi-leptonic branching ratio of the Λ_c. The data point is the measured semi-leptonic branching ratio from Reference 41.

Finally, the viability of the intrinsic charm hypothesis can be investigated with this data. According to this model, in 350 GeV proton interactions the cross section for $\Lambda_c\bar{D}$ production should be about 210 μb/nucleon (for a 1% intrinsic charm component in the proton wave function). The previous result for associated $\Lambda_c\bar{D}$ production obviously rules this out. However, the above calculation took the x_F distribution of the Λ_c to be $(1 - x_F)^1$. The intrinsic charm model[34] makes a prediction for the x_F distributions of both the Λ_c and the $\bar{D}$. Using these distributions (which give production peaked near $x_F = .5$) and assuming that all prompt single muons with momentum greater than 50 GeV/c arrise from the decays of these diffractively produced states, the result is that

$$B'\sigma_{IC} = .44 \pm .13 \ \mu b/\text{nucleon},$$

and

$$B''\sigma_{IC} = .37 \pm .09 \ \mu b/\text{nucleon}.$$

Here σ_{IC} is the intrinsic charm cross section. An $A^{2/3}$ dependence has been assumed since that is an explicit prediction of the model.[42] The effective Λ_c semi-leptonic branching ratio has been discussed above; it is assumed here that $B' = .044$. The quantity B'' is the effective average branching ratio of the $\bar{D}$'s produced along with

the Λ_c. A conservative (i.e., low) assumption is to take $B'' = .04$. Then it follows that σ_{IC} is 10.0 ± 3.0 and 9.3 ± 2.3 μb/nucleon, respectively. These cross sections correspond to intrinsic charm components of the proton of .048% and .044%, respectively, far below the predicted 1%. Other stringent limits on the intrinsic charm component have been set by the EMC collaboration[43] in an experiment which investigated the production of charm by muons, and also by this experiment through an analysis of dimuons with large missing energy.[44]

6.3.2 Other Proton Experiments

Several experiments have investigated the production of charmed particles in proton interactions. For the most part, in this discussion emphasis will be placed on other prompt (single) lepton measurements, namely neutrino beam dump experiments. However, results of a few "direct" searches will also be considered.

Neutrino beam dump experiments were discussed in Chapter 1. The relative strengths and weaknesses of that technique, as compared to observing prompt single muons, were explored. There have been three beam dump runs at CERN. Results from the third run are not yet available. Results from the first run[45] will not be considered. Only the results from the three second run experiments (CDHS[16], CHARM[46], and BEBC[47]) will be discussed. Also, the neutrino beam dump experiment (E613[48]) performed at Fermilab will be considered.

The ratio $\bar{\nu}_\mu/\nu_\mu$ determined in neutrino beam dump experiments should be equal to the ratio μ^-/μ^+ determined in this experiment, provided the leptons arise from the same source. Figure 6-8 shows this ratio for each experiment. The neutrino experiments are comparable to the high-p data because they require minimum values for the neutrino energy similar to the 20 GeV requirement placed by the high-p trigger on the muon (E > 20 GeV for

CDHS and CHARM, E > 10 GeV for BEBC, and E > 25 GeV for E613). A small correction (5%) has been applied to the μ^-/μ^+ ratio to account for the small difference between the acceptance for the two signs of muon.

A special comment must be made regarding the value of $\bar{\nu}_\mu/\nu_\mu = 1.10 \pm .52$ shown in the figure for E613. Another value, $\bar{\nu}_\mu/\nu_\mu = 1.12 \pm .24 \pm .17$, obtained by a different method, was also published in Reference 48. The value with the larger error is shown in the figure because of the curious history of this ratio from E613. It has been reported to be .80 ± .19 (Reference 49; April, 1982), .65 ± .30 (Reference 50; August, 1982), 1.01 ± .24 (Reference 51; October, 1982), and also 1.09 ± .25 (Reference 52; May, 1983). In view of this migration, the more conservative error is perhaps the more reliable.

Charm production cross sections have been calculated by all of these groups. Only one experiment has performed fits to the x_F and p_T distributions. Using the same parameterization as used here (see Section 6.2), E613 found $\alpha = 4 \pm 1$ and $\beta = 2 \pm .5$.

In order to make a direct comparison between experiments, it is necessary to compare cross sections calculated under the same assumptions. Table 6-1 shows such a comparison. For all experiments included,

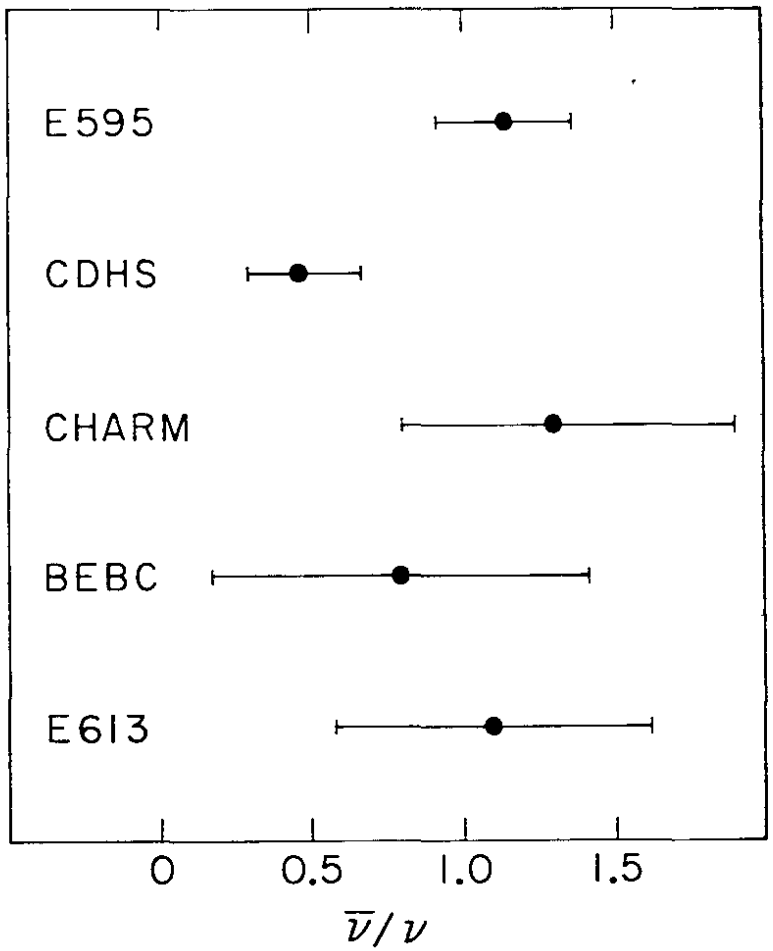

Figure 6-8: The ratio $\bar{\nu}_\mu/\nu_\mu$ from the neutrino beam dump experiments and the ratio μ^-/μ^+ from this experiment (E595).

Table 6-1: Cross sections from neutrino beam dump experiments and E595, calculated under the same model and branching ratio assumptions; in particular, a $(1 - x_F)^4$ distribution and an 8% semi-leptonic branching ratio were assumed. See the text for details. The errors given reflect only the errors in rates and not uncertainties from model dependence. Cross sections are given in units of μb/nucleon.

Expt	σ_{charm} $A^{1.0}$	σ_{charm} $A^{2/3}$	material
E595	17.8 ± 1.6	68 ± 6	Fe (A = 56)
CHARM (ν_e)	19 ± 6	76 ± 24	Cu (A = 63.5)
BEBC (ν_e)	17 ± 4	68 ± 16	Cu
BEBC (ν_μ)	30 ± 10	120 ± 40	Cu
E613 (ν_μ)	27 ± 4	154 ± 23	W (A = 184)
average	19.6 ± 1.4	79 ± 5	
	χ^2 = 3.4	χ^2 = 10.6	

$D\bar{D}$ production according to $(1 - x_F)^4 e^{-2p_T}$ has been assumed, along with an 8% semi-leptonic branching ratio. It was not possible to include CDHS because of the form in which they reported results (see below). Different experiments have made different assumptions for secondary charm production, but these effects are small.

The cross section given in Table 6-1 for this experiment (E595) has been increased by 11% to account for the different beam energies (350 GeV for E595, 400 GeV for all others). This correction is based on the energy dependence from Reference 37 (see Section 6.2). The table gives cross sections for both $A^{1.0}$ and $A^{2/3}$ dependences.

The CERN experiments used a copper dump, while E613 used tungsten (recall that E595 used iron). This allows the A-dependence of charm production to be investigated. A fit to the hypothesis that all cross sections are equal yields a χ^2 of 3.4 for $A^{1.0}$ and a χ^2 of 10.8 for $A^{2/3}$ (4 degrees of freedom). Linear A-dependence seems strongly favored. However, it should be noted that E613 has recently reported[53] (from a comparison of prompt ν_e production from beryllium and tungsten) that $\sigma_{charm} \sim A^{.72}$. If so, then the cross section from E613 is in poor agreement both with this experiment (E595) and with the CERN beam dump experiments.

An interesting feature of the cross sections shown in

Table 6-1 is that the ν_e measurements agree with E595, while the ν_μ measurements are higher. Recall that backgrounds such as beam scraping, target punch-through, etc., contribute mainly to the ν_μ flux.

The CDHS group has interpreted the $\bar{\nu}_\mu/\nu_\mu$ ratio measured in their experiment ($.48^{+.21}_{-.16}$) as sizeable production of charmed baryons in the forward direction. They report

$$B_{\Lambda_c}\sigma_{\Lambda_c} = 3.9 \pm 1.0\ \mu b/\text{nucleon},$$

assuming linear A-dependence. This value is inconsistent with the E595 result (see Section 6.3.1) of

$$B'\sigma_{\Lambda_c} = .19 \pm .29\ \mu b/\text{nucleon},$$

also assuming linear A-dependence (the x_F distributions for Λ_c production have been assumed to be $(1 - x_F)^1$ in both cases). Other fixed target experiments[54] have also reported charmed baryon cross sections which cannot be resolved with E595 (no matter what the Λ_c semi-leptonic branching ratio is; see Section 6.3.1 and Figure 6-7).

By far the most successful proton fixed target <u>direct</u> charm search has been NA16 at CERN, using LEBC (the LExan Bubble Chamber) followed by the European Hybrid Spectrometer.[55] This experiment has reported a D meson cross section of 28^{+13}_{-6} μb for 360 GeV protons incident on a hydrogen target. This cross section taken together

a hydrogen target. This cross section taken together with those in Table 6-1 provides more evidence for $A^{1.0}$ dependence of the charm cross section. The NA16 group parameterized the x_F distribution by $d\sigma/dx_F \sim (1 - x_F)^n$ and found $n = 1.8 \pm .8$. This is flatter than the

$E\, d\sigma/dx_F \sim (1 - x_F)^{5.0 \pm .9}$ from this experiment. They parameterized the p_T distribution as $d\sigma/dp_T^2 \sim e^{-ap_T^2}$ and found $a = 1.1 \pm .3$, to be compared with $.75 \pm .20$ from this experiment. No Λ_c's have been observed by NA16, although an excess of observed $\bar{D}$'s (7 events) over D's (2 events) can be interpreted as associated $\Lambda_c\bar{D}$ production with cross section in the range 15 to 50 μb. Of course, with such low statistics any interpretation is dubious.

Experiments[56] at center of mass energy of 62 GeV at the ISR proton-proton collider have reported extremely large charm cross sections (.4 to 1 mb), much of which is attributed to Λ_c production. Because of the high energy of these experiments, it is not possible to make direct comparisons (E_{cm} = 25.6 GeV for E595). Theoretical extrapolations using the flavor creation model and the intrinsic charm model cannot accommodate both the lower energy and higher energy results. Flavor excitation, with sufficiently small Q^2_{min} (see Section 6.1), may be able to accommodate both.[57]

6.4 Charm Production by Pions

In this section, the production of charmed particles in pion-nucleon and pion-nucleus interactions will be considered. The high-p data discussed in Chapter 5 will be considered in Section 6.4.1. Other experiments will be summarized and compared to this experiment in Section 6.4.2.

6.4.1 Results from the Pion High-p Data

The prompt single muon rates from the pion data exhibit an important property not seen in the proton data. Namely, the prompt single μ^- rates are greater than the prompt single μ^+ rates by about a factor of two. Figure 6-9 shows the ratio μ^-/μ^+ for both the pion and proton data for all events with momentum greater than p_{min}, plotted versus p_{min}.

The questions which will be addressed in discussing the pion data are:

1) How can the difference in μ^+ and μ^- rates be explained?
2) What is the charm production cross section with pions?
3) Is charm production dominantly forward or central?
4) What limit can be set on the intrinsic charm component of the pion?

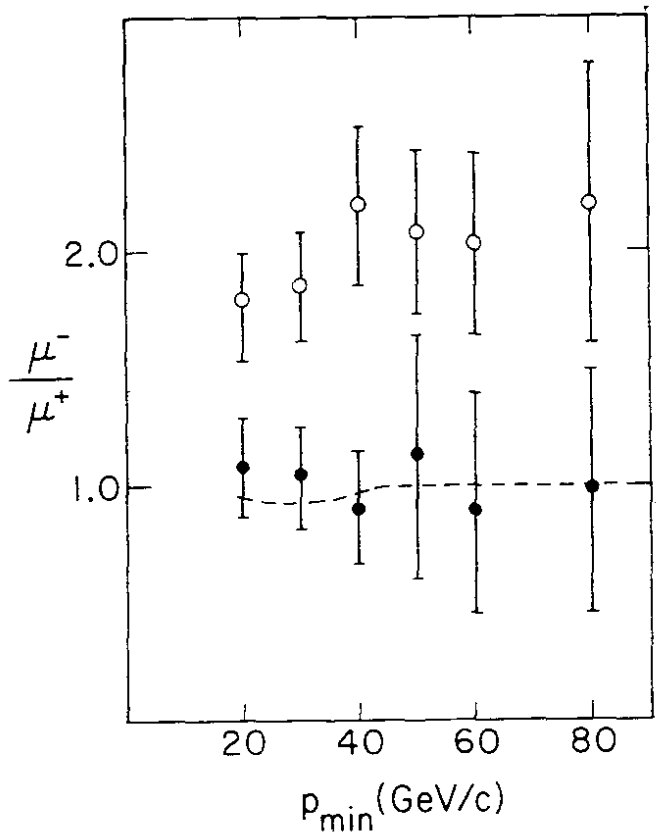

Figure 6-9: The ratio of μ^-/μ^+ for prompt single muons with momentum greater than p_{min}, versus p_{min}, for the proton (solid dots) and pion (open circles) data. The dashed curved shows the expected ratio (including acceptance) for equal production.

The first three questions will prove to be so interrelated that they cannot be answered separately.

The difference in the μ^+ and the μ^- rates implies that charmed particles (which contain a c quark) and charmed antiparticles (which contain a $\bar{c}$ antiquark) must either be produced differently or that they must decay differently. Of course, in strong interactions charmed particles must be produced in pairs, and any particle and its antiparticle must have the same branching ratios to the appropriate charge conjugate states. Nonetheless, there are plausable scenarios which could lead to such an effect. Three are:

(i) D's and $\bar{D}$'s might be produced with different x_F distributions. Here it is assumed that D's and $\bar{D}$'s are made up of the same mixture of charmed states (so that the average branching ratio is the same) and are produced with the same cross section. If the $\bar{D}$ distribution were flatter, the acceptance for μ^-'s from $\bar{D}$ decays would be larger than for μ^+'s from D decays, causing a μ^- excess in the data.

(ii) A mechanism such as $\Lambda_c\bar{D}$ production could be important. The Λ_c would be "target-like" and would therefore be at negative (or at least very small) x_F. Consequently, no μ^+'s would be observed from this process.

(iii) More D^0's and D^-'s might be produced than D^+'s

and $\bar{D}^{\circ}$'s (because both the $D^{\circ}(c\bar{u})$ and $D^{-}(\bar{c}d)$ have a valence quark in common with the beam $\pi^{-}(\bar{u}d)$, while the $D^{+}(c\bar{d})$ and $\bar{D}^{\circ}(\bar{c}u)$ do not). Charged D's are known to have a larger semi-leptonic branching ratio than neutral D's, and this could account for the μ^{-} excess. In this case, the D's which carry the pion valence quarks might be expected to have flatter x_F distributions than those which do not. If so, the acceptance for observing μ's from the decays of D°'s and D^{-}'s would be enhanced, leading to an even larger μ^{-} excess than would otherwise be the case.

The μ^{+} and μ^{-} momentum distributions have separately been fit to the hypothesis of D meson production according to

$$E \frac{d^3\sigma}{dp^3} \sim (1 - x_F)^{\alpha} e^{-\beta p_T},$$

where x_F is the Feynmann x and p_T the transverse momentum of the D. The χ^2 curves versus α for both of these fits are shown in Figure 6-10. The best values are $\alpha^{+} = 2.1 \pm .5$ and $\alpha^{-} = 1.6 \pm .3$. These values are consistent with being equal, although a flatter distribution is favored for $\bar{D}$'s. Indeed, if equal values of $B(1 - B)\sigma$ are assumed for both D's and $\bar{D}$'s, but the

α's are taken to be equal to their best fit values, then the predicted μ^{-}/μ^{+} ratio would be 1.19. This is significantly less than the observed ratio of $1.78 \pm .20$. Even for the extreme case $\alpha^{+} = 2.6$ and $\alpha^{-} = 1.3$ (the extreme values allowed for both parameters), the ratio would be 1.55, still more than a standard deviation below the measured ratio. Therefore, it appears that hypothesis (i) is ruled out.

The results of the fits to the transverse momentum distributions are shown, in the form of χ^2 curves versus β, in Figure 6-11, for the μ^{+} and μ^{-} distributions separately. The figure also shows the sum of the two χ^2 curves, which gives the best value of β to be $2.0 \pm .3$. Figure 6-12 shows the prompt single muon rates versus p_T along with the Monte Carlo distributions for $\beta = 2$.

Two other parameterizations of the p_T distributions have also been tried. They were: (1) $e^{-\beta' m_T}$, where $m_T = (p_T^2 + m_D^2)^{.5}$, and (2) $e^{-\beta'' p_T^2}$. The results were that $\beta' = 3.5 \pm .5$ and $\beta'' = .70 \pm .15$.

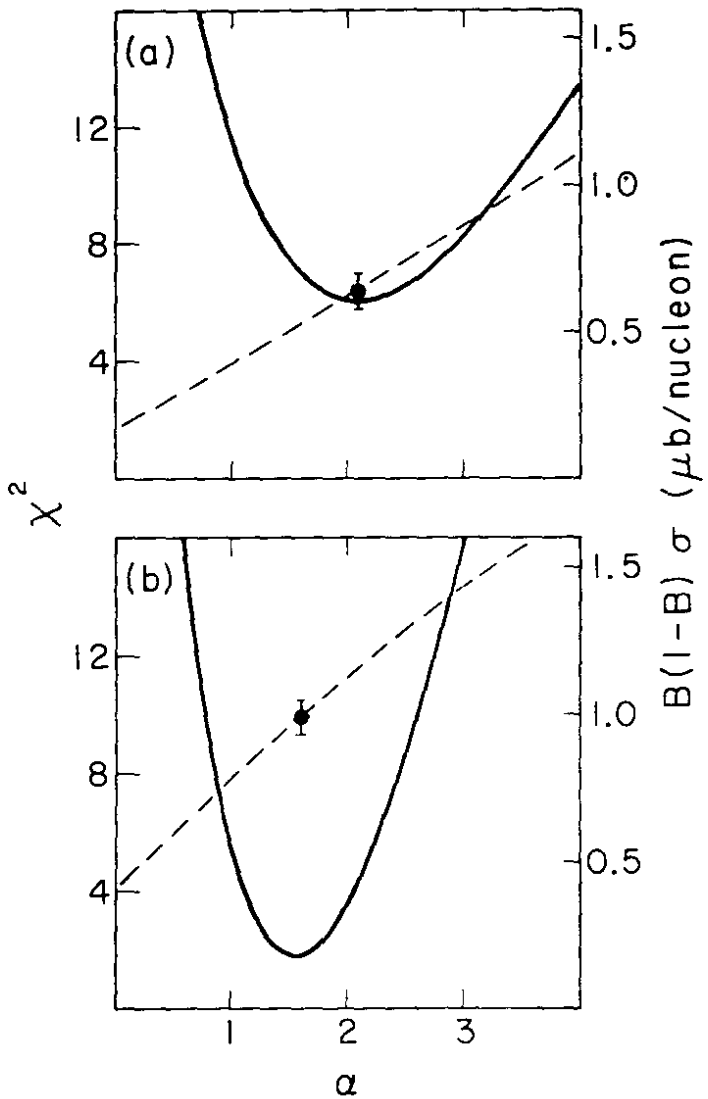

Figure 6-10: The χ^2 curves (solid curves) versus α for fits to the momentum distributions of prompt single (a) μ^+'s and (b) μ^-'s produced by pions. The dotted curves refer to the right axis and give B(1 - B)σ.

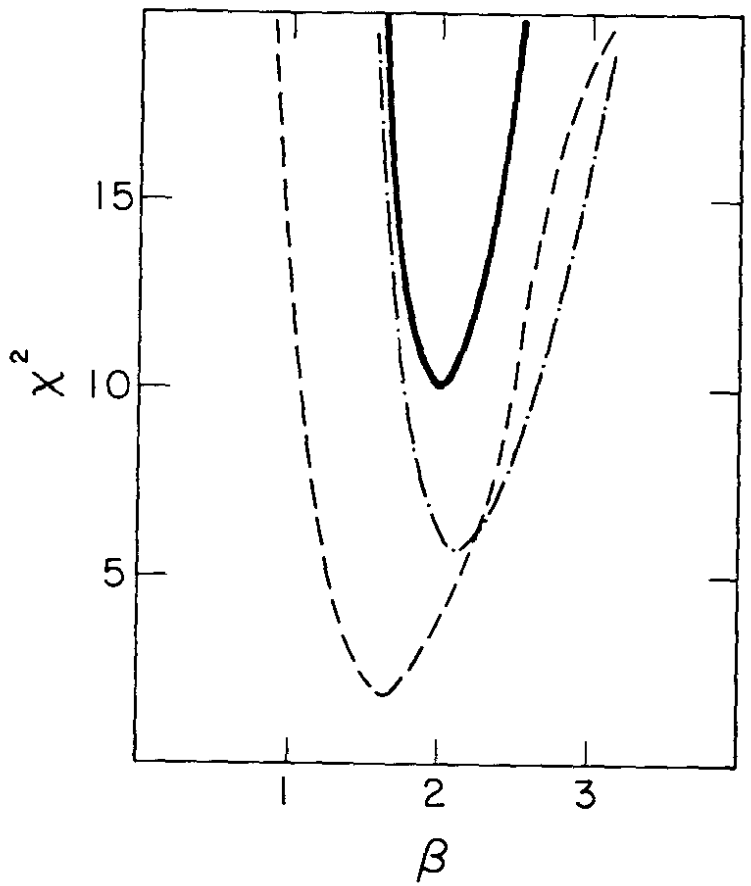

Figure 6-11: The χ^2 curves versus β for fits to the p_T distribution of prompt single μ^+'s (dashed) and μ^-'s (dot-dashed) produced by pions. The solid curve is the sum.

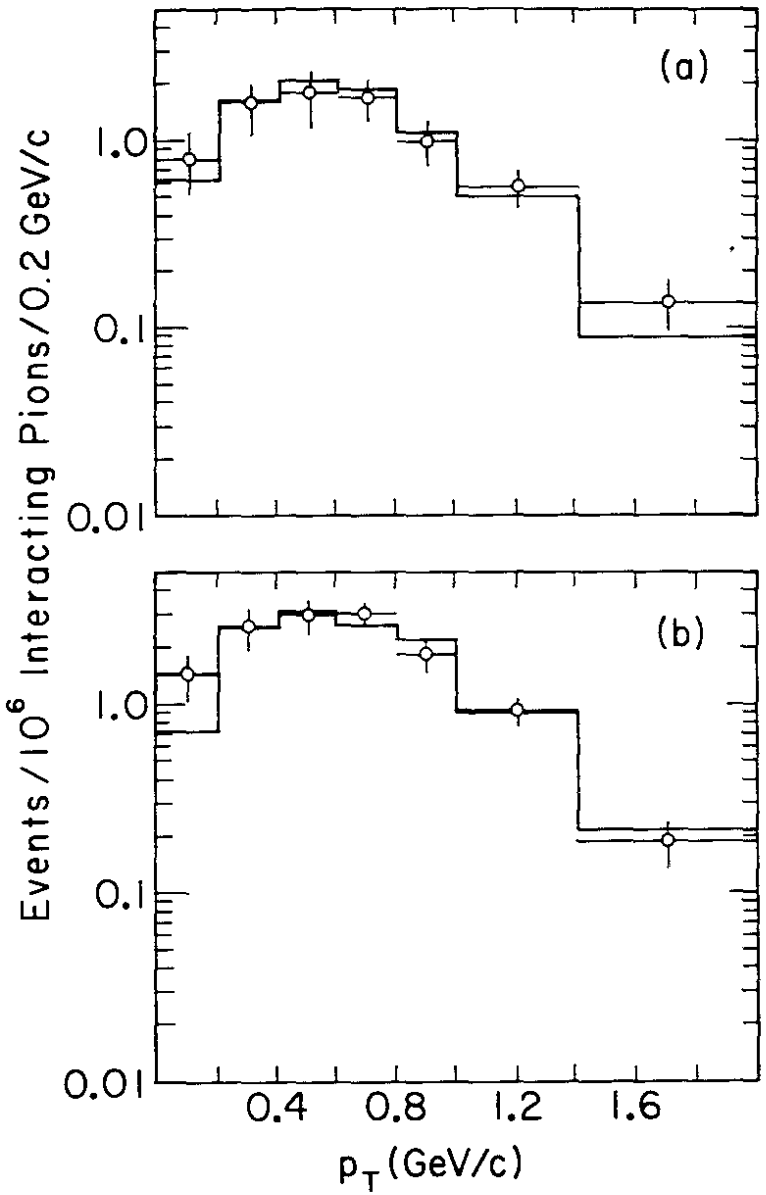

Figure 6-12: Pion prompt single muons rates versus p_T for (a) μ^+'s and (b) μ^-'s. The solid curves show the Monte Carlo distributions for $\beta = 2$.

The hypothesis of substantial associated $\Lambda_c\bar{D}$ production cannot be ruled out by these data. It is possible, however, to determine the level of the cross section that would be required to explain the μ^- excess and also the x_F distribution of the $\bar{D}$'s. Since this process contributes only to the observed μ^-'s, the $(\mu^- - \mu^+)$ difference isolates this contribution. A fit to the $(\mu^- - \mu^+)$ distribution yields a best α of $.8 \pm .6$, and

$$B\sigma_{\bar{D}} = .3 \pm .1\ \mu b/\text{nucleon}.$$

Here $A^{1.0}$ has been assumed. The cross section also assumes that the $\bar{D}$'s are produced only for $x_F > 0$.

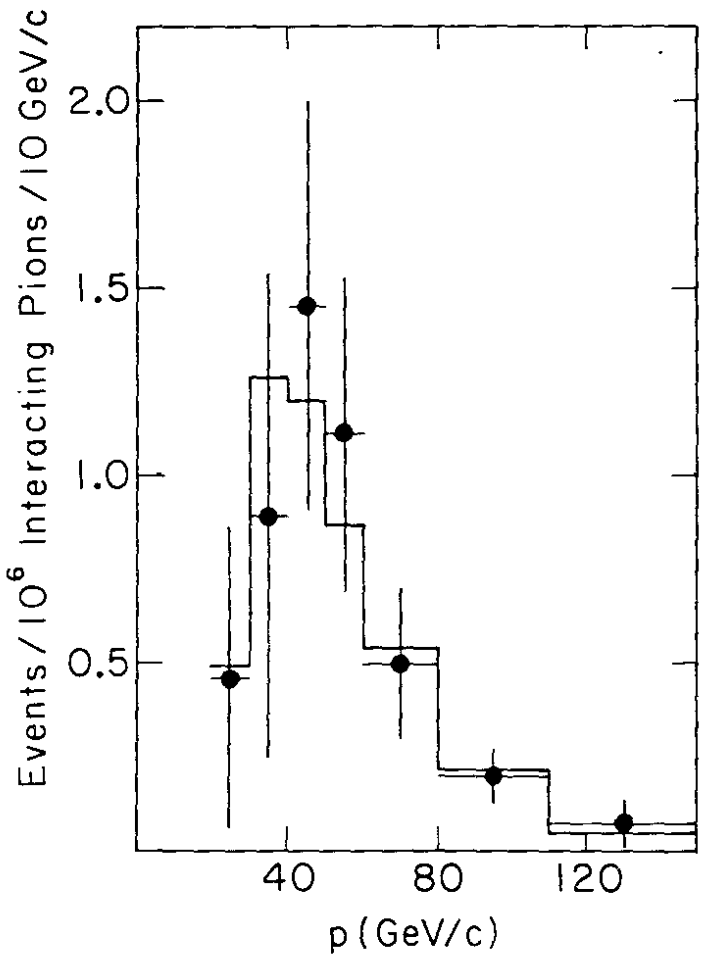

Figure 6-13: The (μ^- - μ^+) distribution versus momentum. The solid curve shows The Monte Carlo distribution for α = .8.

The hypothesis of more D° and D^- production than D^+ and $\bar{D}^\circ$ production can also account for the observed μ^- excess. A natural way to investigate this would be to parameterize the x_F distribution of each charmed state separately (e.g., $D^+ \sim (1 - x_F)^a$, $D^\circ \sim (1 - x_F)^b$, $D^- \sim (1 - x_F)^c$, and $\bar{D}^\circ \sim (1 - x_F)^d$). In view of the similarities of D^+ and $\bar{D}^\circ$ production, it would be reasonable to assume a = d. Also, in view of the similarities of D° and D^- production, it would be reasonable to assume b = c. Unfortunately, the production of D^*'s confuses matters. For example, if a D^{*-} is produced at high x_F via recombination of a $\bar{c}$ antiquark with the valence d quark from the beam π^-, it will decay about 2/3 of the time into a $\bar{D}^\circ$, which will also be at high x_F. That is, the production of D^*'s "mixes" the recombined states with the unrecombined states.

This problem may be avoided if the distinction is drawn between a recombination component and a non-recombination component, rather than between the charmed states themselves. In particular, the data have been compared to a model in which it is assumed that produced charmed particles belong to one of two distributions. One component, the recombination component, has an x_F distribution given by $(1 - x_F)^{\alpha_r}$ and cross section times branching ratio equal to $B_r(1 - B)\sigma_r$.

An additional parameter is required to characterize the difference in the D° and the D^- semi-leptonic branching ratios. This parameter is taken to be the effective ratio of the D^- to D° branching ratios and will be denoted by R. The other component, the non-recombination component, is assumed to have an x_F distribution given by $(1 - x_F)^{\alpha_n}$ and cross section times branching ratio equal to $B_n(1 - B)\sigma_n$. Since there is no reason to expect the mixtures of charged and neutral D's to be different for charmed and anticharmed particles within this component, no difference in the branching ratios to μ^+'s and μ^-'s has been assumed.

This model provides a good fit to the data ($\chi^2 = 3$ for 8 degrees of freedom). The results are:

$\alpha_r = .55^{+.45}_{-.51}$, $B_r(1 - B)\sigma_r = .32^{+.17}_{-.14}$ μb/nucleon,
$R = 2.51^{+1.03}_{-.51}$, $\alpha_n = 6.6^{+4.5}_{-2.3}$, and
$B_n(1 - B)\sigma_n = .96^{+.41}_{-.32}$ μb/nucleon. Assuming $B_r = B_n$, the total charm cross section (recombination plus non-recombination) is given by
$B(1 - B)\sigma_{charm} = 1.29^{+.40}_{-.29}$ μb/nucleon, where the fraction of the total that belongs to the recombination component is $.25^{+.15}_{-.10}$. These cross sections have been calculated only for $x_F > 0$. Linear A-dependence has been assumed. If $A^{2/3}$ were assumed, the cross sections would be increased by a factor of 3.8.

Within the context of this model, these results

indicate that recombination with valence quarks of the beam particle leads to a rather forward production distribution, while production of charmed particles without recombination is rather central. The recombination seems to occur for about 25% of the produced charmed particles.

Cross section estimates are subject to branching ratio uncertainties, but the total (forward plus central) charm cross section appears to be in the range of 15 to 30 μb/nucleon ($x_F > 0$, linear A-dependence).

If this picture is correct, then the value of R is a measure of the ratio of the semi-leptonic branching ratios of charged to neutral D's. The possible production of D^*'s (at an unknown level) complicates the interpretation of R. The effect of D^* production (because D^*'s decay predominantly to D°'s) is to reduce the effective (i.e., measured) ratio. If there were no D^* production, the measured value could only increase. Therefore, the value of $R = 2.51^{+1.03}_{-.51}$ is actually a lower limit on the ratio of branching ratios. A maximum likelihood analysis, within the context of this model, shows that

$$\frac{B(D^- \to \mu X)}{B(D^\circ \to \mu X)} > 1.8 \quad \text{(90\% confidence level).}$$

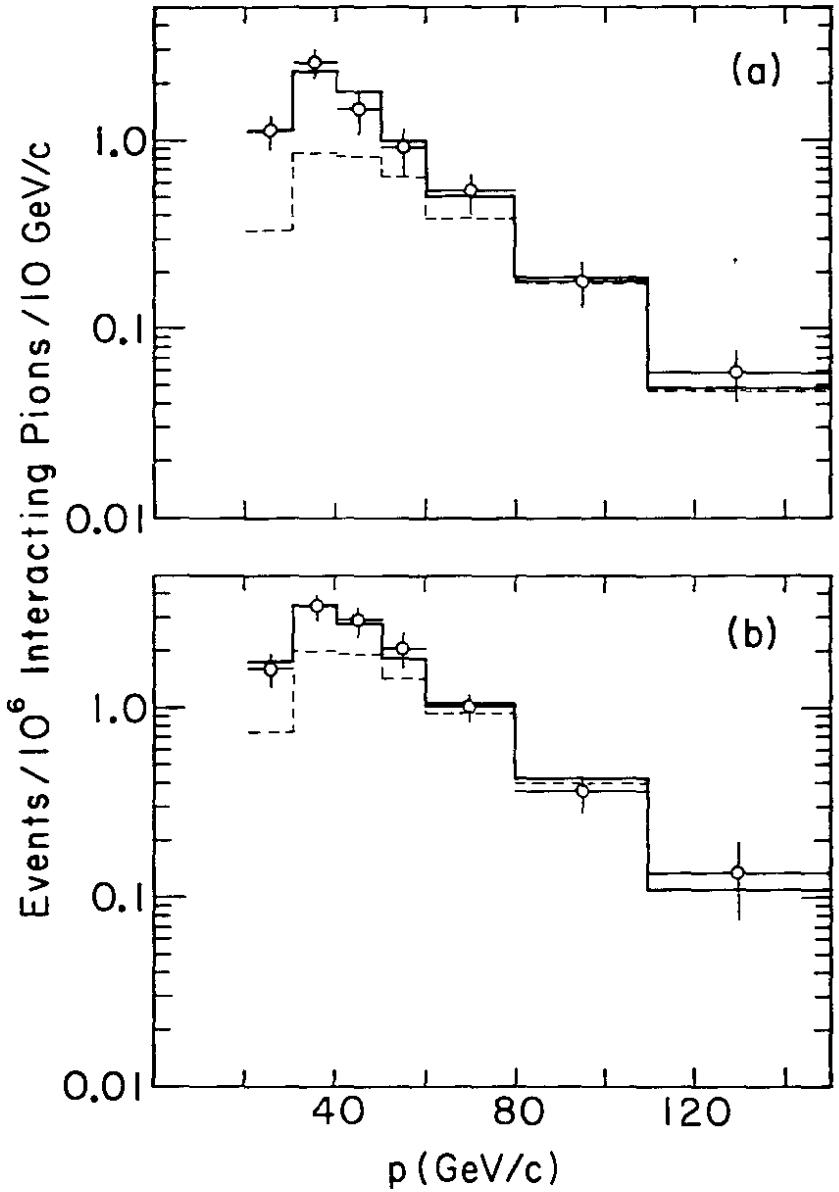

Figure 6-14: Pion prompt single muon rates versus momentum for (a) μ^+'s and (b) μ^-'s. The solid curve shows the Monte Carlo distributions from the two component fit (see text). The dotted curve shows the forward (α = .55) component only.

Finally, the allowed level for the intrinsic charm component of the pion can be obtained by assuming that all prompt single muons produced above 50 GeV/c in momentum derive from this source. This leads to the result (combining both signs and assuming $A^{2/3}$) that $B(1 - B)\sigma_{IC} = .95 \pm .07$ μb/nucleon. It is reasonable to assume B = .06. The resulting value for the maximum allowed diffractive cross section ($\sim$ 16 μb/nucleon assuming $A^{2/3}$) corresponds to an intrinsic charm component of .18%, significantly less than the predicted 1%. A lower limit on the intrinsic charm component of the pion has been determined from the study of dimuons with large missing energy from this experiment.[44]

It should be noted that the x_F distributions predicted by the intrinsic charm model are characteristic of the diffractive character of the the assumed interactions. Therefore, the above cross sections may be taken as upper limits on diffractive $D\bar{D}$ production independent of the intrinsic charm hypothesis.

6.4.2 Other Pion Experiments

The number of experiments which have observed charm production by pions is rather small. In this section, they will be briefly discussed.

One experiment[58] at Fermilab observed D^* production (with marginal statistical significance) in 200 GeV pion interactions on beryllium. The experiment triggered on the "slow" pion from the $D^* \to D\pi$ decay. In so doing, the acceptance was limited to an extremely small x_F range ($-.03 < x_F < .03$), resulting in an extremely model dependent measurement. It should be noted that in πN collisions $x_F = 0$ has no special significance. There is no natural symmetry about this point, as in pp collisions.

Another Fermilab experiment reported[59] the observation of "diffractive" $D\bar{D}$ production with 40 - 50 μb cross section in 217 GeV πp interactions. This result was reported (at a conference) in 1981 and has not yet been published. A diffractive cross section of more than about 16 μb/nucleon is ruled out by E595 (see the discussion of intrinsic charm in Section 6.4.1).

The most successful direct charm searches in pion interactions have been the CERN experiments NA16 and NA11. NA16 (LEBC-EHS) has already been discussed in the context of charm production by protons.

NA16 has reported[11] the D meson cross section to be 20^{+8}_{-4} μb for $x_F > 0$ in 360 GeV πp interactions. Using the parameterization $d^2\sigma/dx_F dp_T^2 \sim (1 - x_F)^n e^{-ap_T^2}$, they found $n = 2.8 \pm .8$ and $a = 1.1 \pm .3$. The corresponding value for a from E595 was $.70 \pm .15$.

The most intriguing result from NA16 is that the x_F distribution seems to favor two components, one with $n = 1 \pm 1$ and the other with $n = 6 \pm 3$. The "central" ($n = 6$) component accounts for about 70% of the events. This result seems to support the interpretation of the μ^- excess observed in E595 as the consequence of there being both forward (recombination) and central (non-recombination) components to charm production. In fact, all the D's observed by NA16 with $x_F > .3$ were either D^{*-}'s, D^-'s, or D^0's (all containing one of the same valence quarks as the beam π^-). No D^+'s or $\bar{D}^0$'s were observed with $x_F > .3$. The small number of observed charmed particles (10 D's and 14 $\bar{D}$'s) does not provide a strong test of the hypothesis of associated $\Lambda_c\bar{D}$ production. These first results from NA16 were statistically limited, but with more data this is a potentially powerful experiment.

NA11[60] took data with 175 and 200 GeV π^-'s on beryllium. The experiment triggered on electrons between 3 and 12 GeV/c in momentum with $p_T > .3$ GeV/c, corresponding to an acceptance for D mesons in the range

$-.2 < x_F < .2$. The experiment reconstructed the "non-triggering" D's in a forward spectrometer which had acceptance for $x_F > .2$. The cross section reported was $\sigma_{D\bar{D}} = 48 \pm 15 \pm 24$ μb/nucleon (assuming $A^{1.0}$). This experiment did not see any evidence for two components in the x_F distribution for D production, although more D° and D^- production was observed than D^+ and $\bar{D}^\circ$ production. No evidence for excess $\bar{D}$ production was observed.

Finally, NA18[61] at CERN has reported $\sigma_{D\bar{D}} = 28 \pm 11$ μb/nucleon (assuming $A^{1.0}$) in 340 GeV π^- interactions in a small bubble chamber (BIBC) filled with C_3F_8.

The general agreement between the CERN experiments and E595 on the level of the charm cross section (on a variety of targets) suggests that $A^{1.0}$ is the appropriate A-dependence for charm production by pions. The absence of any evidence for excess $\bar{D}$ production suggests that $\Lambda_c\bar{D}$ production may not be large. However, all of these experiments suffer from poor statistics. The evidence for a two component x_F distribution from NA16 is not compelling, but does lend support to this interpretation of the μ^- excess observed in E595. NA11 does not confirm this hypothesis, but it should be recalled that NA11 ran with a lepton trigger (see Section 1.2.1). The possible bias introduced by this trigger, because of correlations between the produced charmed particles, is unknown.

6.5 Summary

This thesis has described Fermilab Experiment 595, a measurement of prompt single muon production by 350 GeV protons and 278 GeV π^-'s on iron. In Chapter 1, the subject of hadronic charm production was introduced, with emphasis on experimental techniques and in particular on the "beam dump" technique. In Chapter 2, the apparatus for E595 was described. The event reconstruction was covered in Chapter 3. The analyses of the proton and pion data were described in Chapters 4 and 5, respectively. In this chapter, the prompt single muon results have been discussed within the context of hadronic charm production.

In 350 GeV proton interactions, prompt single μ^+ and μ^- production are approximately equal. The results indicate that the charm production cross section times the average semi-leptonic branching ratio is given by $B(1 - B)\sigma = 1.57 \pm .30$ μb/nucleon for $-1 < x_F < 1$. The data are well represented by $D\bar{D}$ production with $E\, d\sigma/dx_F \sim (1 - x_F)^{5.0 \pm .9}$. Charmed baryon production is allowed at the 10 μb/nucleon level. An upper limit on the charmed baryon cross section which is independent of the semi-leptonic branching ratio of charmed baryons has been calculated. Intrinsic charm appears to be ruled out by these data. Comparison to

neutrino beam dump experiments, using the same model and branching ratio assumptions, favors an $A^{1.0}$ dependence for the charm cross section. Comparison to the NA16 experiment at CERN also indicates $A^{1.0}$ dependence.

In 278 GeV π^- interactions, prompt single μ^- production is larger than prompt single μ^+ production by almost a factor of two. The source of the μ^- excess has not been firmly established. One possible explanation, which receives some support from NA16 data, is that valence quarks from the beam pion recombine with charmed quarks about 25% of the time. The x_F distribution of charmed particles produced via recombination appears to be considerably flatter than that for charmed particles produced without recombination. If this picture is correct, then the ratio of the semi-leptonic branching ratios of charged to neutral D's is greater than 1.8 (90% confidence level). The total charm cross section times the average semi-leptonic branching ratio is $B(1 - B)\sigma = 1.29^{+.40}_{-.29}$ μb/nucleon for $x_F > 0$. Comparison with other experiments favors an $A^{1.0}$ dependence of the charm cross section.

REFERENCES

1. B. J. Bjorken and S. L. Glashow, Phys. Lett. 11, 225(1964).

2. S. L. Glashow, J. Iliopoulos and L. Maini, Phys. Rev. D2, 1985(1970).

3. J. E. Augustin et al., Phys. Rev. Lett. 33, 1406(1974).

4. J. J. Aubert et al., Phys. Rev. Lett. 33, 1404(1974).

5. F. J. Hasert et al., Phys. Lett. 46B, 138(1973).

6. G. Goldhaber et al., Phys. Rev. Lett. 37, 255(1976).

7. L. M. Lederman, Phys. Rep. 26, 149(1976).

8. G. Goldhaber and J. E. Wiss, Ann. Rev. Nucl. Part. Sci. 30, 337(1980).

9. N. Ushida et al., Phys. Rev. Lett. 45, 1053(1980).
N. Ushida et al., Phys. Rev. Lett. 48, 884(1982).
N. Ushida et al., Phys. Lett. 121B, 287(1983).
N. Ushida et al., Phys. Lett. 121B, 292(1983).

10. E. Albini et al., Phys. Lett. 110B, 339(1982).

11. M. Aguilar-Benitez et al., Phys. Lett. 123B, 98(1983).

12. V. L. Fitch et al., Phys. Rev. Lett. 46, 761(1981).

13. NA32 at CERN, the ACCMOR collaboration.

14. J. Sandweiss, Physics Today 31, (Oct., 1978), p. 40.

15. K. W. Brown et al., Phys. Rev. Lett. 43, 410(1979).
K. W. B. Merritt, Caltech Ph.D. thesis, (1981), unpublished.

16. H. Abramowicz et al., Z. Phys. C13, 179(1982).

17. J. L. Ritchie, Fermilab TM-805 and TM-805A, (Aug., 1978), unpublished.

18. W. F. Baker et al., FERMILAB-78/79-EXP, (Jan., 1974), unpublished.
H. W. Atherton et al., CERN-80-07, (Aug., 1980), unpublished.
P. P. Rapidis, Proceedings of the 1981 SLAC Summer Institute (Jan., 1982), p. 641.

19. J. P. Dishaw, Stanford Ph.D. thesis (1981), unpublished.

20. J. R. Lee, Caltech Ph.D. thesis (1981), unpublished.
R. E. Blair, Caltech Ph.D. thesis (1982), unpublished.

21. J. G. Branson et al., Phys. Rev. Lett. 38, 1331(1977).

22. A. Diamant-Berger et al., Phys. Rev. Lett. 44, 507(1980).

23. R. N. Coleman et al., Phys. Rev. Lett. 44, 1313(1980).
J. P. Albanese et al., Phys. Lett. 122B, 197(1983).
J. Badier et al., Phys. Lett. 124B, 535 (1983).

24. A. Bodek et al., Phys. Lett. 113B, 82(1982).

25. C. Bebek et al., Phys. Rev. Lett. 46, 84(1981).
K. Chadwick et al., Phys. Rev. Lett. 46, 88(1981).

26. G. E. Hogan et al., Phys. Rev. Lett. 42, 948(1979).

27. F. J. Sciulli, Proceedings of the Calorimeter Workshop, Fermilab (1975), edited by M. Atac, p. 79.
U. Amaldi, Physica Scripta 23, 409(1981).

28. E. Anassontzis, FERMILAB-CONF-82/50-EXP, (July, 1982); B. Cox, Proceedings of the 21st Int. Conf. on High Energy Physics, edited by P. Petiau and M. Porneuf (Paris, 1982), p. C3-140.

29. B. L. Combridge, Nucl. Phys. B151, 429(1979).

30. B. L. Combridge, RL-82-027, (March, 1982), presented at Morionde Workshop on New Flavors, Les Arcs, 1982.

31. R. Winder and C. Michael, Nucl. Phys. B173, 59(1980).

32. B. Andersson, H.-U. Bengtsson and G. Gustafson, LU TP 83-4, (March, 1983).

33. V. Barger, F. Halzen and W. Y. Keung, Phys. Rev. D24, 1428(1981).

34. S. J. Brodsky, C. Peterson and N. Sakai, Phys. Rev. D23, 2745(1981).

35. W. Bacino et al., Phys. Rev. Lett. 43, 1073(1979).

36. W. Wilson, Phys. Rev. D17, 3032(1978).

37. C. E. Carlson and R. Suaya, Phys. Lett. 81B, 329(1979).

38. A. S. Carroll et al., Phys. Lett. 80B, 319(1979).

39. M. E. Nelson et al., SLAC-PUB-3059 (LBL-15733), (Feb., 1983), submitted to Phys. Rev. Lett.

40. R. Blankenbecler and S. J. Brodsky, Phys. Rev. D10, 2973(1974).

41. E. Vella et al., Phys. Rev. Lett. 48, 1515(1982).

42. G. Bertsch et al., Phys. Rev. Lett. 47, 297(1981).

43. J. J. Aubert et al., Phys. Lett. 110B, 73(1982).

44. A. Bodek et al., Phys. Lett. 113B, 77(1982).

45. P. Alibran et al., Phys. Lett. 74B, 134(1978).
T. Hansl et al., Phys. Lett. 74B, 139(1978).
P. C. Bosetti et al., Phys. Lett. 74B, 143(1978).

46. M. Jonker et al., Phys. Lett 96B, 435(1980).

47. P. Fritze et al., Phys. Lett. 96B, 427(1980).

48. R. C. Ball et al., Phys. Rev. Lett. 51, 743(1983).

49. R. C. Ball et al., UMHE-82-06 and Proceedings of 1982 Morionde Workshop on New Flavors, (Les Arcs, 1982), p. 393.

50. R. C. Ball et al., submitted paper to 21st Internation Conference on High Energy Physics, (Paris, 1982);
see R. C. Ball et al., Proceedings on Neutrino ´82, (Balatonfured, Hungary, 1982), Vol. 1, p. 89.

51. R. C. Ball et al., Invited Talk at the 1982 DPF Meeting (College Park, Maryland, Oct., 1982), presented by M. J. Longo.

52. R. C. Ball et al., UMHE-83-09 (May, 1983), to be published in the Proceedings of the 18th Rencontre de Moriond (La Plagne, 1983).

53. R. C. Ball et al., UMHE 83-13, (July, 1983), submitted paper to 22nd Int. Conf. on High Energy Physics (Ithaca, 1983).

54. A. N. Aleev et al., JINR-E1-82-759, (Nov., 1982), unpublished.
T. Aziz et al., Nucl. Phys B199, 424(1982).
S. F. Biagi et al., Phys. Lett 122B, 455(1982).

55. M. Aguilar-Benitez, Phys. Lett. 123B, 103(1983).

56. K. L. Giboni et al., Phys. Lett. 85B, 437(1979).
W. Lockman et al., Phys. Lett. 85B, 443(1979).
D. Drijard et al., Phys. Lett. 85B, 452(1979).
D. Drijard et al., Phys. Lett. 81B, 250(1979).
M. Basile et al., Nuovo Cimento 63A, 230(1981).

57. R. Odorico, Nucl. Phys. B209, 77(1982).

58. V. L. Fitch, Phys. Rev. Lett. 46, 761(1981).

59. J. Cooper, Proceedings of the 16th Rencontre de Moriond, edited by J. Thran Thanh Van (1981), p. 113;
see also L. J. Koestler et al., Proceedings of the 20th Int. Conf. on High Energy Physics, edited by L. Durand and L. Pondrom (Madison, 1980), p. 190.

60. R. Bailey et al., CERN-EP/83-83 (June, 1983), submitted to Phys. Lett.
R. Bailey et al., CERN-EP/83-84 (June, 1983), submitted to Phys. Lett.

61. A. Bardetscher et al., Paper 789 submitted to 21st Int. Conf. on High Energy Physics, (Paris, 1982).

62. Y.-S. Tsai, Rev. Mod. Phys. 46, 815(1974); erratum Rev. Mod. Phys. 49 (1977).

63. F. E. Taylor et al., Phys. Rev. D14, 1217(1976).

64. T. Ferbel, Proceedings of the 19th Int. Conf. on High Energy Physics (Tokyo, 1978), p. 465.

65. D. S. Barton, Phys. Rev. D27, 2580(1983).

66. U. Amaldi, M. Jacob and G. Matthiae, Ann. Rev. Nucl. Part. Sci. 26, 385(1976).

67. Private communication M. Zielinski and T. Ferbel; see M. Zielinski et al., Z. Phys C16, 197(1983).

68. Bruno Rossi, High Energy Particles (Prentice-Hall, Inc., 1952); Sect. 2.3, eq. 6; Sect. 2.14, eq. 4; Sect. 2.20, eqs. 6c and 6d.

69. D. O. Caldwell et al., Phys. Rev. Lett. 42, 554(1979).

70. A. Bodek et al., Phys. Rev. D20, 1471(1979).

APPENDIX 1

DIMUON MONTE CARLO

Highly asymmetric dimuons constituted a background to the prompt single muon measurement. In particular, those dimuons with one muon of momentum less than about 5.2 GeV/c were classified as single muon events. This background was removed with the aid of a Monte Carlo calculation. In this appendix the dimuon Monte Carlo is described and its predictions are compared to the observed dimuon distributions.

Data were taken with both a 350 GeV/c proton beam and a negative 278 GeV/c pion beam, and as a consequence, dimuon production with these two different beams had to be treated separately. In particular, cross sections and production distributions (versus Feynman x and p_T) of the various sources of dimuons, as well as the energy dependence of the cross sections, are different for the two beams. However, in both cases, the method used was the same and only parameters were changed. Production of

dimuons by the re-interaction of secondary hadrons (i.e., those produced in the primary collisions) was also included in the dimuon generation. Tertiary production was included for the proton case, but was found to be negligible for pions.

Dimuons were treated as originating from one of two types of sources: the resonances (ρ, ω, ϕ, ψ, and ψ') and the continuum regions stretching from the dimuon threshold ($2m_\mu$ = .211 GeV) all the way up to the ψ. In fact, no source of dimuons of mass greater than about 2 GeV is important here. The low mass sources dominate.

The production parameters, which included cross sections and Feynman x and p_T distributions, were estimated initially from Reference 21. Unfortunately, these measurements were conducted at different energies and on different target nuclei than this experiment. It was found that some adjustment of parameters was necessary in order for the Monte Carlo predictions to fit the dimuon distributions measured in this experiment.

The Bethe-Heitler production of muon pairs from the interactions of photons (from neutral pion decays) with the target nuclei was also included in the Monte Carlo. The Bethe-Heitler cross sections and distributions were taken from the calculation of Tsai.[62]

It was found that, in the case of 350 GeV protons on target, 72% of triggering dimuons were from the primary

collision, 18% were from the interactions of secondary and tertiary hadrons, and 10% were from the Bethe-Heitler mechanism. In the case of 278 GeV negative pions, 82% were from the primary collision, 7% were from the interactions of secondaries, and 11% were from Bethe-Heitler production.

After the production of the parent particle and its subsequent decay to a $\mu^+\mu^-$ pair, each muon was traced through the apparatus. The effects of multiple Coulomb scattering and dE/dx losses on the muon trajectories were included. For each event in which a muon penetrated the counters necessary to satisfy the high-p trigger, a record was written to tape. This record was in the same format as the raw data and contained spark positions and scintillation counter data (i.e., bits were set and minimum ionizing pulse heights, without fluctuations, were recorded for those counters through which a muon passed). This "Monte Carlo data" was then passed through the same reconstruction and analysis programs as the real data.

The Monte Carlo results are compared to the data in Figures A1-1 through A1-6 for the proton data and Figures A1-7 through A1-12 for the pion data. These comparisons were restricted to events in which the momenta of both muons were measured in the toroid spectrometer. This corresponds to a minimum momentum requirement of around

12 GeV/c for the lower momentum muon. A single normalization factor (.91 for protons and .94 for pions) was applied to the Monte Carlo in order to facilitate a comparison of the shapes of distributions. No plots have been normalized separately. The statistical errors on the data are not shown in the figures since they are substantially smaller than the statistical errors on the Monte Carlo, which are shown. Larger Monte Carlo statistics were not justified because the dominant sources of error in the prompt single muon rates were the errors from the density extrapolations rather than the dimuon subtraction.

As described in Section 4.2.3, the dimuon Monte Carlo was used to calculate the ratio of unobserved to observed dimuons versus the momentum, and also versus the transverse momentum, of the triggering muon. These ratios are shown in Figure A1-13 for the proton data and Figure A1-14 for the pion data. The errors shown are considered to be reasonable estimates of the uncertainty in these ratios arising from uncertainties in the details of dimuon production (i.e., uncertainties in the parameters used in the Monte Carlo). This view was arrived at by comparing the ratios calculated with different sets of parameters which also gave reasonable agreement between data and Monte Carlo.

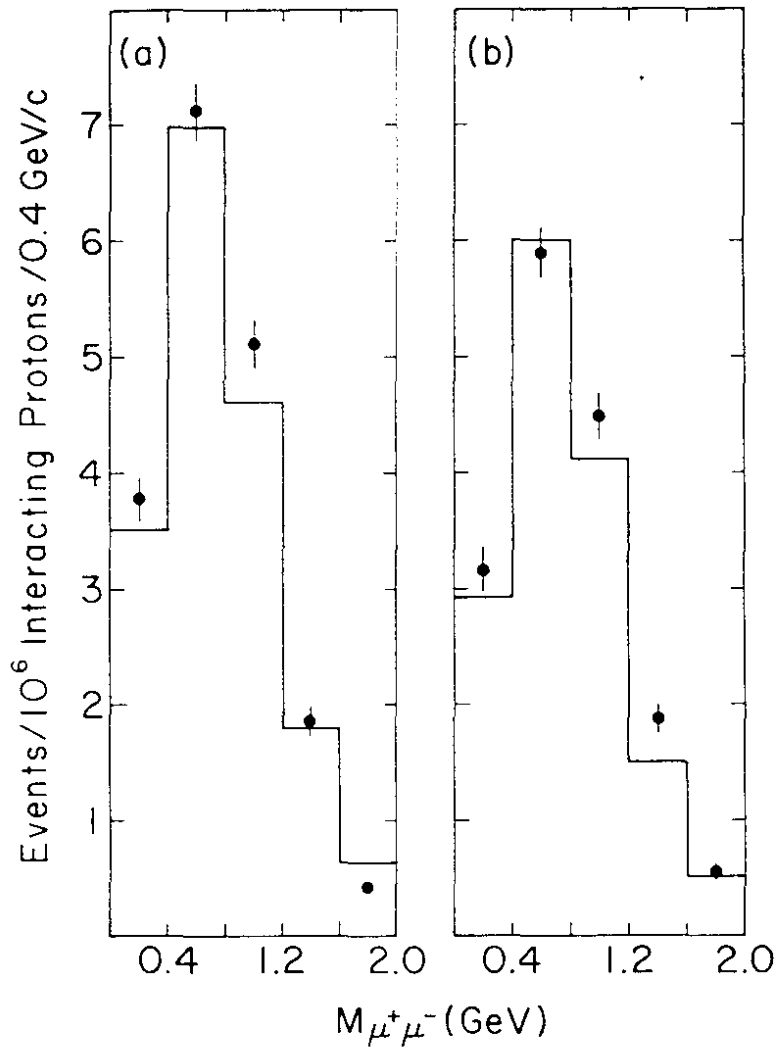

Figure A1-1: Dimuon mass for proton data. Solid lines are data and dots are Monte Carlo for: (a) events with a triggering μ^+ and (b) events with a triggering μ^-.

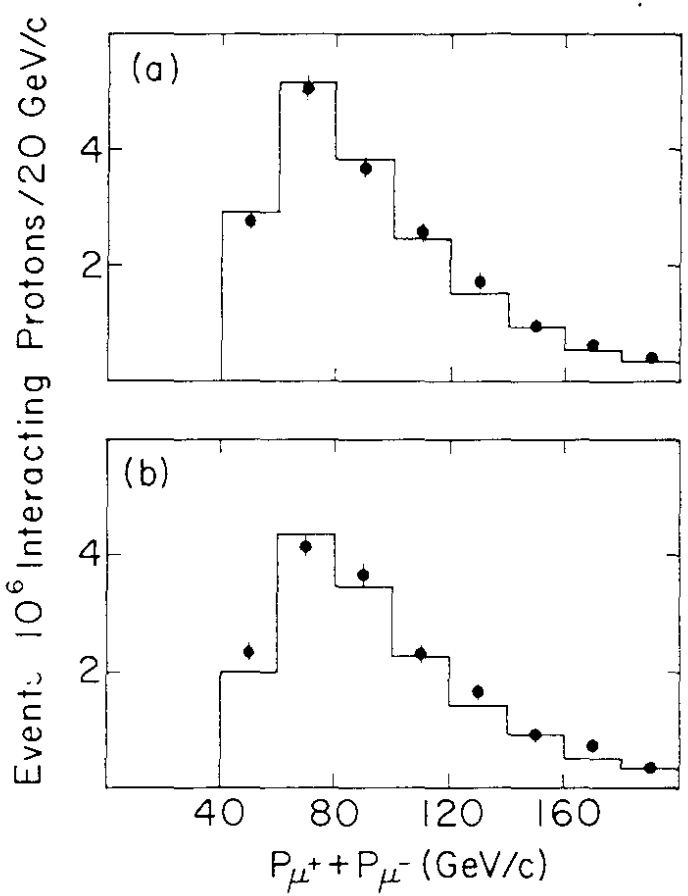

Figure A1-2: Sum of muon momenta for proton data. Solid lines are data and dots are Monte Carlo for: (a) events with a triggering μ^+ and (b) events with a triggering μ^-.

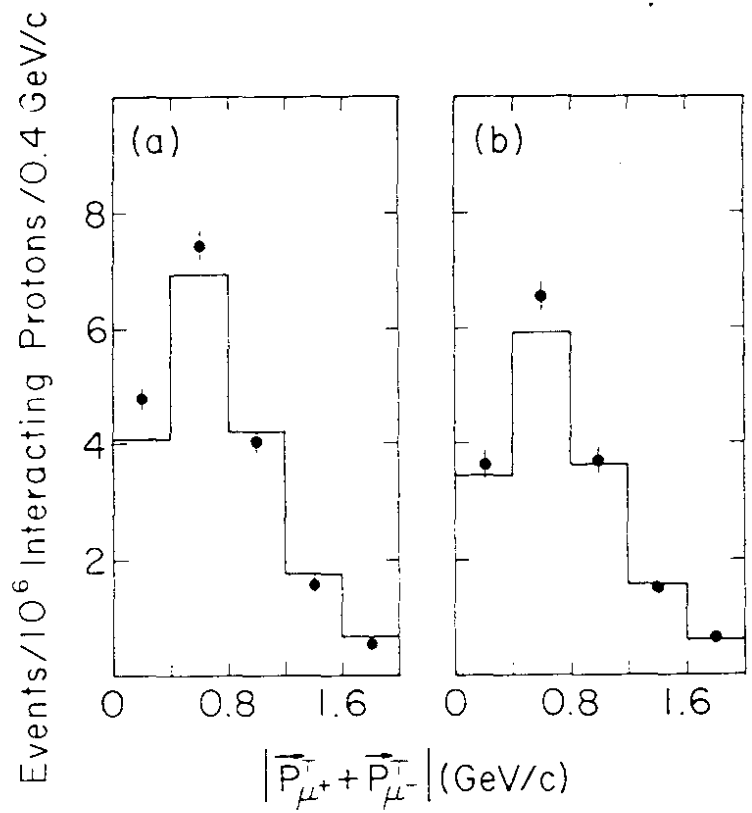

Figure A1-3: Pair transverse momentum for proton data. Solid lines are data and dots are Monte Carlo for: (a) events with a triggering μ^+ and (b) events with a triggering μ^-.

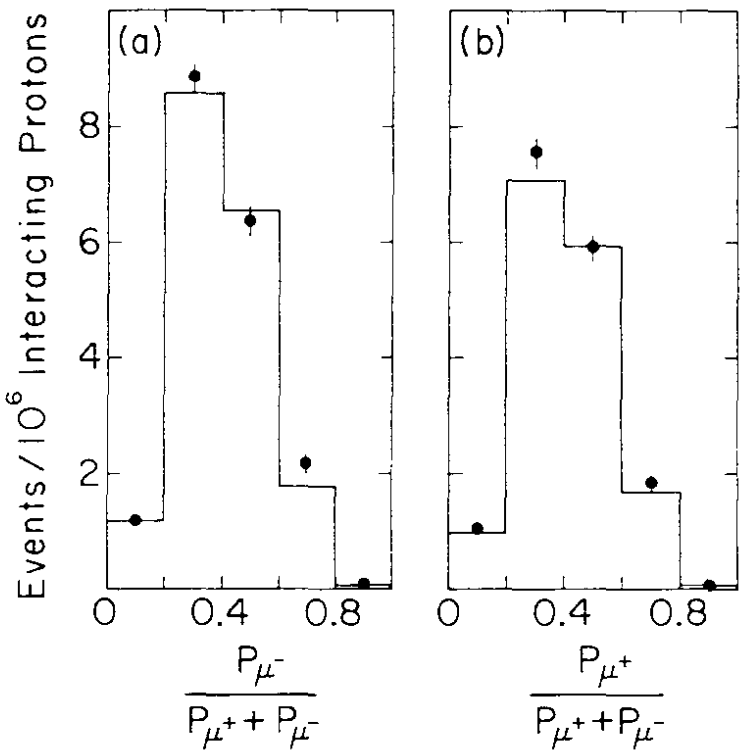

Figure A1-4: Momentum of non-triggering muon divided by the sum of dimuon momenta for proton data. Solid lines are data and dots are Monte Carlo for: (a) events with a triggering μ^+ and (b) events with a triggering μ^-.

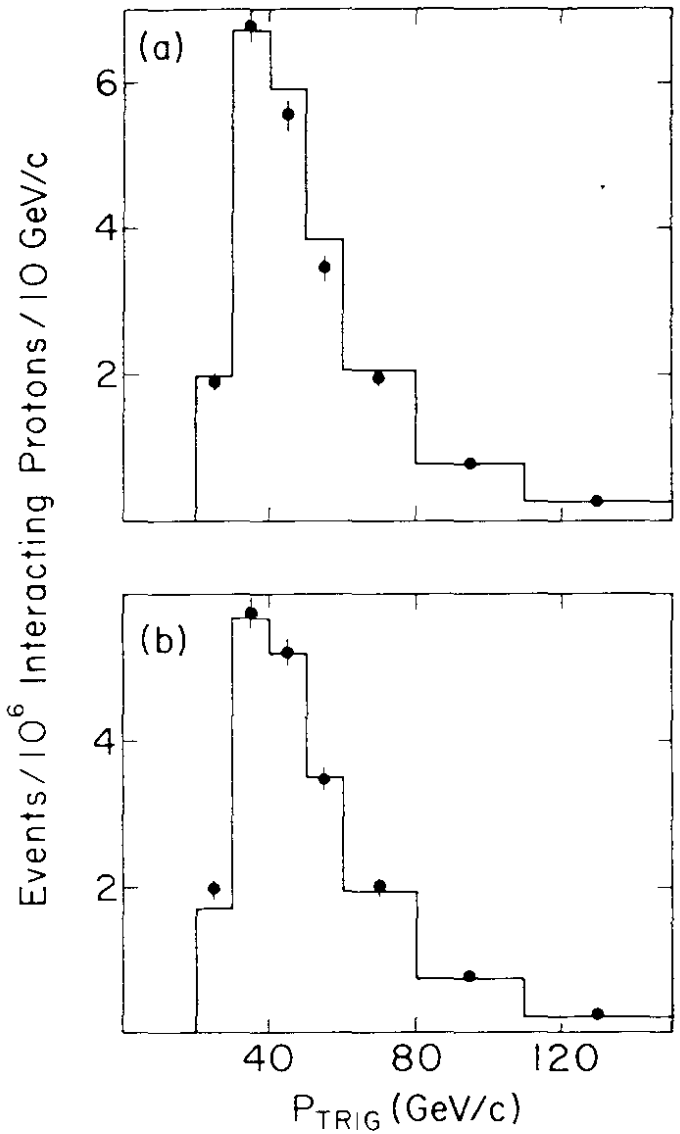

Figure A1-5: Momentum of triggering muon for proton data. Solid lines are data and dots are Monte Carlo for: (a) events with a triggering μ^+ and (b) events with a triggering μ^-.

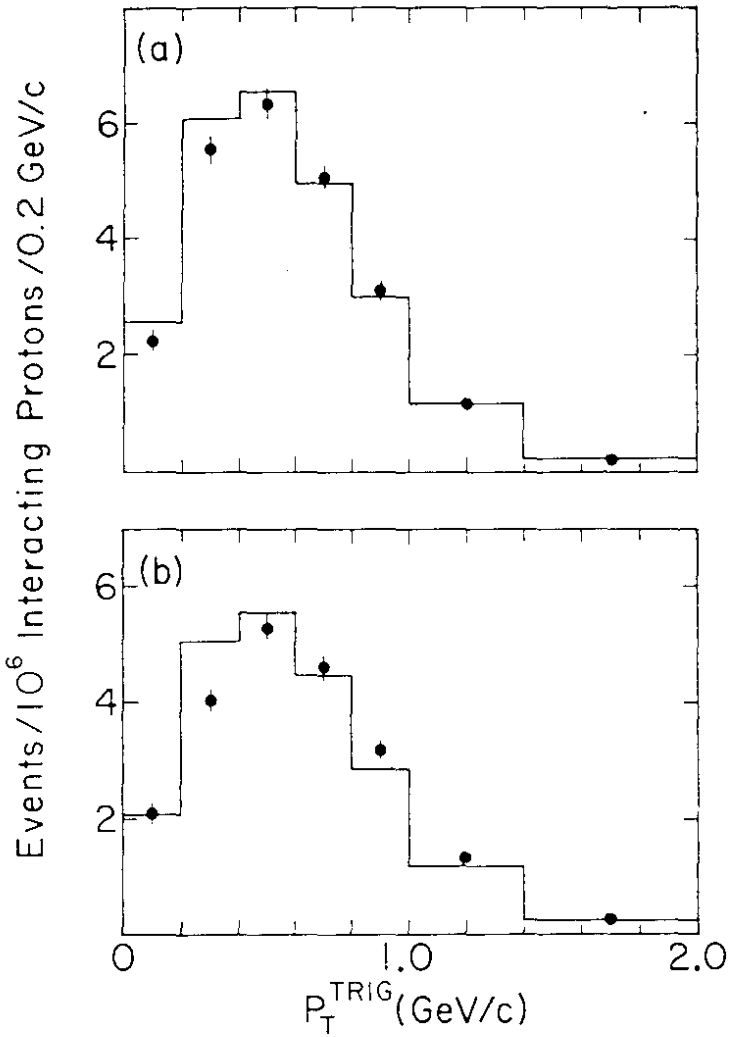

Figure A1-6: Transverse momentum of triggering muon for proton data. Solid lines are data and dots are Monte Carlo for: (a) events with a triggering μ^+ and (b) events with a triggering μ^-.

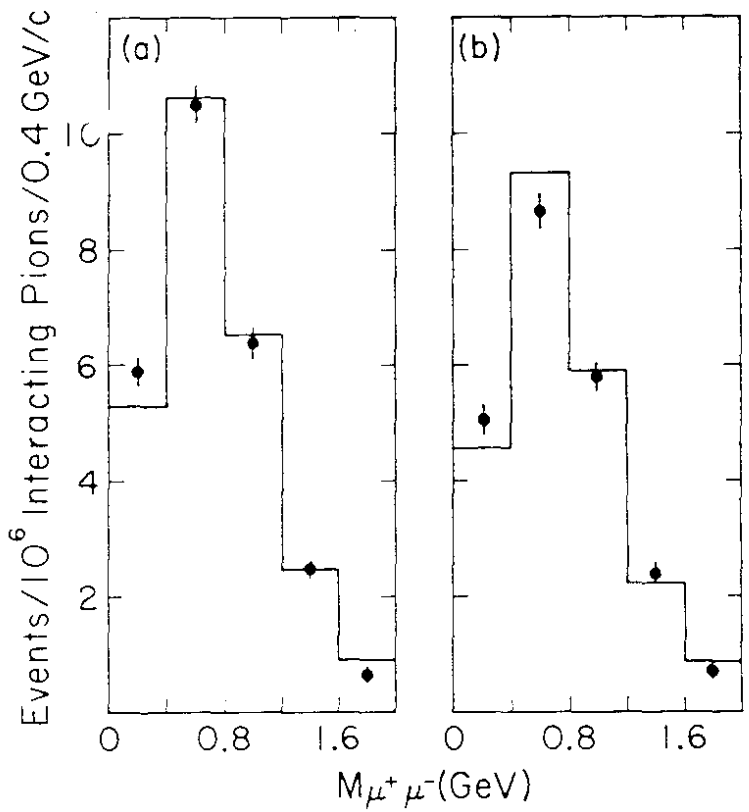

Figure A1-7: Dimuon mass for pion data. Solid lines are data and dots are Monte Carlo for: (a) events with a triggering μ^+ and (b) events with a triggering μ^-.

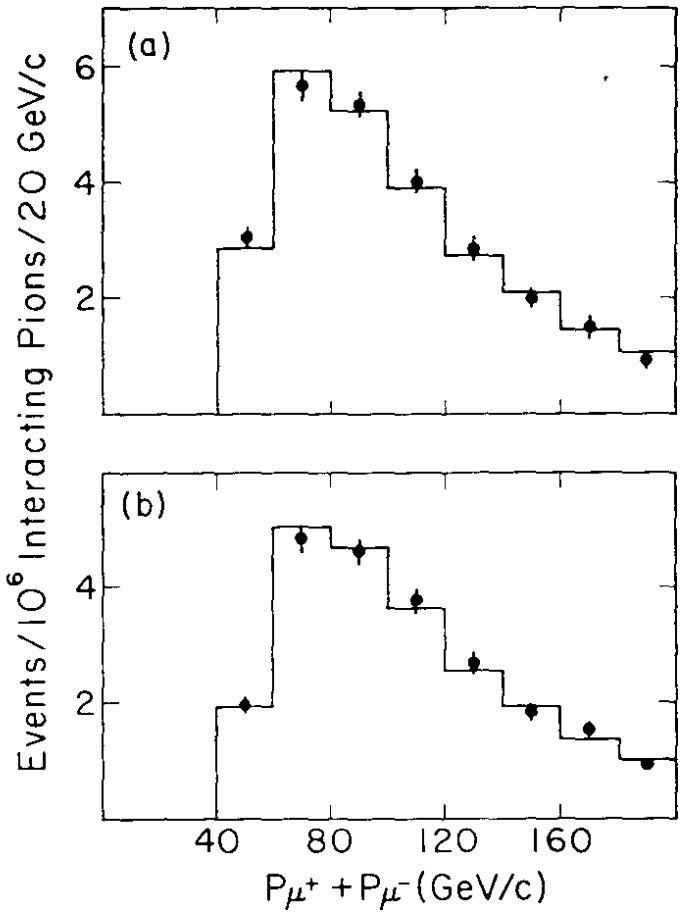

Figure A1-8: Sum of muon momenta for pion data. Solid lines are data and dots are Monte Carlo for: (a) events with a triggering μ^+ and (b) events with a triggering μ^-.

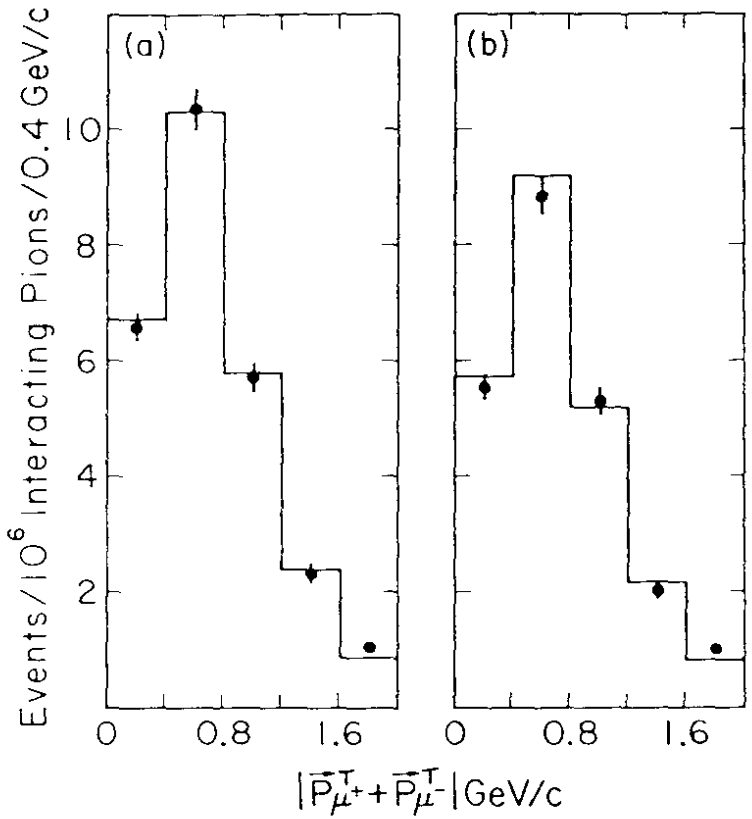

Figure A1-9: Pair transverse momentum for pion data. Solid lines are data and dots are Monte Carlo for: (a) events with a triggering μ^+ and (b) events with a triggering μ^-.

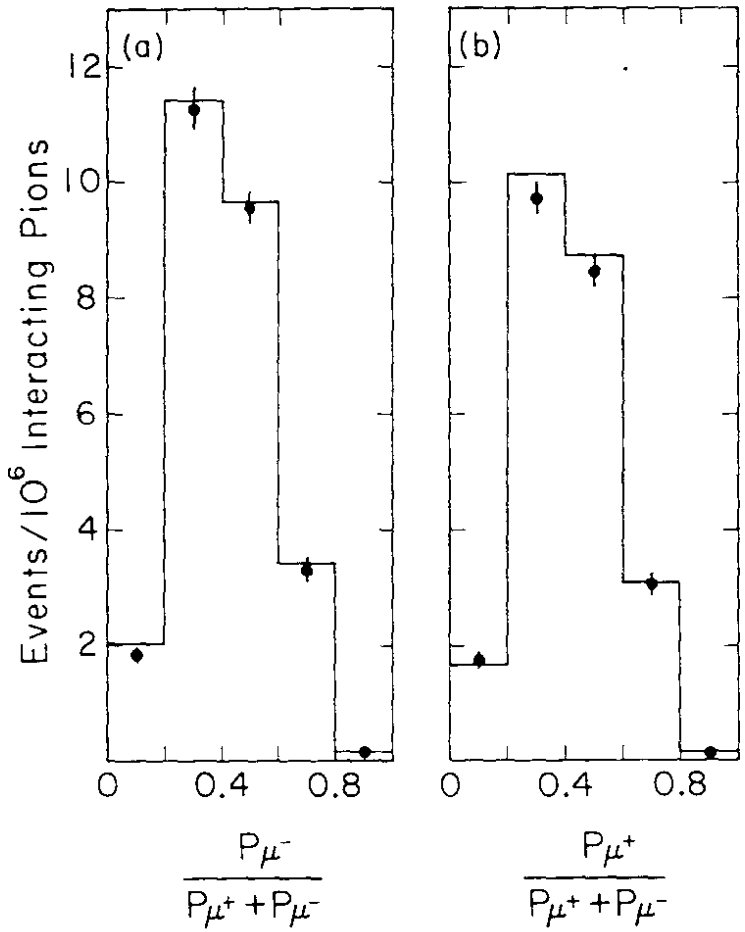

Figure A1-10: Momentum of non-triggering muon divided by the sum of dimuon momenta for pion data. Solid lines are data and dots are Monte Carlo for: (a) events with a triggering μ^+ and (b) events with a triggering μ^-.

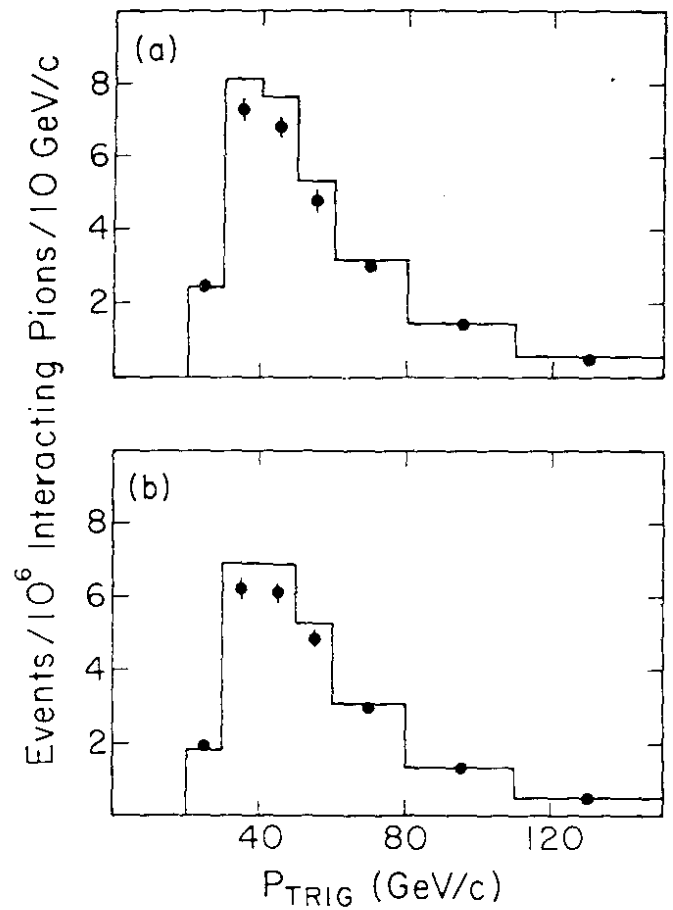

Figure A1-11: Momentum of triggering muon for pion data. Solid lines are data and dots are Monte Carlo for: (a) events with a triggering μ^+ and (b) events with a triggering μ^-.

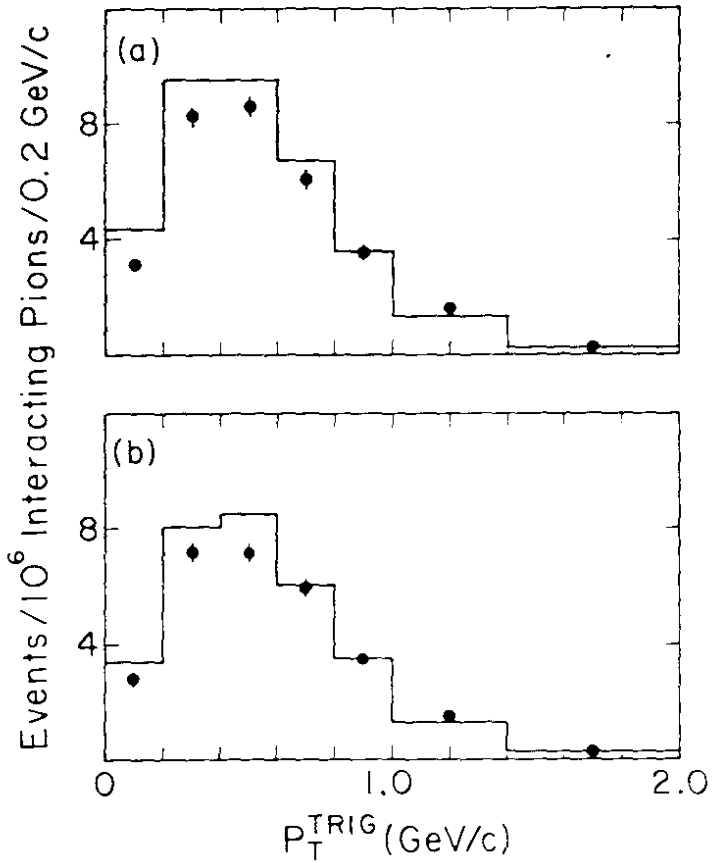

Figure A1-12: Transverse momentum of triggering muon for pion data. Solid lines are data and dots are Monte Carlo for: (a) events with a triggering μ^+ and (b) events with a triggering μ^-.

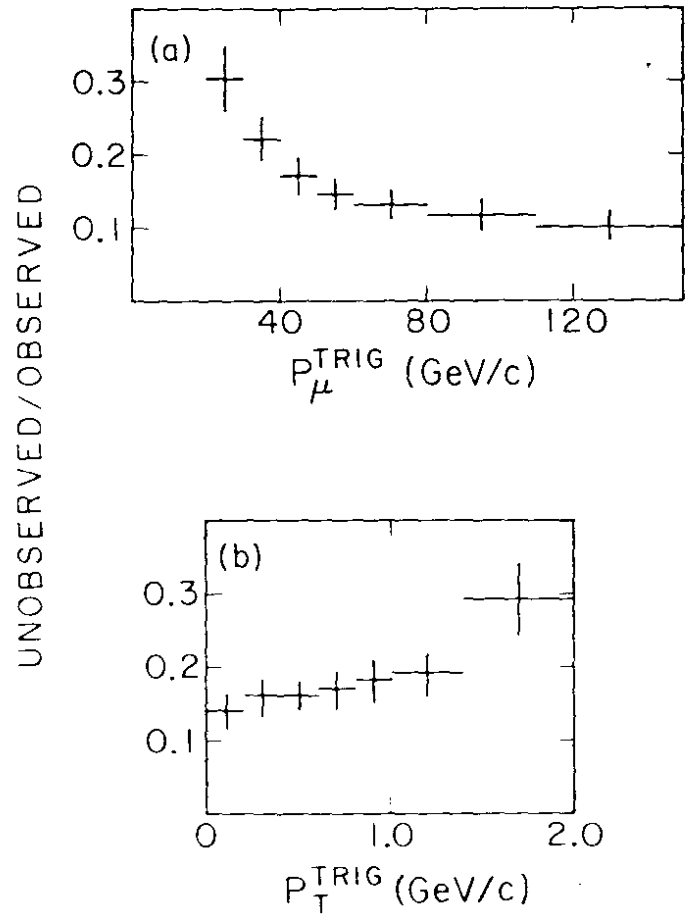

Figure A1-13: Calculated ratio of unobserved to observed dimuons versus (a) momentum and (b) transverse momentum of triggering muons for proton induced high-p triggers.

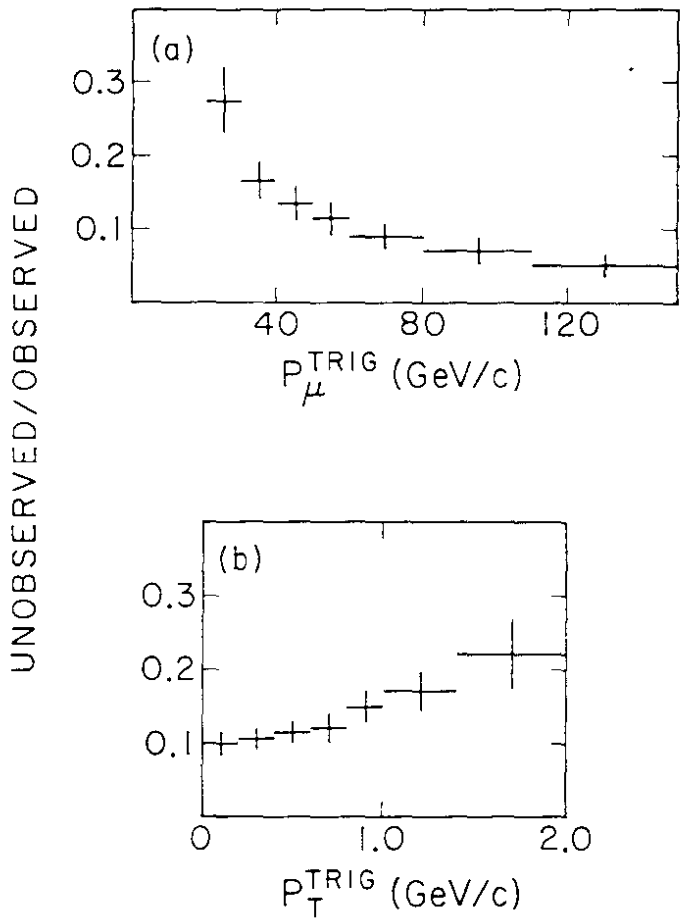

Figure A1-14: Calculated ratio of unobserved to observed dimuons versus (a) momentum and (b) transverse momentum of triggering muons for pion induced high-p triggers.

APPENDIX 2

CALCULATION OF DOWNSTREAM DECAY RATES

The term "downstream decays" refers to muons produced in pion and kaon decays in the far downstream region of the target-calorimeter or in the gap between the end of the target-calorimeter and the muon identifier. The effective density of the downstream part of the target-calo· meter (after 1.7 meters of steel, 10 proton interaction lengths) was the same for the COMPACTED, SEMI-EXPANDED, and EXPANDED configurations of the target-calorimeter. As a consequence, muons produced in this region would appear to be prompt. Muons produced in the gap (after 2.4 meters of steel) would also contribute a false prompt signal. The rate for such muons was quite small, indeed unmeasurably small (see Section 4.2.5). A Monte Carlo calculation was therefore performed to estimate this background.

The Monte Carlo program included the production of pions by protons and pions and the production of kaons by protons and kaons. The generation of these particles

employed a radial scaling parameterization of particle production data on hydrogen from Reference 63, modified to include A-dependent effects. In particular, an approximate representation of data summarized in Reference 64 has been used:

$(dN/dx_F)_A/(dN/dx_F)_H = A^{B(x_F) - .7}$, where

$B(x_F) = .45 + .40(1 - x_F)^{2.5}$ for $x_F > 0$, and p_T distributions have been modified by a factor of $A^{.23p_T}$.

For this calculation, production of muons by pion and kaon decays was simulated by following the hadronic cascade for six generations. It was concluded from the contribution of each generation to the downstream decay rate that additional generations could account for no more than an additional 10%.

For the proton data, the Monte Carlo overestimated the non-prompt μ^+ rate by 10% and the non-prompt μ^- rate by 50%. For the pion data, it was necessary to augment the Monte Carlo calculation with additional information on particle production from Reference 65. This was because the Monte Carlo did not generate kaons produced in pion interations. The calculation overestimated the pion induced non-prompt rates by 30% for μ^- and by 20% for μ^+.

The method of the downstream decay calculation was to generate pions (or kaons) belonging to a given generation of the hadronic cascade, keeping track of position in the

target-calorimeter and all other relevant variables. The pions were then allowed to decay to muons which were traced through the apparatus (including dE/dx and multiple Coulomb scattering) to determine which muons would trigger. For muons which triggered, the probability that the decay occured in each of three regions, the expanded region, the unexpanded region, and the gap, was calculated. For a pion of known position and momentum, this calculation is effectively exact. Sums were incremented for these three quantities. The trigger rate for decays in these three regions was just the sums of the probabilities divided by the number of incoming beam particles.

The rates were calculated in bins versus muon momentum. For each bin, the ratio of the unexpanded rate plus twice the gap rate (see Section 4.2.5) to the rate for the expanded region was calculated. The downstream decay rate (for each bin) was taken to be this ratio times the non-prompt rate measured from the density extrapolation (for that bin). The calculated downstream decay rate versus momentum for the proton data was shown in Figure 4-9 (page 132). The calculated rates were subtracted from the raw prompt rates. A 100% systematic error was assumed. The subtraction did not exceed 3% of the prompt single muon rates for either data set.

APPENDIX 3

NONUNIFORM CALORIMETER DENSITY

An error in the density extrapolation comes about because the "dump" is not a uniform medium, but rather a series of alternating dense plates and air gaps. The error is small as long as the plate thickness is small compared to the interaction length in the material (iron in this case). A correction for this effect has been applied in this experiment. The correction is derived below.

Consider a beam dump with plate thickness ℓ and distance g between the plates (this dump will be taken to be infinitely long; the effect of finite length, downstream decays, has been discussed elsewhere). Let X measure the distance in steel from the front of the dump and let λ represent the interaction length (taken for simplicity to be the same for protons and pions). In the following, no attention will be paid to momentum; the calculation may be thought of as performed at fixed p, so the result may be applied in p bins. Suppose that N_{pr} protons are incident upon the dump and in each proton

interaction N_π pions are produced. The number of pions produced between X_1 and $X_1 + dx_1$ is

$$N_{pr} N_\pi e^{-x_1/\lambda} \frac{dx_1}{\lambda} .$$

The probability that a pion produced at X_1 will survive to reach X_2 is given by

$$e^{-\frac{X_2 - X_1}{\Lambda}} , \quad \Lambda = \frac{\lambda c\tau\gamma\beta}{\lambda + c\tau\gamma\beta} .$$

The quantity Λ is neglibibly different from λ because $c\tau\gamma\beta$ is enormous compared to λ ($c\tau\gamma\beta$ has the usual meaning; see Chapter 1). Therefore, the number of pions at position X_2 is given by

$$N_{pr} N_\pi \int_0^{X_2} e^{-X_1/\lambda} e^{-\frac{X_2 - X_1}{\lambda}} \frac{dx_1}{\lambda} = N_{pr} N_\pi \frac{X_2}{\lambda} e^{-X_2/\lambda} .$$

The number of pions which decay <u>in steel</u> is

$$N^d_{steel} = N_{pr} N_\pi \int_0^\infty \frac{X_2}{\lambda} e^{-X_2/\lambda} \frac{dx_2}{c\tau\gamma\beta} = N_{pr} N_\pi \frac{\lambda}{c\tau\gamma\beta} .$$

The number of pions which decay <u>in air</u> is

$$\begin{aligned} N^d_{air} &= \left(\frac{g}{c\tau\gamma\beta}\right) \sum_{n=1}^{\infty} N_{pr} N_\pi \frac{n\ell}{\lambda} e^{-n\ell/\lambda} \\ &= N_{pr} N_\pi \frac{g\ell}{\lambda c\tau\gamma\beta} \sum_{n=1}^{\infty} n \left(e^{-\ell/\lambda}\right)^n \\ &= N_{pr} N_\pi \frac{g\ell}{\lambda c\tau\gamma\beta} \left[\frac{e^{-\ell/\lambda}}{(1 - e^{-\ell/\lambda})^2}\right] . \end{aligned}$$

The term in brackets can be expanded in powers of $\frac{\ell}{\lambda}$.

Then

$$N^d_{air} \cong N_{pr} N_\pi \frac{g\ell}{\lambda c \tau \gamma \beta} \left[\left(\frac{\lambda}{\ell}\right)^2 \left(1 - \frac{1}{12}\left(\frac{\ell}{\lambda}\right)^2\right)\right].$$

Hence, the total number of decays (steel + air) is

$$N^d_{steel} + N^d_{air} = N_{pr} N_\pi \frac{\lambda}{c\tau\gamma\beta}\left[1 + \frac{g}{\ell}\left(1 - \frac{1}{12}\left(\frac{\ell}{\lambda}\right)^2\right)\right].$$

Now, the number of decays per incident proton, times the appropriate branching ratio, can be identified with the non-prompt rate R_{np}. Therefore,

$$R_{np} \propto 1 + \frac{g}{\ell}\left[1 - \frac{1}{12}\left(\frac{\ell}{\lambda}\right)^2\right] .$$

But note that $\frac{g+\ell}{\ell} = \frac{\rho_{Fe}}{\rho}$, where ρ is the average density. Then, with some manipulation,

$$R_{np} \propto \frac{\rho_{Fe}}{\rho}\left[1 - \frac{1}{12}\left(\frac{\ell}{\lambda}\right)^2\right] + \frac{1}{12}\left(\frac{\ell}{\lambda}\right)^2 .$$

Since $\frac{1}{12}\left(\frac{\ell}{\lambda}\right)^2 \approx 10^{-4}$ for the appropriate choices of ℓ and λ, the constant of proportionality is the non-prompt rate at $\rho = \rho_{Fe}$. Thus, the false prompt signal at $1/\rho = 0$ is given by

$$\frac{1}{12}\left(\frac{\ell}{\lambda}\right)^2 R_{np}(\rho = \rho_{Fe}) .$$

Note that, strictly speaking, this calculation has only treated first generation pions, while the measured non-prompt rate includes all generations.

APPENDIX 4

CALCULATION OF INTERACTING MUON RATES

A muon interaction in the target-calorimeter could satisfy the high-p trigger if the energy lost exceeded about 30 GeV. About half of such triggers were rejected by the PWC cuts on track quality and momentum. The remaining half had to be removed by other means. In Section 5.1.2, a procedure of performing fits to shower length distributions was described which was used to subtract most ($\sim$ 90%) of the remaining interacting muons (those with purely electromagnetic showers). In this appendix, interacting muon events are discussed in detail and a final subtraction for those that remained after the shower length subtraction is calculated.

There are four processes by which muon interactions could lead to single muon final states:

$$\mu^- + Fe \rightarrow \mu^- + Fe + \gamma \text{ (bremsstrahlung)},$$

$$\mu^- + Fe \rightarrow \mu^- + Fe + e^+ + e^- \text{ (pair production)},$$

$$\mu^- + e^- \rightarrow \mu^- + e^- \text{ (knock-on electrons), and}$$

$$\mu^- + Fe \rightarrow \mu^- + \text{hadrons (inelastic scattering)}.$$

The cross sections per nucleus for these processes for 278 GeV/c muons on iron are shown in Figure A4-1, plotted versus the quantity y, sometimes called the "inelasticity" and given by $y = E_{lost}/E_{initial}$. The calculation of $d\sigma/dy$ is described in Appendix 5. Note the rapid decrease in cross section with increasing y, implying that most muon interactions will yield very high momentum muons, a property that was noted from the data in Section 5.1.2. Also note that the first three processes, those which produce purely electromagnetic showers, account for about 90% of the total cross section in the region of high y, which is of interest (the region where pion induced prompt single muon events reside).

Two problems prevent an a priori calculation, using the cross sections shown in Figure A4-1, of the interacting muon rates i.e., the number of interacting

muons per IBV). The first is that the number of muons surviving the PWC cuts is unknown. This number depended on the precise running conditions under which data were taken (collimator positions, for example), which were functions of target-calorimeter configuration, beam intensity and quality, and potentially other factors. A proper measurement of this quantity would have required a prescaled "muon trigger," to which analysis cuts could be applied to determine their effects.

The second problem is that details of the calorimeter response affected the rate. The trigger required the

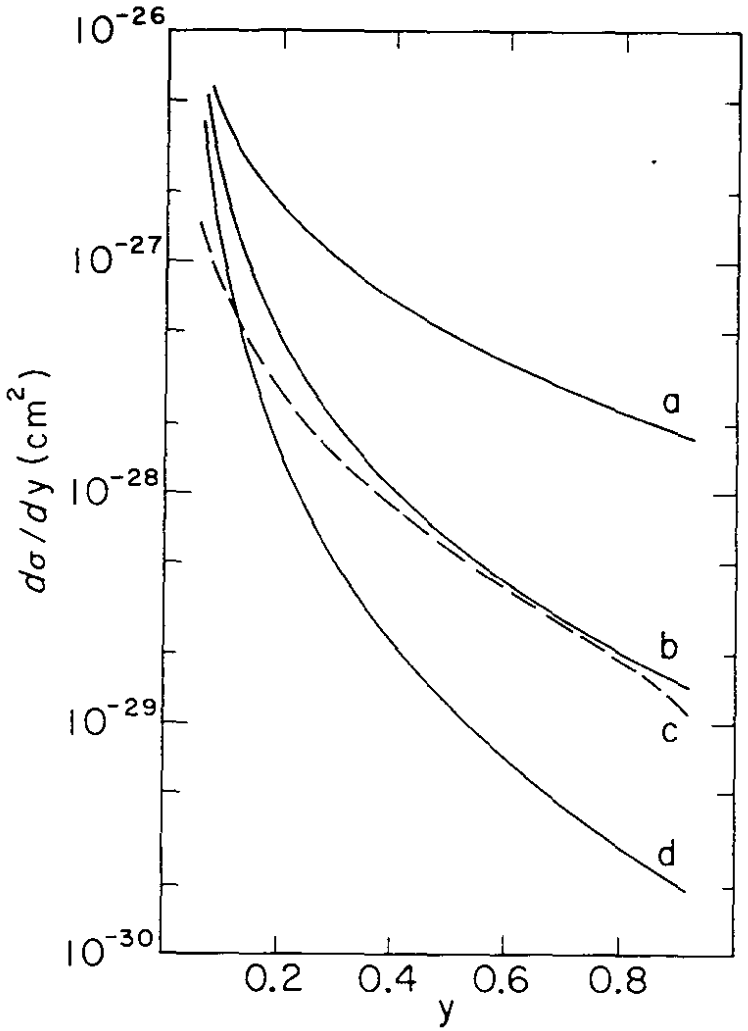

Figure A4-1: $d\sigma/dy$ per nucleus versus y for 278 GeV/c muons to interact in iron by the processes: (a) bremsstrahlung, (b) knock-on electron production, (c) inelastic scattering (which produces hadrons), and (d) direct e^+e^- pair production.

hardware sum of the first 40 calorimetry counters (ESUM) to exceed roughly 30 GeV, and at the same time, the sum of the fourth through the eleventh calorimetry counters to exceed about 5 GeV (E4-11). (For a complete description of the trigger, see Section 2.3) As a result, the energy threshold for muon interactions depended upon the longitudinal position of the interactions. Uncertainties relating to this could introduce significant systematic errors into any calculation. Also, the energy calibration for purely electromagnetic showers is expected to differ from that of hadronic showers at the 10% to 30% level and this was never measured (i.e., data were never taken with an electron beam).

It is possible, however, to make an estimate of the interacting muon rates independently of the shower length fits. The procedure for doing this is straightforward, but rather involved, and will be described below. The results of this procedure can be compared to the results from the shower length method. Unfortunately, this comparison is complicated by the presence of events besides interacting muons which give triggering μ^-'s along with purely electromagnetic showers in the target-calorimeter. Such events will have short showers and will be included with interacting muons by the fitting method. Therefore, they must be taken into

account in any comparisons.

Three sources of purely electromagnetic showers (which also provide a triggering muon) are: (1) interacting muons, (2) the decays $\pi^- \rightarrow \gamma\mu^-\nu$, $K^- \rightarrow \pi^0\mu^-\nu$, and $K^- \rightarrow \gamma\mu^-\nu$ in the space between the PWC spectrometer magnet and the target-calorimeter, and (3) any hadronic interactions which lead to final states with only one π^- and one or more π^0's (i.e., no high energy hadrons except the π^- which decays to the triggering μ^-, and π^0's which decay to two photons which shower electromagnetically). Of these three, interacting muons are overwhelmingly dominant, except at very low muon momentum. Each will be addressed below:

(1) The first step in estimating the interacting muon rates is to isolate an almost pure sample of such events. This was accomplished by selecting events in which the incident beam particle had momentum between 260 and 270 GeV/c, well below the nominal beam momentum (these events were among the half of the interacting muon events which were rejected by the PWC cuts). From the number of these "off-momentum" events with triggering μ^+'s, it was found that only about 1% of the events could have originated from pions passing the momentum cut. These muons probably were produced by pion decays in flight between the last bend in the beamline and the PWC spectrometer, a distance of about 330 meters.

One use of this almost pure sample of interacting muons was to test the fitting procedure. As mentioned in Section 5.1.2, the sum of two gaussians (with the same mean) provided a good fit to the shower length distributions. This is illustrated in Figure A4-2. The events at long shower length were due to muon interactions which produced hadrons and will be dealt with later in this appendix.

The off-momentum events also provided a means of determining the shape of the momentum distribution of "on-momentum" interacting muons, since each event could be scaled to 278 GeV/c, holding y fixed (see Appendix 5). The only problem with this is that the y acceptance of the trigger was slightly smaller for the lower momentum muons ($.12 < y < .92$) than for the on-momentum 278 GeV muons ($.11 < y < .93$). Scaling events to 278 GeV does not replace this missing acceptance, but the difference is so small that it matters only at low y, where the cross sections vary extremely rapidly.

The normalization of this distribution can be obtained by normalizing to the real high-p data in the region of very high momentum, where interacting muons are the dominant source of events (small corrections for other sources of events are necessary however). But first another source (besides 278 GeV/c muons) of interacting muon events must be considered. Pions and

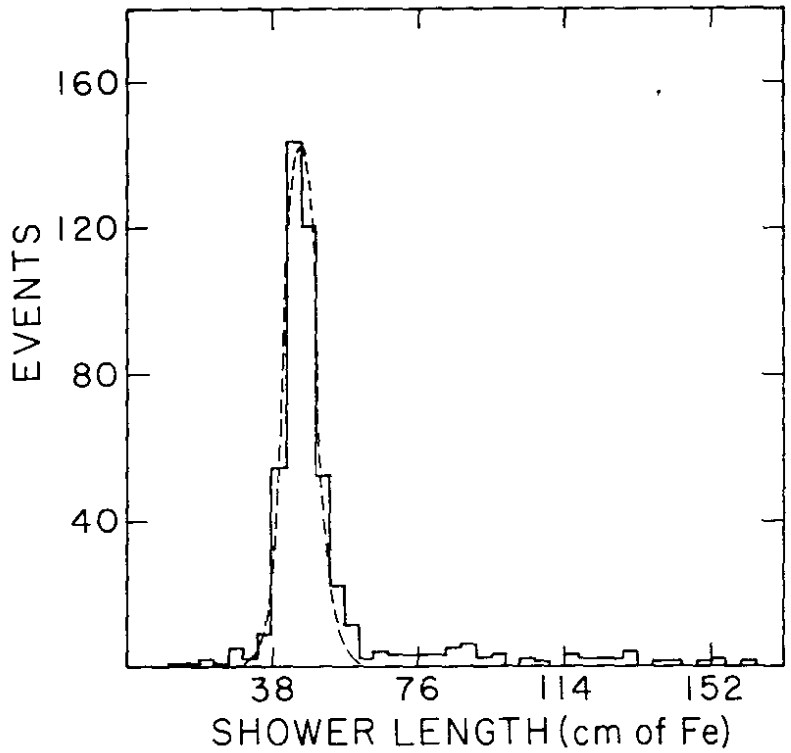

Figure A4-2: Shower length for events selected with incoming beam particle momenta between 260 and 270 GeV/c for the out-going momentum bin from 80 to 110 GeV/c. The plot includes all data from the COMPACTED, SPECIAL 1, and SPECIAL 2 configurations. The dotted line is the result of a fit to the sum of two gaussians constrained to have the same mean.

kaons whose momenta were measured in the PWC spectrometer to be within the ±2.5% momentum cut could still decay in flight in the 7.7 meters between the spectrometer magnet and the target-calorimeter (in fact, the 7.7 meters is the distance to the mean interaction point of hadrons in the target-calorimeter). Muons from such decays could interact and trigger. Here, unlike the case of on-momentum muons, the number of incident muons is known (because it only depends on the pion and kaon masses, lifetimes, muonic branching ratios, momenta and the length of the decay space). The muons from pion decays had momenta distributed uniformly between 159 and 278 GeV/c; the muons from kaon decays, constituting only (1.89 ± .95)% of the total, had momenta distributed uniformly between 13 and 278 GeV/c. The number of interactions from these muons was not large in comparison to the on-momentum muons, but because of the lower momentum of the incoming muons, the out-going muons tended to have lower momentum also, causing these events to constitute a significant fraction of the total at low momentum.

It is useful to adopt a notation for the two logically different classes of interacting muons. Interactions due to on-momentum muons will be denoted by $I\mu(1)$. Those due to muons from pion and kaon decays just upstream of the target-calorimeter will be denoted by

$I\mu(2)$.

The $I\mu(2)$ rates were determined as follows. The probability for calibration muons of five different momenta (50, 100, 175, 225, and 278 GeV/c) to satisfy the IBV requirement was measured. Short showers were required of these events, since there was some contamination due to pions in the beam. This provided the probability as a function of momentum that a muon would interact via one of the purely electromagnetic processes, although the statistics were rather poor. This interaction probability as a function of momentum was used to weight the distribution of incoming muons to determine the interaction rates. The momentum distribution of the out-going muons was determined from the empirical y-distribution obtained from the events with incoming momenta between 260 and 270 GeV/c. The errors in this calculation are due mainly to the uncertainties in the interaction probability and have been estimated to be about 30%.

The normalization of the $I\mu(1)$ distribution was chosen to cause the sum $I\mu(1) + I\mu(2)$ to equal the single μ^- rate in a bin from 190 to 230 GeV/c (after a 3% correction for pion decay). At these high momenta, other sources of single muons were negligible. Pion decay was estimated to be about 3% of the μ^- rate in this bin by extrapolation from the measured decay rates at lower

momenta using the data from Reference 65. To check that the small missing y-acceptance was not a significant effect in this bin, the normalization was also calculated for a bin from 150 to 170 GeV/c (where more, albeit small, corrections must be included, for example for charmed particle decays) and was found to be consistent. Also, in order to avoid double counting of the inelastic production of hadrons by muons, a 12% reduction was made in $I\mu(1)$ (which will be restored, as a function of momentum, later in this section). The main source of error in the normalization comes from the uncertainty in the pion decay rate in the 190 to 230 GeV/c momentum range. The extrapolation from lower momentum cannot be considered very reliable since the data used were reported only for fixed p_T, and it is possible that the p_T distributions for pion production at momenta sufficiently high to yield muons in this momentum bin are different than those at lower momentum. Therefore, a 6% systematic error has been assumed in the normalization.

(2) The decays $\pi^- \to \gamma\mu^-\nu$, $K^- \to \pi^0\mu^-\nu$, and $K^- \to \gamma\mu^-\nu$ immediately upstream of the target-calorimeter (but downstream of the PWC spectrometer magnet) could cause triggers because the photons would deposit their energy in the calorimeter and the muons could penetrate to the end of the detector. However, since the showers in these events were purely electromagnetic, they were included in

the result of the shower length fits. Therefore, it is necessary to include them in any comparisons between the fitting method and the calculated interacting muon rates. However, since these events constituted a separate background from interacting muons, they were discussed in Section 5.2.3.

(3) Any hadronic interaction in which the final state consisted of a single π^- and any number of π^0's could both trigger (if the π^- decayed) and be mistaken for an interacting muon (since the showers would be purely electromagnetic). It should be emphasized that while such events were, strictly speaking, non-prompt, no harm was done by subtracting them (if they were not subtracted, they would have been "removed" by the density extrapolation). These events need be considered here only because they impact upon a comparison of the fitting method and the calculated $I\mu(1) + I\mu(2)$ rates.

The diffractive dissociation of the incident π^- leads predominantly[66] to $\rho^0\pi^-$ and $\rho^-\pi^0$ states. In the latter case, the ρ^- will almost always decay to $\pi^-\pi^0$, leading to a $\pi^-\pi^0\pi^0$ final state. The rate expected from the <u>coherent</u> production (i.e., no nuclear break-up) of this state has been evaluated using the measurements from Reference 67 (the cross section is about 8 mb). It is not expected that the coherent production of this state alone accounts for all possible sources of events of the

required topology. For example, the reaction obviously need not be exactly coherent. It is only required that no extra hadrons have enough energy to cause the resulting shower to be longer than a typical electromagnetic shower. In fact, as will be seen below, it appears that the coherent production of $\rho^-\pi^0$'s accounts for about half the observed non-prompt rate for events with purely electromagnetic showers.

Figure A4-3 shows the four sources of events with purely electromagnetic showers versus the momentum of the out-going muon. As can be seen, on-momentum interacting muons ($I\mu(1)$) account for the bulk of the total and dominate at high momentum. Interestingly, it is the hadronic events that dominate at very low momentum (shown for the COMPACTED density in the figure). The errors in the rates are not shown, simply to avoid confusion. For the most part, it is the normalizations of the various distributions that are uncertain and not the shapes. The uncertainties in normalization are about 8% for $I\mu(1)$ (statistical plus systematic), about 30% for $I\mu(2)$, and about 50% for the rare pion and kaon decays (all the uncertainty coming from the uncertainty in the kaon fraction in the beam; see Section 5.2.3). The coherent $\rho^-\pi^0$ contribution is probably known

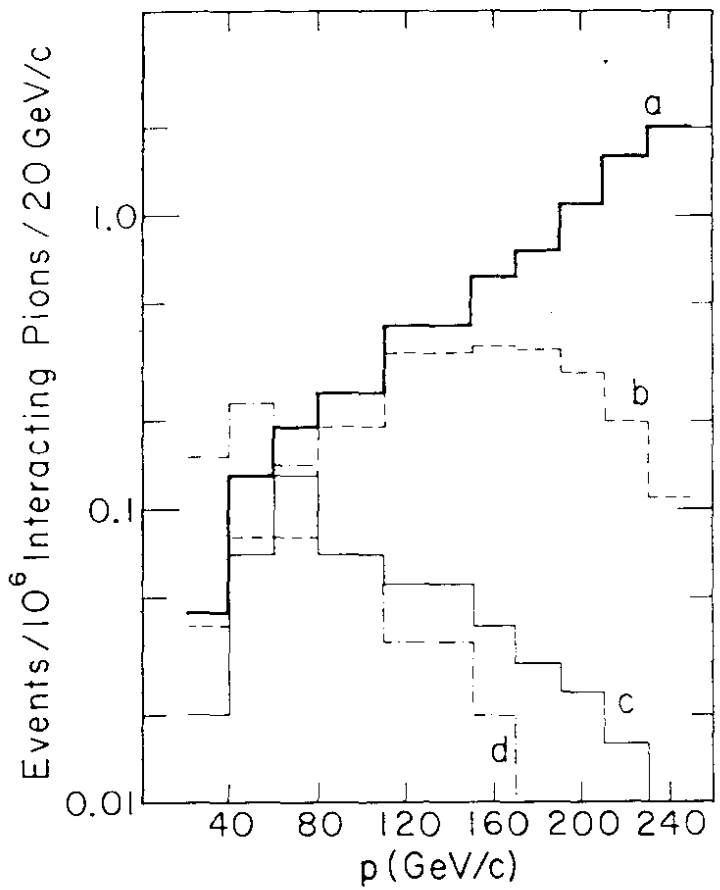

Figure A4-3: Rates versus momentum for the four types of events that produce purely electromagnetic showers: (a) Iμ(1), (b) Iμ(2), (c) pion and kaon decays upstream, and (d) coherent production of $\rho^-\pi^0$.

to about 20%, but since other processes could contribute this is therefore something of a lower limit.

Figure A4-4 shows the sum of the four distributions from the previous figure, with errors included, along with the the rates measured by the shower length fit for the COMPACTED configuration of the target-calorimeter. Figure A4-5 shows the same quantities for the EXPANDED configuration. The agreement is good, except at low momentum. It should be noted that not only does the disagreement at low momentum follow the shape of the coherent $\rho^-\pi^0$ production, but it also increases by about a factor of two between COMPACTED and EXPANDED. Therefore, the disagreement between the fitting method and the calculations can be attributed to hadronic reactions which have not been included in the calculation.

Having established that muon interactions which produced purely electromagnetic showers have been delt with properly, it is now necessary to consider muon interactions which produced hadrons, and therefore were not removed by the shower length subtraction. Figure A4-6 shows the expected ratio of inelastic production of hadrons to the sum of bremsstrahlung, direct pair production, knock-on electron production versus y. (See Figure A4-1 and Appendix 5.) This ratio can be measured

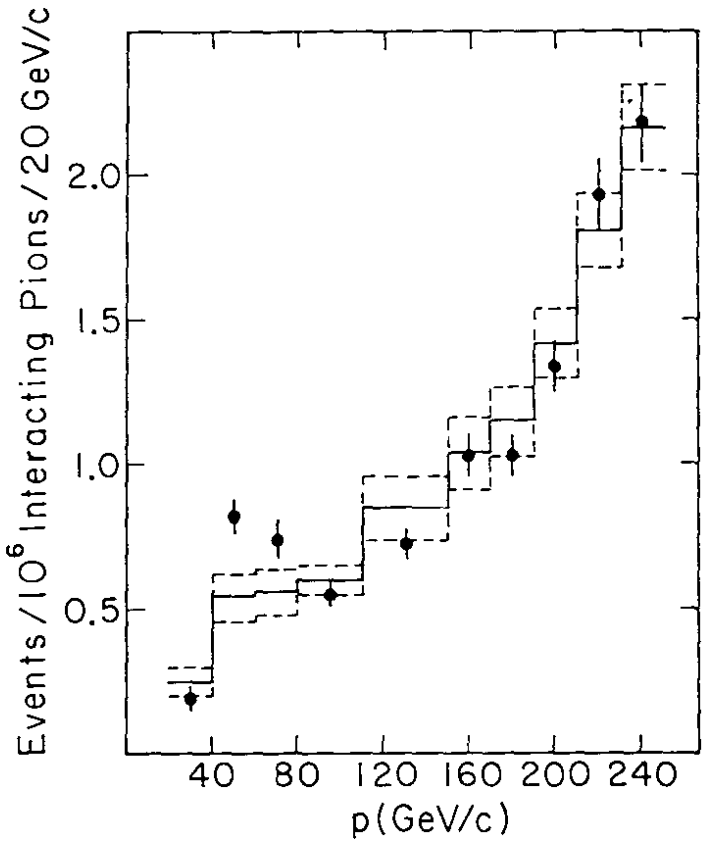

Figure A4-4: Calculated and measured interacting muon rates for the COMPACTED configuration. The measurements are from the shower length fit. The calculations include the four sources of purely electromagnetic showers discussed in the text. The dotted lines indicate the uncertainty in the calculation.

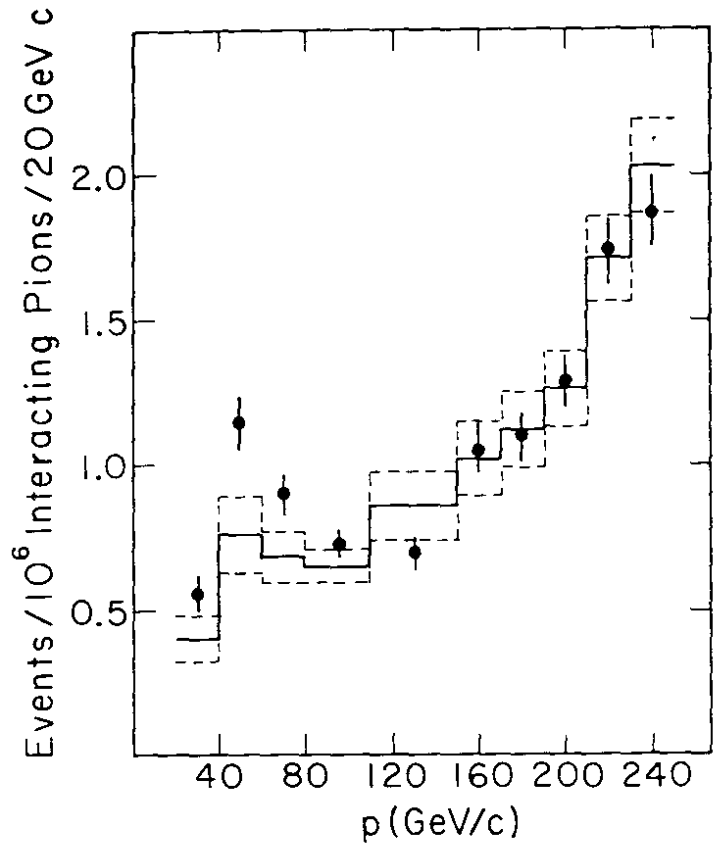

Figure A4-5: Calculated and measured interacting muon rates for the EXPANDED configuration. The measurements are from the shower length fit. The calculations include the four sources of purely electromagnetic showers discussed in the text. The dotted lines indicate the uncertainty in the calculation.

from the off-momentum (260 to 270 GeV/c incident) interacting muon events by taking the ratio of the number of events with "long" showers to the number of events in the electromagnetic peak. Events whose shower length was greater than 64.8 cm were classified as hadronic (see Figure A4-2, for example). These measurements, versus y, are also shown in Figure A4-6. Two comments regarding these measurements are necessary: First, the ratio for low y is not shown in the figure because only events with more than 75 GeV in the calorimeter have been used. (This is in order to be far enough above the ESUM threshold that any difference between the calibration for hadronic and electromagnetic showers would not matter.) Second, the errors in the ratio become large at high y because a subtraction had to be made for events due to pion interactions.

The good agreement between the calculated and observed ratios implies that the calculation can be trusted. Therefore, the curve shown in Figure A4-6 has been used to calculate the rates for hadronic production by muons from the previously calculated $I\mu(1)$ and $I\mu(2)$ distributions. The effect of the small density dependence in $I\mu(1)$, which is probably due to different beam conditions, has been taken into account. The total subtraction was found to be .29 ± .04 per 10^6 IBV's for events with $p < 150$ GeV/c. This amounts to about 2% of

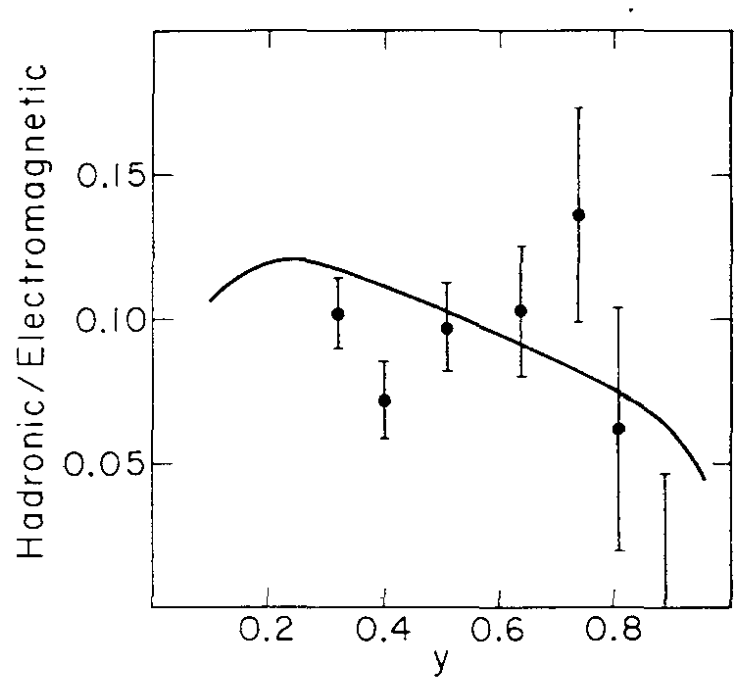

Figure A4-6: Measured and calculated ratio of inelastic hadron production by 278 GeV/c muons on iron to production of purely electromagnetic final states versus y.

the prompt single μ^- rate (after the subtraction for highly asymmetric dimuons).

Recall that interacting muons with purely electromagnetic showers were subtracted versus p_T using the fitting method, as described in Section 5.1.2. It was checked that the shape versus p_T of these rates was the same as that of the events in the momentum range between 260 and 270 GeV/c. The p_T distribution of interacting muons that produced hadrons was taken to have the same shape and was normalized to .29 ± .04 events per 10^6 interacting pions.

APPENDIX 5

MUON INTERACTION CROSS SECTIONS

In this appendix, the equations which were used to calculate the curves in Figures A4-1 and A4-6 are given. All cross sections are given <u>per nucleus</u>.

The cross sections versus y ($y = E_{lost}/E_{initial}$) for bremsstrahlung, knock-on electrons and direct pair production were taken from Rossi[68]. The equations (not in the notation of Rossi) are:

$$\frac{d\sigma_{brem}}{dy} = \alpha Z^2 r_e^2 \left(\frac{m_e}{m_\mu}\right)^2 \frac{4}{yE}\left[\frac{4}{3} - \frac{4}{3}y + y^2\right] \times \left\{ \ln\left[\frac{2E}{m_\mu}\frac{\hbar c}{m_\mu r_n}\frac{1-y}{y}\right] - \frac{1}{2}\right\},$$

$$\frac{d\sigma_{knock\text{-}on}}{dy} = Z\left(\frac{2\pi\alpha^2}{E m_e}\right)\left[\frac{1}{y^2} - \frac{1}{y} + \frac{1}{2}\right],$$

and $$\frac{d\sigma_{pair}}{dy} = \frac{8}{\pi}\alpha^2 Z^2 r_e^2 \left(\frac{m_e}{m_\mu}\right)^2 \frac{1}{y^3}$$

$$\times \begin{cases} \ln\left(\frac{1}{\alpha Z^{1/3}} \frac{m_\mu}{m_e} y\right) ; & y < y_t \\ \ln\left(\frac{2E}{m_\mu}\right) ; & y > y_t \end{cases}$$

where $$y_t = \frac{2m_e}{m_\mu}\alpha Z^{1/3} ,$$

α is the fine structure constant, Z is the number of protons in a target nucleus (Z = 26 for iron), r_e is the classical radius of the electron, m_e is the electron mass, m_μ is the muon mass, E is the initial muon energy, and $r_n = 1.38 \times 10^{-13}$ cm $A^{1/3}$ (r_n = 5.28 fm for iron).

The cross section equation for the production of hadrons by muons has been derived by Bodek and modified for the effects of nuclear shadowing at low Q^2 (see, for example, Reference 69). The structure function F_2 has been taken from fits to SLAC data from Reference 70. The cross section is given by

$$\frac{d\sigma}{dy} = A\left(116 \times 10^{-30}\,\mathrm{cm}^2\right)\frac{\alpha}{\pi}$$

$$\times \int_{t_{min}}^{t_{max}} F_{SHAD}(t)\left[\left(1 - y + \tfrac{1}{2}y^2\right)\frac{F_2(\omega_w)}{t^2}\left(\frac{\omega_w}{\omega}\right) - \frac{m_\mu^2 y^2}{t^2} F_2(\omega_w)\left(\frac{\omega_w}{\omega}\right)\right] dt ,$$

where $t = Q^2$, $\omega = \frac{2M\nu}{t}$, $\nu = yE$,

$$\omega_w = \frac{2M\nu + a^2}{t + b^2} , \quad t_{min} = \frac{m_\mu^2 y^2}{(1-y)^2} ,$$

$$t_{max} = 2M\nu + a^2 - b^2$$

$$F_{SHAD}(t) = \begin{cases} .7 + \frac{.3}{.2}t ; & t < .2 \\ 1.0 ; & t > .2 \end{cases} ,$$

$$F_2(\omega_w) = \frac{1}{2}\sum_{n=3}^{7} c_n (1 - X_w)^n ,$$

$$X_w = \frac{1}{\omega_w} ,$$

and M is the proton mass. The parameters used were: a^2 = 1.512, b^2 = 0.351, c_3 = 0.477, c_4 = 2.160, c_5 = 3.627, c_6 = -10.470, and c_7 = 4.927.